

Proceedings of  
National Conference on

---

Emerging  
Areas of  
Photonics  
and  
Electronics

---

*September 15 – 16, 2011  
Kolkata, India*

*Jointly Organized by  
SPIE Student Chapter,  
B P Poddar Institute of Management & Technology  
&  
Department of Electronics & Communication Engineering,  
B P Poddar Institute of Management & Technology*

**E d i t o r s**

Arijit Saha  
Ivy Majumdar  
Surajit Mandal  
Shila Ghosh

Department of Electronics & Communication Engineering  
B P Poddar Institute of Management & Technology, Kolkata, India

***Author Disclaimer***

While the author and the publisher believe that the information and the guidance given in this work are correct, all parties must rely upon their own skill and judgement when making use of it. Neither the author nor the publisher assume any liability to anyone for any loss or damage caused by any error or omission in the work, whether such error or omission is the result of negligence or any other cause. Any and all such liability is disclaimed.

***Published by***

Department of Electronics & Communication Engineering,  
B P Poddar Institute of Management & Technology,  
137, VIP Road,  
Kolkata 700052, India.

**EMERGING AREAS OF PHOTONICS AND ELECTRONICS  
Proceedings of National Conference on  
Emerging Areas of Photonics and Electronics (EAPE 2011)**

*All rights reserved. This book, or parts thereof, may not be reproduced in any form or by any means, electronic or mechanical, including photocopying, recording or any information storage and retrieval system now known or to be invented, without written permission from the publisher.*

This proceeding is prepared using Microsoft Word from electronic manuscripts submitted by the authors.

Cover design: Arijit Saha

## PREFACE

With the rapid growth and sophistication of digital technology and computers communication have become more versatile and powerful. Rapid development of optical communication during last three decades enhanced the advancement of communication system. Optical fiber technology and waveguides not only provide the necessary frequency bandwidth to accommodate a potentially large number of channels (and hence a huge capacity), but also offer an immunity from the electromagnetic interference from which the traditional transmission medium often suffers. In addition to optical waveguides, another key area of technological development which plays a crucial role in the success of optical communication systems is optical devices. The rapid growth of semiconductor laser diodes has allowed optical transmitters to be miniaturized and become more powerful and efficient. The technological forces which gave us optical waveguides and semiconductor laser diodes have recently explored theoretical research and manufacturing technology to develop further innovative devices that are crucial in optical communications, for example, optical amplifiers, optical switches and optical modulators. But the *optical/electronic* conversion limits the bandwidth of the system. The advent of photonic integrated circuits (PIC), which are ICs built entirely with optical components, such as laser diodes, waveguides and modulators, will further enhance the power and future prospects of optical communication networks. Not only communication but there are a range of applications in different directions of said devices such as medical imaging, adaptive optical, nanophotonics, Biosensors, image processing, signal processing etc. Wireless communication is also a subject of recent interest and a lot of research works is being done in the field.

The interdisciplinary nature of the subject needs cross connection between the diverse braches and sub branches to develop awareness of the trends. In view of this we organized this conference providing a common forum for formal and informal interaction and exchange of ideas on the emerging areas of electronics and photonics. We believe that students, teachers, researchers and practicing engineers will be enriched and enlightened from this conference.

The areas covered are:

- Free-Space & Guided Optical Communication
- Photonic Devices & Optoelectronic Integrated Circuits
- Adaptive Optics and Astronomical Instruments
- Lasers and Laser Systems
- Biomedical Optics and Electronics
- Electronic & Optical Materials
- Optical & Electronic System Design
- Wireless & Optical Networks

- Microwave & Mobile Communication
- Nano-Technology
- Signal Processing
- Hybrid Image Processing
- VLSI and Embedded Systems

We are indebted to the members of the advisory committee who took serious interest in the Conference and have contributed significantly to this publication. The tremendous efforts of the reviewers are also gratefully acknowledged. We are also thankful to the management of B P Poddar Institute of Management and Technology for providing their support to make the conference a grand success.

Editors

## **EAPE 2011**

### **Patrons**

Arun Poddar, Chairman, BPPIMT  
Ayush Poddar, Vice Chairman, BPPIMT  
Subir Choudhury, Director, BPPIMT

### **General Chair**

Arun Majumdar, Sr. Scientist, Ridgecrest, California, USA

### **Advisory Committee**

Otakar Wilfert, Professor, Brno University of Technology, Czech Republic  
V.P.N Nampoori, Professor, Cochin University of Science and Technology, India  
Mritunjay Bhattacharya, Ex-Vice Chancellor, WBUT, India  
B.N.Chatterjee, Ex-Professor, Dept.IIT Kharagpur, Dean of BPPIMT, India  
A.K. Chakrabarty, Ex-Professor, University of Calcutta, India  
Alok Kumar Das, Ex-Professor, Jadavpur University, India  
S. L. Jain, Emeritus Scientist, National Physical Laboratory, India  
R. Vijaya, Professor, IIT Bombay, India  
K. Bhattacharya, Professor, University of Calcutta, India  
P. P. Sahu, Professor, Tezpur University, India  
Avijit Kar, Professor, Jadavpur University, India  
Sutapa Mukherjee, Principal, BPPIMT, India  
S. C. Chakravartty, Ex-Principal, BPPIMT, India

### **Convener**

Shila Ghosh, BPPIMT, Kolkata

### **Technical Committee**

Bhaskar Som, BPPIMT, Kolkata  
Ivy Majumdar, BPPIMT, Kolkata  
Arijit Saha, BPPIMT, Kolkata  
Surajit Mandal, BPPIMT, Kolkata

**Organizing Chair**

B N Chatterji, Dean, BPPIMT

**Organizing Committee**

Sandip Ghosh, BPPIMT, Kolkata  
Somali Sikder, BPPIMT, Kolkata  
Kabita Paul, BPPIMT, Kolkata  
Kunal Mandal, BPPIMT, Kolkata  
Mohammad Wasim Sayed, BPPIMT, Kolkata  
Nasibullah, BPPIMT, Kolkata  
Nazimul Gazi, BPPIMT, Kolkata  
Dipanwita Roy, BPPIMT, Kolkata  
Niket Kumar Mishra, BPPIMT, Kolkata

**Finance Committee**

Panthadeb Saha, BPPIMT, Kolkata  
Dipsikha Ganguly, BPPIMT, Kolkata  
Arghya Pratim Ganguly, BPPIMT, Kolkata  
Camelia Sarkar, BPPIMT, Kolkata

**Financial Co-Sponsors**

SPIE Student Chapter, BPPIMT

B P Poddar Institute of Management & Technology, Kolkata

Allmineral Asia, India

## Table of Contents

Neither the publisher nor the editors are responsible for the opinions expressed by individual authors and the speakers.

<i>Preface</i>	iii
<i>Advisory Committee</i>	v
<i>Organizing Committee</i>	vi
<i>Sponsors</i>	vii
Free-Space Laser Communications: Fundamentals, System Design, Analysis and Applications <i>Arun K. Majumdar</i>	1
Recent research and development in Free-Space Laser Communications emphasis on UV Communications <i>Arun K. Majumdar</i>	2
Some challenging areas in Free-Space Laser Communications <i>Arun K. Majumdar</i>	3
Biophotonics and Nanobiotechnology <i>V P N Nampoore</i>	4
<i>Optical Communication Network and Devices</i> Alok Kumar Das	6
Opical Networking <i>S Maity</i>	9
Influence of Diffraction Effect on FSOL function <i>Otakar Wilfert and Juraj Poliak</i>	10
Network Configuration and Energy-Efficient Compression to Maximize Lifetime in Wireless Image Sensor Network <i>Ashraf Hossain</i>	16
Automated Laser Reflectometer Imaging System <i>Samrat and J. Indumathi</i>	29

Evaluation of Power Consumption in adiabatic universal gates <i>Samik Samanta</i>	35
Dual Band Notched Fractal Ultra-Wideband Antenna <i>Anirban Karmakar and Shabana Huda</i>	39
Fiber Optic Sensor Mechanisms for Biochemical Detection <i>Ricky Anthony and Sambhunath Biswas</i>	46
Design and realization of solar internal lighting system for homes and office spaces <i>Kavitha K.G., Upkar Kumar, Rethesh R., A.Mujeeb, P.Radhakrishnan, V.P.N.Nampoori</i>	60
Low Temperature DC conductivity of Graphite Kaolinite composite <i>R.Goswami, S.C.Chakravarty, E.Bose, U.Mukherjee, P.Saha, P.Mondal</i>	65
A Zero-Order Achromatic Quarter-Wave Retarder <i>Arijit Saha, Kallol Bhattacharya, Ajoy Kumar Chakraborty</i>	70
Texture Matching of Gray Level Images Using Legendre Moment Technique <i>Ivy Majumdar, Suvankar Das, Avirup, Avijit Kar, B.N.Chatterji</i>	77
Imaging Characteristics of a Birefringent Lens in the Infrared Region <i>Surajit Mandal, Ajay Ghosh</i>	84
A New Modulation and Coding Scheme for Free Space Optical Communication Using Turbo Coded BICM – ID with 16 QAM <i>A. Sarkar, P. Saha</i>	95
Implementation of an audio equalizer with user specified cutoff frequencies in MATLAB GUIDE using a peak filter <i>Saatwik Katiha</i>	99
Lasing Without Population Inversion <i>Lipika Adhya</i>	109
A three-element variable retarder for infrared monochromatic light using crystalline quartz <i>Arijit Saha</i>	116

X

A Novel Technique for Computing the Polychromatic Optical Transfer Function of Optical Imaging Systems 123

*Surajit Mandal, Ajay Ghosh*

Development of Colorimeter using Low Cost Optical Bridge 130

*Kushan Chakrabarty, Isha Das and Shila Ghosh*

Secured Data Communication Using PCM and Pseudo-Noise Generation 135

*Mohammad Wasim Sayed and Nasibullah*

*INVITED TALK*  
**Free-Space Laser Communications: Fundamentals, System  
Design, Analysis and Applications**

Arun K. Majumdar

Senior Scientist, Ridgecrest, California USA  
Email: a.majumdar@IEEE.org

**Abstract.**

This lecture introduces the fundamental concepts involved in understanding free-space laser communication system design and performance. Concepts for system design and subsystem design using commercially available laser, opto-electronic components, and fast detectors will be developed. Starting from a basic treatment of the effects of atmospheric turbulence and scattering media on high-data-rate laser signals, we discuss how to analyze overall link budget performance including the effects of the atmospheric channel.

*INVITED TALK***Recent research and development in Free-Space Laser Communications: emphasis on UV Communications**

Arun K. Majumdar

Senior Scientist, Ridgecrest, California USA  
Email: a.majumdar@IEEE.org**Abstract**

This lecture will cover recent exciting areas in Free-Space Optical (FSO) communication which is a mature field, but facing many exciting fundamental and technological challenges in order to improve its performance in arrange of scenarios. Research challenges exist in areas like short range FSO systems, long range terrestrial communication links through atmospheric turbulence, improvement of the FSO performance with clever transceiver implementations, new beam profiles, adaptive optics, and the right modulation schemes. Specific example in this lecture will cover non-line-of-sight links using solar blind UV radiations scattered from transmitter to receiver which opens interesting communication scenarios.

*INVITED TALK*  
**Some challenging areas in Free-Space Laser Communications**

Arun K. Majumdar

Senior Scientist, Ridgecrest, California USA  
Email: a.majumdar@IEEE.org

**Abstract.**

This lecture will cover and discuss some of the fundamental and technological challenging areas where more research efforts need attention. Some of these emerging areas include, but not limited to: underwater laser links, Free-space optics (FSO) communications in indoor spaces, non-line-of-sight FSO communications, chaos based secure communication links, adaptive optics and other mitigation based high data rate communications in presence of turbulence.

***INVITED TALK***  
**Biophotonics and Nanobiotechnology**

V P N Nampoory

International School of Photonics,  
Cochin University of Science and Technology, Cochin 682022  
nampoory@gmail.com

**Abstract.**

**Biophotonics** is a new field of research referring to the intersection of light with biology and medicine. Biophotonics can also be defined as a field emerged out of the marriage between photonics, the technology of light, and biotechnology, the technology of life sciences. Latest related field is the recently emerged nanobiotechnology which is the fusion of nanotechnology and biotechnology. Biophotonics and nanobiotechnology provide appropriate materials and technology which help light in serving the well being of the biosphere in general and human life in particular.

The present talk is an over view of biophotonics and nanobiotechnology. The talk consists of 1) introduction to photonics, biophotonics, nanobiotechnology 2) materials for biophotonics and nanobiotechnology 3) Introduction to bio imaging techniques- confocal microscopy 3) Biomaterials for photonic applications 4) photonic and nanomaterials for biological and medical applications 5) Interaction of low frequency electromagnetic radiation on biomolecules like DNA 6) conclusion

The first section of the talk will describe basic ideas and concepts involved in photonics, photonic bandgap materials, nanotechnology and nanobiotechnology. The second section will deal with various materials which are important in biophotonics and nanobiotechnology. Various methods of materials synthesis based on biological molecules also will be discussed. Confocal microscopy and related techniques in

bioimaging will be described at length. Devices and materials based on biopolymers like DNA and proteins will be reviewed towards the end of the talk.

The effect of low frequency electromagnetic radiation on biomolecules is a topic of current importance due to the overdose of electromagnetic radiation in the biosphere originating from mobile phone and mobile phone towers. The talk will touch up on the photonic techniques to monitor the impact of such radiations in biomolecules like DNA.

The talk will conclude with some future prospects.

*INVITED TALK*  
**Optical Communication Network and Devices**

Alok Kumar Das

Ex-Professor, Department of Electronics & Communication Engineering  
Jadavpur University  
Email: alok\_kumar\_das@yahoo.com

**Abstract**

To accommodate the skyrocketing amount of traffic, optical network with wavelength division multiplexing (WDM) having several wavelengths per fiber as channels, is the most feasible solution. Transmission rate of a channel with 2.4, 10 or 40 Gbps is indeed achievable only in the electrical domain. With the advent of optical amplifiers in the mid 1990s and later on the feasibility of various types of optical switches, have enabled to consider the development of a new generation of optical networks in which optical signal with a given light path is routed without O-E-O (optical to electrical and electrical to optical) conversion and thus reduces the deployment time and produces additional network robustness. It has the advantage of eliminating the intermediate layer such as such as ATM and SONET/SDH. In a larger networks having more number of nodes, more wavelengths are needed and to avoid the large number of wavelengths the wavelength-routed networks overcome these limitations through wavelength reuse, wavelength conversion, and optical switching. The OXC (Optical Cross Connect), optical circuit switches (OCS), optical packet switches (OPS), and optical burst switches (OBS) techniques are considered where OXC produces the switching fabric for long term traffic demands. The OCS, OPS and OBS techniques require a light path to reconfigure automatically the switching fabric. Optical level switching (OLS) offers interoperability between OPS, OBS, and OCS and demonstrates successfully in Global optical network for multi-service applications. IP (Internet Protocol) backbone carriers are now connecting

core routers directly over point-to-point WDM links (IP over WDM). This layer structure with a help of GMPLS (Generalized Multi Protocol Level Switching) and OXC (Optical Cross Connect) with IP packets are directly mapped into wavelength channels. The technologies for core networks (intercity), metro networks for MANs (intra-city), and local access networks for the services to the home or business, need rapid provisioning of connections within each subnet. The numerous investigations have been carried out to solve routing and wavelength -assignments (RWA) problem in this DWDM networks considering the static light path system applying OXC-based networks and the dynamic light path system applied to OCS, OPS and OBS-based networks.

The objective of the tutorial is to provide firstly the various investigations of optical transparency, mainly on optimization techniques related to RWA problem. The variation of quality of transmission (QoT) depending on RWA problem and hence for better network planning or better traffic engineering, will also be discussed. We consider the design of a network under long term traffic demands as OXC-based networks where as the dynamic traffic demands in OCS, OPS or OBS-based networks. Traffic statistic and optical burst overlap reduction in core routers of OBS networks will be discussed. In a second step, we describe the various devices for different components (Transponders, WDM multiplexers/de-multiplexers, amplifiers, optical fibers) to be required in a typical optical transmission system. Now-a-day there is a need to develop efficient optical components and devices relevant to the different optical networks with better (QoT). We shall discuss the router and routing techniques and different switches and their implementations. The different implementation methods of the switches are mechanical, MEMS, liquid crystals, bubble, waveguide type TO (Thermo-optic) and EO (Electro-optic) switches, wavelength routing switch (AWG and tunable ?), etc. These optical switches are very efficient and depending on size, capacity, speed, scalability, and cost one technology may prove superior to another, at least for specific needs. The advantages and disadvantages of electrical, Opto-electronics and optical switches and in-depth understanding for their requirements considering the limitation of the bandwidth between the links in different network systems will be discussed. The other waveguide type

devices like modulators, attenuators, add/drop filters, couplers, power dividers and combiners, TE and TM mode splitters etc., required for optical networks, will be discussed considering their low losses and compact sizes. Now-a-day polymeric optical waveguide devices have attracted great interest in the field of integrated optics as it offers many advantages compared with other available waveguide materials because of their potential for easy, low-temperature and low-cost processing, highly tunable material index with large Thermo-optic coefficient. It also offers EO property with large Electro-optic coefficient. It possesses high nonlinear optical property for high speed and wide-band signal processing. The demand for low priced polymeric optical fibers (POF) is increasing due to their many short distance applications (10Gbps transmission over 100 meters) including fibers in home. Lastly, we shall discuss the networking of 21st century.

*INVITED TALK*  
**Optical Networking**

S Maity

General Manager,  
Eastern Telecom Project, BSNL

**Abstract.**

Telecommunication network comprising of network elements such as voice and data switches, routers, database servers, multiplexers and so on are all connected by long distance and short distance transmission links. With the progress of time, bandwidth requirement of links is on the rise. Among all the technologies available today for transmission links, Optical Fibre Cable (OFC) is the only technology which meets the requirement of bandwidth exclusively for the core network. However, in the access network both OFC and different wireless technologies are used. But with more and more data centric applications, OFC has even reached the home. Fibre To The Home (FTTH) is now a reality and specially in urban environment where multistoried complex are being constructed, FTTH is the proper technology to support all services such as voice, high speed Internet access with download speed of upto 100 Mbps, Video on Demand, IPTV etc.

***INVITED***  
**Influence of Diffraction Effect on FSOL function**

Otakar Wilfert, Juraj Poliak

Dept. of Radio electronics, Brno University of Technology,  
Purkynova 118, Brno, 612 00, Czech Republic

wilfert@feec.vutbr.cz; phone +420-541149130

**Abstract:** The paper deals with an important influence of diffraction effect on Free-Space Optical Link function. The main advantages and disadvantages of the Free-Space Optical Link are mentioned in the contribution. Scalar theory of diffraction is presented and important solution of wave equation – Gaussian beam is introduced. In practical part, approach based on Fast Fourier Transform algorithm is discussed. Simple program for user-friendly simulation of this approach in MATLAB was created and the results of it will be demonstrated. Modeling of the influence of diffraction effect on laser beam shape makes improvement of FSOL design possible.

**Keywords:** Diffraction, Gaussian beam, Fourier transform, GUI

## 1. INTRODUCTION

Today wireless communication technologies are characterized by lack of free frequencies, in particular in urban areas. Together with the demands on high data rates it leads to the utilization of higher and higher frequency bands, typically from 50 to 100GHz. The properties of radio systems using very high carrier frequencies are becoming similar to the properties of systems using a narrow optical beam (line-of-sight requirement, dependence on atmospheric phenomena). The utilization of such frequencies brings substantial technological problems. A natural solution to the problem would be using an optical carrier [1-2].

Free-Space Optical Link (FSOL) is an optical line-of-sight broadband communication that transmits optical signals in free space by narrow optical beams. Usually, a non-coherent laser intensity modulation is used and the link represents a clear (protocol-independent) transmission channel, see figure 1. It is primarily intended for connecting two points, where laying a fiber is difficult or absolutely impossible. The first generation FSO can easily attain speeds of hundreds of Mb/s, allowing direct application to Ethernet or STM-1 and STM-4 networks.

With regard to the atmospheric conditions of transmission, availability of fiber optics elements, and eye-safety, wavelengths of 850nm (short) and 1550nm (long) are used for FSOL. The link installation and operation do not bring any legal obstacles because the wavelengths fall within the infrared spectral band. Currently, no license or certificate is required. But wireless optical technology must conform to international standards of work safety for lasers.

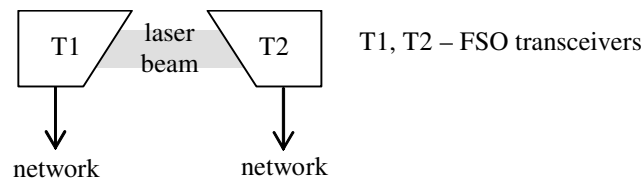


**Fig. 1** Typical FSOL configuration

The FSOL technology is interesting for a number of reasons [3]:

- FSOL is not a subject of license procedures.
- FSOL uses optical carriers ranging from 850nm to 1500nm, which does not pollute the environment with electromagnetic energy radiation on radio frequencies.
- FSOL transmitting optical power conforms to the respective international standards. The systems are designed to be eye-safe even at the transmitting aperture.
- Thanks to a very narrow beam of several milliradians it is very hard to jam or tap the FSOL. Its transmitters do not exhibit any side lobes. A potential intruder must virtually enter the beam, which can be detected.
- The FSOL bandwidth potential corresponds to that of fiber optics. The FSOL technology is then a natural complement of modern broadband fiber networks.

From atmospheric impact on the optical beam result some disadvantages of the FSOL:

- Availability of the terrestrial FSOL depends on the weather.
- FSOL requires a line of sight between transceivers.
- Birds and scintillation cause beam interruptions.
- High coherence of the laser beam causes the diffraction effect on transmitting lens.

For FSOL reliability improvement number of new methods is applied: multi beam transmission, utilization of auto tracking system system, adaptive optics, polygonal topology, etc. When the laser beam is being shaped, wave behavior of the transmitted beam is critical. By these effects stands diffraction as the most critical. Therefore diffraction will be described theoretically and its influence on transmitted beam will be simulated. A program in MATLAB environment will be created to allow user to change input parameters of the simulation.

## 2. THEORY OF DIFFRACTION

Diffraction occurs when electromagnetic radiation is bended in a way other than refraction or reflection [4]. This phenomenon is described in wave theory of electromagnetism. Its consequences are derived from Huygens-Fresnel principle [5]. For the description of the diffraction phenomenon and its effects, double integral is used. That means, double integral is needed to be calculated through the whole diffraction object and for every point in the observation plane. That would be too excessive and computationally intensive. Therefore, analytical approximations are often used to simplify and speed up the calculation for the price of accuracy [5-6]. In standard situations and technical use this accuracy is more than sufficient.

Fresnel approximation leads to a simplified integral

$$\psi(x, y, z) = C \iint_{S_0} \psi_0(x_M, y_M) \cdot e^{\frac{jk}{2z}(x_M^2 + y_M^2)} e^{-\frac{jk}{z}(x \cdot x_M + y \cdot y_M)} dx_M dy_M \quad (1)$$

Wave function describing Fresnel diffraction in the point  $(x, y, z)$  is calculated as Fourier transform of the product of the wave function  $\psi_0(x_M, y_M)$  in the plane of the diffraction aperture [7] and a phasor  $e^{\frac{jk}{2z}(x_M^2 + y_M^2)}$ . For the need of the technical practice, there is more convenient to introduce model describing distribution of the intensity  $I(x, y, z)$  in the plane of observation rather than a wave function. These relates as follows

$$I(x, y, z) = |\psi(x, y, z)|^2. \quad (2)$$

Final expression describing the distribution of the diffraction of the planar wave  $\psi_0$  on a circular aperture in the distance  $z$  is as follows

$$I(x, y, z) \propto \left| FT \left\{ \psi_0(x_M, y_M) e^{\frac{jk}{2z}(x_M^2 + y_M^2)} \right\} \right|^2 \quad (3)$$

From this equation is obvious, how the nature itself can perform Fourier transform of a signal.

## 3. SIMULATION

Simulation of diffraction uses a model described with expression (3) and was built in MATLAB program. It provides flexibility during the development of the simulation as

well as built-in functions for 2D signals processing. To ensure that even less skilled MATLAB users may use the program for the simulation, it was built in the form of GUI (graphical user interface).

Script simulates diffraction of planar Gaussian wave with beam width  $w$  and wavelength  $\lambda$  on a circular plane with radius  $r$  in the distance  $z$ . Simulation consists of several parts. In the first part, input parameters are defined:

- - Wavelength  $\lambda$
- - Distance of observation plane from the diffraction aperture  $z$
- - Radius of diffraction aperture  $r$
- - Beam width of Gaussian beam  $w$
- - Number of points of discretization  $N$

These parameters are read and used for the calculation. In the final part of the simulation, results are displayed. Input parameters can be changed in the right side of the main window of GUI (Figure 2). To run the calculation, the “Evaluate” button has to be pressed. Results are shown in the form of 4 images. Image 1 to 4 show the Gaussian profile of laser beam in the plane of diffraction aperture, circular aperture, diffraction pattern in the distance  $z$  and cut through the centre of the diffraction pattern respectively.

Simulation assumes that diffracting beam is planar, i.e. distribution of the phase in the cut upright to the direction of the propagation is constant. This assumption is never fulfilled as the beams are always slightly divergent. However, its consequences are never visible on the shape of the diffraction pattern, only on its radial size.

When diffraction for given number of Fresnel zones is needed to be simulated, orange button named “FZ => z” may be used. After entering desired number of Fresnel zones, pressing the button will calculate the distance when exactly this number of Fresnel zones is observed. Then this number as input parameter of calculation must be filled.

Besides educational purposes, this program may also be used for analysis of what minimum radius of the output lens is needed. This is always a compromise between level of diffraction effect and perfection of the shape of bigger lens. As it can be seen from the fourth image on Figure 1, in the desired centre of receiver may be lower intensity, so the receiver will “lock” to the next peak. This will cause a problem as this peak is too narrow and in turbulent atmosphere will cause higher BER. Additionally, in mobile links this effect is even more critical as these peaks are changing with the distance.

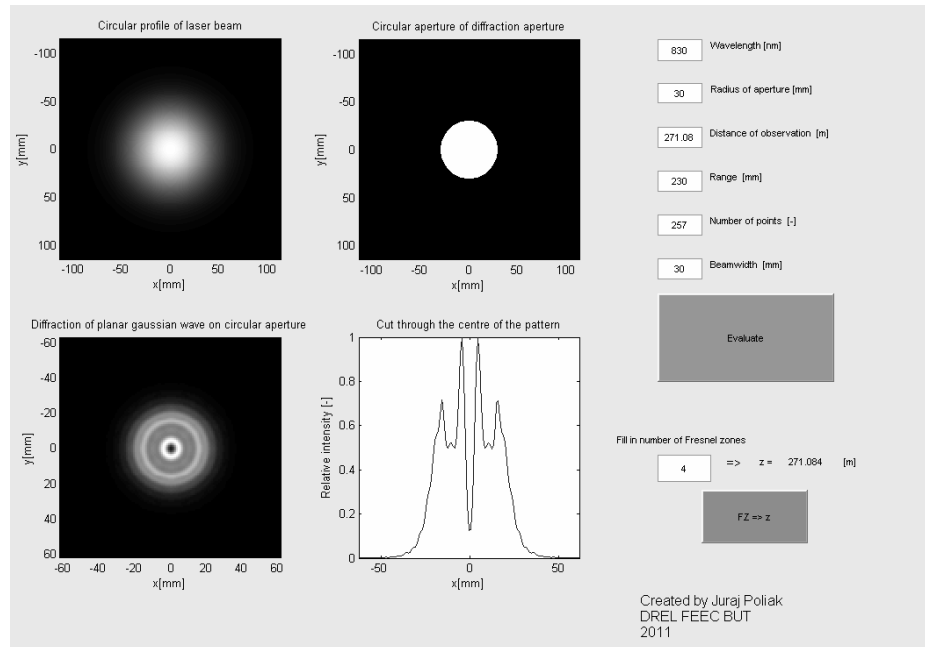


**Fig.2** Simulation of diffraction of circularly symmetrical laser beam with wavelength  $\lambda = 830$  nm and beamwidth  $w = 30$  mm on a circular aperture with radius  $r = 30$  mm in the distance  $z = 271.08$  m (exactly 4 Fresnel zones are observable).

#### 4. CONCLUSION

In the article both the main advantages and disadvantages were presented. The useful tool for simulation of diffraction was introduced. The simulation is limited with approximations, e.g. circular Gaussian beam, planar distribution of laser beam, but also need of MATLAB to be installed on the PC. Authors are currently working on extending the program to include also elliptical Gaussian beam and divergent laser beam. Simulation was consulted with prof. Jiří Komrská as well as confronted with real experiment. The influence of diffraction effect on the laser beam modeling makes improvement of FSOL design possible.

## 5. ACKNOWLEDGEMENT

The research described in the paper was supported by the Czech Grant Agency under grants No. 102/09/0550, No. P102/11/1376, No 102/08/H027 and by the research program MSM0021630513. The research has been also supported by the projects CZ.1.07/2.3.00/09.0092 and CZ.1.07/2.3.00/20.0007 WICOMT in frame of the operational program Education for competitiveness and by the Czech Ministry of Industry and Trade under grant agreement No. FR-TI2/705.

## 6. REFERENCES

1. Santamária, A., López-Hernández, F. J.: *Wireless LAN Systems*, Artech House, London, 1994.
2. Schuster, J., Willebrand, H., Bloom, S. and Korevaar, E. *Understanding the performance of Free Space Optics*, Journal of Optical Networking, Vol. 2, No. 6, pp. 178-200, 2003.
3. Majumdar, A. K., Ricklin, J. C.: *Free-Space Laser Communications*, Springer, New York, 2008.
4. Saleh, B. E. A., Teich, M. C.: *Fundamentals of Photonics*, John Wiley, New York, 1991.
5. Born, M., Wolf, E.: *Principles of Optics*, Cambridge University Press, London, 2003.
6. Osche, G.R.: *Optical Detection Theory for Laser Applications*, John Wiley, New Jersey, 2002.
7. Alda, J.: *Laser and Gaussian Beam Propagation and Transformation*. Encyclopedia of Optical Engineering, Cambridge University Press, New York, pp. 999-1013, 2003.

# Network Configuration and Energy-Efficient Compression to Maximize Lifetime in Wireless Image Sensor Network

Ashraf Hossain

Department of Electronics & Communication Engineering, Aliah University  
DN-47, Sector-V, Salt Lake City, Kolkata-91, India  
E.mail: ashraf.ece@aliah.ac.in; hossain\_ashraf@rediffmail.com

**Abstract**—The nodes in a wireless image sensor network are generally energy constrained. The lifetime of such a network is limited by the energy dissipated by individual nodes during image processing and communication with other nodes. This paper provides an analytical framework for placing a number of camera nodes in a linear array such that each node dissipates the same energy per data gathering cycle while maintaining an acceptable image quality at the sink node. This approach ensures that all nodes run out of battery energy almost simultaneously and offers maximum network lifetime. Raw image captured by each camera node is processed locally to identify the important components to be forwarded to the sink. PSNR of the reconstructed image at the sink node is calculated for two test images.

**Key words:** Image sensor network; Image compression; Multi-hop; Inter-node distance; Network lifetime; Image quality

## 1. INTRODUCTION

A wireless image sensor network (WISN) consists of energy-constrained camera nodes that are deployed for a wide range of applications including surveillance, target tracking, environmental and habitat monitoring [1]. The feasibility of WISN is possible due to the progress of technology in image sensors and wireless communication [2–3]. The camera nodes are capable of transmitting and receiving of packets over a wireless link. Nodes are powered by battery that may not be replenished. Each node is also capable of processing its data locally.

The performance of WISN is limited by huge data load and battery energy. Thus, it is very important to compress the raw image captured by each camera nodes before transmission. The camera nodes are sometimes deployed in adverse conditions with limited energy. An accepted definition of lifetime of such a network is the time span from the instant when the network is deployed to the instant when the network is considered to be non-functional. A network is considered to be non-functional when a single sensor node dies, or a percentage of the nodes die [4].

In WISN, the information gathered by the camera nodes has to be sent to a sink node to make the conclusion about the activity of the area of interest. The communication range of the camera nodes is not large to reach a sink node. As a result, the mode of communication in this network is multi-hop. In a multi-hop linear wireless network, the nodes closer to the sink may have higher load of relaying packets as compared to the distant nodes. Hence the nodes closer to the sink are likely to get over-burdened and run out of their battery energy sooner. This type of linear sensor network has applications in highway traffic monitoring, border line surveillance, oil and natural gas pipeline monitoring etc.

Bhardwaj *et al.* [5] have considered a linear multi-hop network and proposed an upper bound on the lifetime of the network for an optimum number of intermediate nodes. However, this analysis is not applicable to situations where each node in the network senses and transmits its own packet, in addition to the packets received from other nodes. Shelby *et al.* [6], Haenggi [7] have studied a linear many-to-one multi-hop sensor network. However, they have not considered data compression.

In [4], we have considered a data gathering linear array of wireless sensor nodes over a finite distance. An exact placement of nodes has been obtained in order to ensure equal energy dissipation by each node in a data gathering cycle. It is found that maximum network lifetime is achieved when each node dissipates same energy per data gathering cycle.

Lecuire *et al.* [8] have studied the image transmission in linear array. They have proposed a semi-reliable image transmission strategy. Raw image is decomposed into a number of packets with different priority levels. This study is based on the transmission of image data from a source to a sink using intermediate nodes in a linear array. The intermediate relay node takes the decision of forwarding or discarding a packet depending on its state of energy. Thus, there is a chance of discarding a packet by an intermediate node. If a packet is discarded by an intermediate node near the sink then a significant amount of network energy will be wasted. The whole analysis of tradeoff between image quality and lifetime is done on the basis of number of hops. However, they have not considered many source nodes in the network. Wu and Abouzeid [9] and [10] have studied distributed image compression and transmission in wireless sensor network. Wu and Chen [11] have studied collaborative image coding for wireless sensor network.

In this paper, we extend our earlier work [4]. The semi-reliable image transmission has been incorporated only at the local source node. The raw image is locally processed to identify important component which need to be forwarded. The identification of important component is done on the basis of reconstructed image quality at the sink node. The lifetime of the network has been derived for two schemes of node placement. Peak signal-to-noise ratio (PSNR) of the reconstructed image at the sink node has also been calculated for two test images.

The rest of the paper is organized as follows. Section 2 gives the system description. Section 3 illustrates the image compression method using discrete wavelet transform (DWT). Node placement analysis for uniform energy dissipation is presented in

section 4. In section 5, we present the results and discussions. Finally, section 6 concludes the paper.

## 2. SYSTEM DESCRIPTION

A linear array of  $K$  wireless camera sensor nodes is considered with the sink at one end (Fig. 1). We assume that all the  $K$  camera nodes have same initial energy of  $E_0$  units. The distance between  $i^{\text{th}}$  camera node and  $(i-1)^{\text{th}}$  camera node is indicated as  $h_i$  units for  $2 \leq i \leq K$ . The distance between the sink and the 1<sup>st</sup> camera node is denoted as  $h_1$ . The farthest  $K^{\text{th}}$  camera node is at a distance of  $D$  units from the sink. For this model

$$\sum_{i=1}^K h_i = D \quad (1)$$

We consider a data-gathering network where each camera node takes a snapshot of its surroundings. Thus each camera generates an image of size  $M \times N$  pixels over a data gathering cycle of  $T_d$  second. Each pixel needs eight bit to represent it. The raw image is processed locally to reduce number of bits required to represent it. Let  $B$  be the packet size and  $l$  be the number of packets required to represent the compressed image. The compressed image is forwarded to the sink.

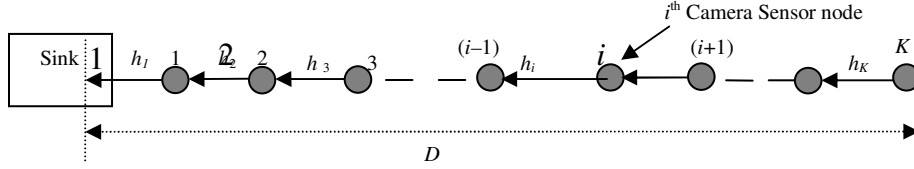


**Fig. 1.** Linear array of wireless camera sensor nodes.

A camera node sends its packets to the sink by using the nearest neighbour towards the sink as a repeater. Camera nodes closer to the sink are expected to forward all the packets towards the sink. No data aggregation is assumed at any node. We assume that each node can deal with  $P$  packets/second. This implies that  $PT_d \geq Kl$ .

### ***Image processing energy consumption model of a node***

The energy consumed in two dimensional discrete wavelet transform (2D-DWT) image processing per bit is [9]

$$E_{DWT} = \gamma \quad (2)$$

The energy consumed in quantization and coding per bit is

$$E_{ENT} = \delta \quad (3)$$

### Radio energy dissipation model of a node

The energy dissipation model (Fig. 2) for radio communication is assumed similar to [12] and [13], following which the energy consumed by the  $i^{\text{th}}$  camera node for transmitting a packet to the  $(i-1)^{\text{th}}$  camera node over a distance  $h_i$  is

$$E_{tx} = e_t + e_d h_i^n \quad (4)$$

Here  $e_t$  is the amount of energy spent per packet in the transmitter electronics circuitry and  $e_d h_i^n$  is the amount of energy necessary for transmitting a packet satisfactorily to the  $(i-1)^{\text{th}}$  camera node. The constant  $e_d$  is dependent on the transmit amplifier efficiency, antenna gains and other system parameters. The path loss exponent is  $n$  (usually  $2.0 \leq n \leq 4.0$ ) [14]. On the receiving end, the amount of energy spent to capture an incoming packet of  $B$  bits is  $e_r$  units. The radio is assumed to consume energy even during idle state, i.e., when the radio neither transmits nor receives. The idle state energy is equal to  $e_{id} T_{id} P$ , where  $T_{id}$  is the idle time and  $e_{id} = c.e_r$  is the idle state energy spent per packet duration, where  $0 < c \leq 1.0$  [12]. Perfect power control is employed i.e. the radio of the node is capable of adjusting its transmitting power according to the inter-node distance.

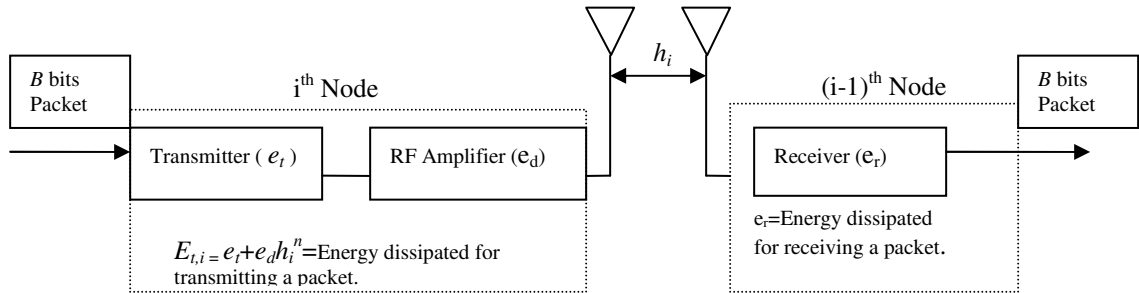


Fig. 2. Radio energy dissipation model.

Let the radio range of a camera node be  $R_r$  units. It is important to ensure  $h_i \leq R_r$ ,  $1 \leq i \leq K$  for maintaining connectivity of the array, if we do not consider the time varying nature of the wireless channel.

In the next section we describe the image compression principle.

### 3. IMAGE COMPRESSION USING 2D-DWT

In this section, we describe the basic principles of image compression using 2D-DWT. DWT has been chosen because it is more robust under transmission and decoding errors [9].

The block diagram of encoder and decoder for a wavelet based image compression system is shown in Fig. 3 [15]. The encoder consists of three components viz. forward wavelet transform, quantizer and symbol encoder. The image is transformed from its spatial domain by using wavelet transform to reduce the inter-pixel redundancies. Then the transform coefficients are quantized to reduce the psychovisual redundancies. The third component of the encoder (symbol encoder) creates a code to reduce coding redundancies. The compressed image is available at the output of symbol encoder. The decoder contains only two components: symbol decoder and inverse wavelet transform. The quantizer is omitted from the decoder because the operation of quantization is not reversible. The reconstructed image is available at the output of the inverse wavelet transform block.

In 2D-DWT based image decomposition scheme, the original image is decomposed into multiple levels of resolution. Fig. 4 illustrates a typical wavelet spectral decomposition. Fig. 4(b) is obtained from Fig. 4(a) by applying 2D-DWT. The original image is decomposed into four different components: approximation (CA1), horizontal (CH1), vertical (CV1) and diagonal (CD1). Fig. 4(c) is obtained from Fig. 4(b) where once again 2D-DWT is applied on the CA1 component.

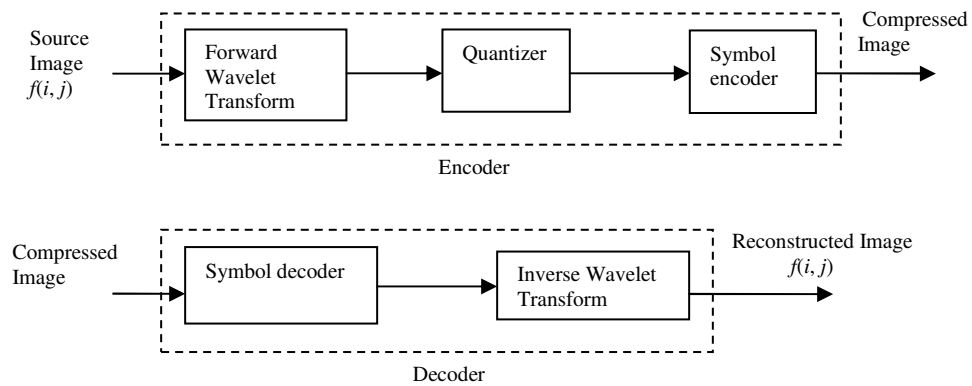


**Fig. 3.** A wavelet-based image compression system block diagram.

It has been observed that CA1 is the most important component. Thus, in our proposed image compression method, only CA1 has been used. One level 2D-DWT is employed on the raw image and only CA1 is quantized and applied to symbol encoder.

In the next section, we determine the distance  $h_i$  between neighboring camera nodes ( $1 \leq i \leq K$ ) such that each camera node spends same energy over a data gathering cycle. This constraint ensures that all the camera nodes get exhausted of their stored battery energy almost simultaneously. The lifetime that can be achieved by such an array of camera sensor nodes is of interest.

#### 4. PLACEMENT OF CAMERA NODES FOR EQUAL ENERGY DISSIPATION

According to the system model, the number of packets received by the  $i^{\text{th}}$  camera node per data gathering cycle is

$$A_r(i) = l(K-i), \text{ for } 1 \leq i \leq K \quad (5)$$

where  $l$  is the number of packets required to represent the compressed image.

The number of packets transmitted by the  $i^{\text{th}}$  camera node including its own packet per data gathering cycle is

$$A_t(i) = l\{(K-i)+1\} = A_r(i) + l, \text{ for } 1 \leq i \leq K \quad (6)$$

The duration of time the radio of the camera node is idle over a single data gathering cycle is

$$T_{id}(i) = \left( T_d - \frac{l\{2(K-i)+1\}}{P} \right), \text{ for } 1 \leq i \leq K \quad (7)$$

The energy consumed for image compression is

$$E_{image} = MNb\gamma \sum_{j=1}^T \frac{1}{4^{j-1}} + qMNb\delta \quad (8)$$

where  $M \times N$  is the image size and  $b$  is the number of bits per pixel.  $T$  is the number of 2D-DWT operation applied on the raw image.  $q$  is the coefficient of the important 2D-DWT components ( $0 < q < 1$ ). Each camera sensor node performs image compression operation for one raw image per data gathering cycle. Thus, each node dissipates  $E_{image}$  amount of energy per data gathering cycle for image processing purpose.

Following the energy consumption model, the total amount of energy spent by the  $i^{\text{th}}$  camera node per data gathering cycle is,

$$E(i) = l(K-i+1)(e_r + e_d h_i^n) + l(K-i)e_r + e_{id} \left( T_d - \frac{l\{2(K-i)+1\}}{P} \right) P + E_{image} \quad (9)$$

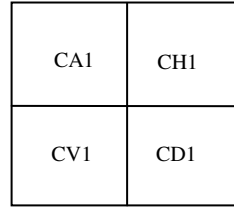
for  $1 \leq i \leq K$

Now, imposing the condition that all the nodes dissipate same energy  $E$  per data gathering cycle i.e.,  $E(i) = E$ , for  $1 \leq i \leq K$ , the inter-node distance  $h_i$  can be expressed as

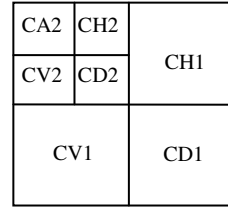
$$h_i = \left[ \frac{E - E_{image} - l(K-i)(e_t + e_r - 2e_{id}) - le_t + e_{id}(l - PT_d)}{l(K-i+1)e_d} \right]^{\frac{1}{n}}, 1 \leq i \leq K \quad (10)$$



(a)



(b)



(c)

**Fig. 4.** Wavelet spectral decomposition: (a) Original image; (b) Single level decomposition; (c) Two level decomposition.

It is interesting to note that each node dissipates a minimum energy  $E_{min}$  based on the values of system parameters as obtained from (10)

$$E_{min} = E_{image} + e_t l(K-2) + e_r l(K-1) + e_{id}(3l - PT_d - 2lK) \quad (11)$$

For known values of radio parameters, the feasible solutions of  $h_i$  is always possible when  $E > E_{min}$ , as has been implicitly assumed in (10).

In the next section, we present the results and discussions.

## 5. RESULTS AND DISCUSSIONS

In this section we present some numerical examples to study the issue of node placement and its effects on network lifetime and image quality. Specifically, the following issues are considered:

- (i) Node placement strategies to obtain desired energy consumption pattern (equal energy dissipation). Comparison of network lifetime achieved by different node placement schemes.
- (ii) Image quality at the sink node.

Let  $E_{th}$  be the threshold of residual energy below which a camera node becomes non-functional. Also, let  $E_{max}$  denote the maximum energy consumed by a camera node over a data gathering cycle in a sensor network. Since the duration of each data gathering cycle is  $T_d$  units, the network lifetime ( $T_{life}$ ) is

$$T_{life} = T_d \left( \frac{E_0 - E_{th}}{E_{max}} \right) \quad (12)$$

Image quality is expressed by peak signal-to-noise ratio (PSNR). PSNR is defined in decibel (dB) as

$$PSNR = 10 \log_{10} \left[ \frac{(2^b - 1)^2}{MSE} \right] \quad (13)$$

where,  $b$  is the number of bits per pixel and mean-squared error (MSE) for  $M \times N$  image is defined as

$$MSE = \frac{1}{MN} \sum_i \sum_j [f(i, j) - \hat{f}(i, j)]^2 \quad (14)$$

where,  $f(i, j)$  and  $\hat{f}(i, j)$  are the pixel values of the original and reconstructed images respectively.

For all the studies we consider a typical set of parameters as shown in Table 1. Following two schemes have been used for performance comparison:

*Scheme a*– All nodes have equal inter-node spacing i.e.  $h_i = D/K$ .

*Scheme b*– This is our proposed scheme. Here, the nodes are placed so that each node dissipates equal amount of energy in a data gathering cycle.

First we consider free space communication (i.e. path loss exponent,  $n = 2.0$ ) for ease of explanation. Typical values of other relevant parameters in Table 1 have been chosen following [9] and [12] closely. The radio parameters are given on a per packet basis.

**Table 1.** System parameters considered for performance analysis.

Parameter	Value
Link distance, $D$	1 000 m
Number of nodes, $K$	10
Packet length, $B$	512 bytes
Number of packets, $l$	15
Packet dealing rate of radio, $P$	1 packet/s
Duration of data gathering cycle, $T_d$	500 s
Path loss exponent, $n$	2.0
$e_t$	204.8 $\mu$ J/packet
$e_r$	204.8 $\mu$ J/packet
$e_d$ (for $n = 2$ )	409.6 nJ/packet/m <sup>2</sup>
$e_{id}$ (assuming $c = 0.9$ )	184.32 $\mu$ J/packet
DWT parameter, $\gamma$	220 nJ/bit
Quantization and entropy coding, $\delta$	20 nJ/bit
Raw image size, $M \times N$	256 $\times$ 256
Number of bits per pixel, $b$	8 bit
Number of 2D-DWT operation, $T$	1
Coefficient of important 2D-DWT components, $q$	0.25
Initial battery energy, $E_0$ (assuming 0.5 A-h and 3V battery)	5.4 kJ
Threshold energy, $E_{th}$	31 mJ
Radio Range, $R_r$	200 m

In our work, we consider a scenario where 10 camera nodes have been deployed over a 1 km link. The inter-node distance for 10 camera nodes are plotted for two cases in Fig. 5. For scheme-*a*, all the nodes are placed with equal inter-node distance (100 m). Scheme-*b* is plotted to obtain equal energy dissipation. Here, the inter-node distance is increasing with the node index (*i*). This is due to the fact that nodes closer to the sink forward more packets than the distant nodes from the sink. The balancing in energy consumption among the nodes is achieved only by assigning smaller inter-node distance to the nodes closer to the sink. The highest inter-node distance is set to the farthest node from the sink and it is equal to the radio range of the camera node. Thus connectivity of the link is justified in absence of any kind of fading.

The energy consumption profile for each node is shown in Fig. 6. *Curve-a* is obtained for equal inter-node distance. *Curve-b* is obtained for scheme-*b* where the camera nodes are placed judiciously so that each node dissipates equal energy. The node nearest to the sink consumes maximum energy per data gathering cycle for scheme-*a*. Thus, it will limit the lifetime of the network. On the other hand, all the nodes dissipate

equal energy per data gathering cycle for scheme–b. Thus all the nodes will get exhausted at the same time and offers maximum lifetime.

The residual energy profile for two placement schemes has been compared in Fig. 7. In scheme–b, all the camera nodes dissipate almost all the battery energy. Thus there is no wastage of energy before the network be adjudged to be a nonfunctional. In scheme–a, the farthest node from the sink has the maximum residual energy which has been wasted as the network be considered as nonfunctional when nodes closest to the sink has no left over battery energy.

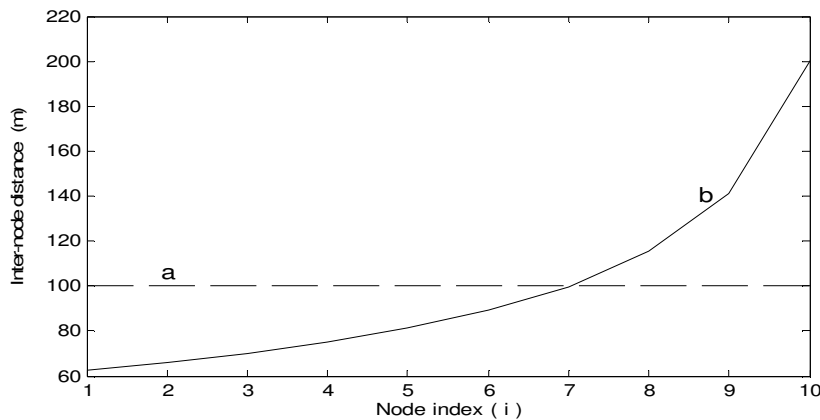


**Fig. 5.** Inter-node spacing for different node placement ( $K = 10$ ,  $D = 1\ 000$  m,  $n = 2.0$ ): (a) for scheme–a; (b) for scheme–b.

We have tested the image quality of the reconstructed image at the sink. The raw test image Peppers is considered in our study. The test image has a size of  $256 \times 256$  pixels. Each pixel is originally encoded to 8 bits. In our compression method, we apply one time ( $T = 1$ ) 2D–DWT on the raw image and neglect all the components except CA1. Then CA1 is quantized to 4 bits by uniform quantizer. We have assumed that channel is error free. Thus no transmission noise has been incorporated. The PSNR values achieved at the sink node is 24.79 dB for the test image. The compression ratio achieved by our compression method is about 8.61 for Peppers image. The reconstructed test images are shown in Fig. 8. The lifetime for the two node placement schemes has been calculated. Schemes–a and b provide the network lifetime of about 37.6 days and 68.5 days respectively. This result shows scheme –b outperforms scheme –a.

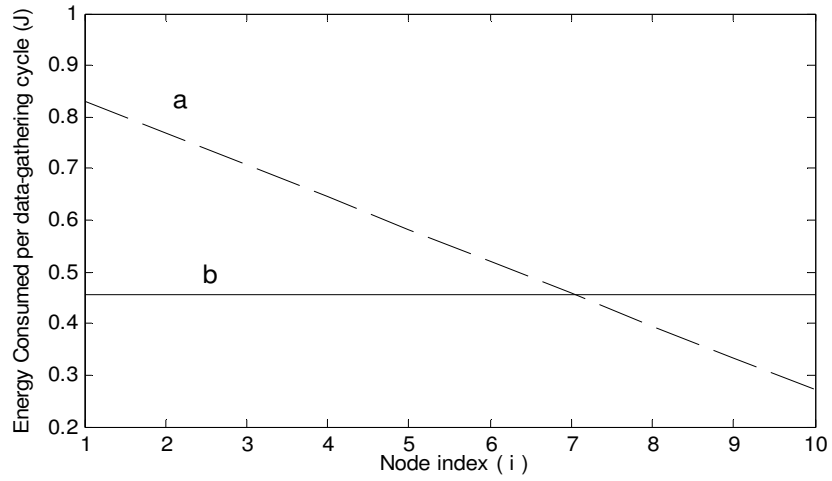


**Fig. 6.** Energy consumption pattern for different node placement ( $K = 10$ ,  $D = 1\ 000$  m,  $n = 2.0$ ): (a) for scheme-a; (b) for scheme-b.

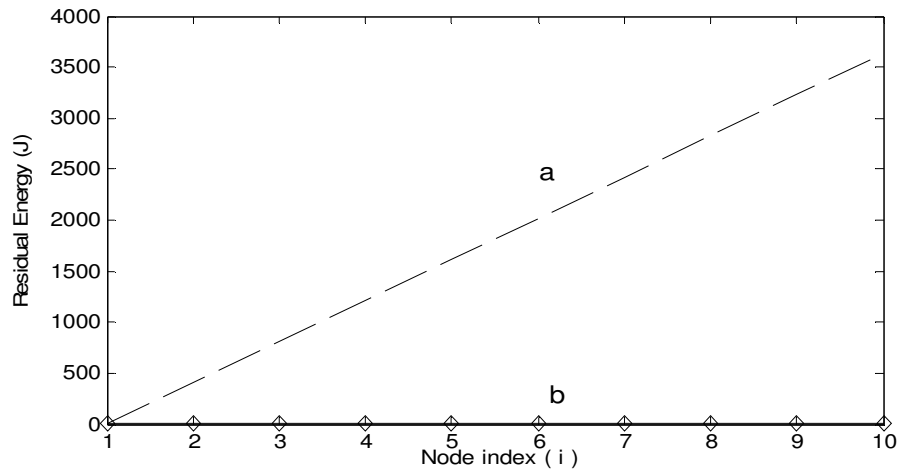


**Fig. 7.** Residual energy of the network ( $D = 1\ 000$  m,  $K = 10$ ,  $n = 2.0$ ): (a) for scheme-a; (b) for scheme-b.



**Fig. 8.** (a) Original Peppers image; (b) Reconstructed Peppers image with PSNR is 24.79 dB.

## 6. CONCLUSION

In this paper we have considered a linear array of  $K$  wireless camera sensor nodes over a distance ( $D$ ). An exact placement of camera nodes has been obtained in order to ensure equal energy dissipation by each camera node in a data gathering cycle. The raw image captured by each camera is processed by 2D-DWT to identify important components. The important components are forwarded to the sink for analyzing the activity over the area of interest. We have compared network lifetime that provides our proposed scheme with another scheme. It is found that maximum network lifetime is achieved when each node dissipates same energy per data gathering cycle. PSNR of the reconstructed image is also calculated at the sink node for test image.

## 7. REFERENCES

1. Aswin C. Sankaranarayanan, Ashok Veeraraghavan and Rama Chellappa, "Object detection, tracking and recognition for multiple smart cameras", *Proceedings of the IEEE*, vol. 96, no. 10, pp. 1606–1624, October 2008.
2. M. Rahimi, R. Baer, O. I. Iroezzi, J. C. Garcia, J. Warrior, D. Estrin and M. B. Srivastava, "Cyclops: in situ image sensing and interpretation in wireless sensor

- networks”, in the Proceedings of the 3<sup>rd</sup> *ACM Conference on Embedded Networked Sensor Systems (SenSys 2005)*, pp. 192-204, San Diego, USA, November 2–4, 2005.
3. E. Culurciello and A. G. Andreou, “CMOS image sensors for sensor networks”, *Analog Integrated Circuits and signal Processing*, vol. 49, no. 1, pp. 39–51, 2006.
  4. Ashraf Hossain, T. Radhika, S. Chakrabarti and P. K. Biswas, “An approach to increase the lifetime of a linear array of wireless sensor nodes”, *International Journal of Wireless Information Networks (IJWIN)*, Springer Netherlands, vol.15, no. 2, pp. 72–81, June 2008.
  5. Manish Bhardwaj, Timothy Garnett and Anantha P. Chandrakasan, “Upper bounds on the lifetime of sensor networks”, in the Proceedings of the *IEEE International Conference on Communications (ICC 2001)*, Helsinki, Finland, vol. 3, pp. 785–790, June 2001.
  6. Zach Shelby, Carlos Pomalaza-Ráez, Heikki Karvonen and Jussi Haapola, “Energy optimization in multihop wireless embedded and sensor networks”, *International Journal of Wireless Information Networks*, Springer Netherlands, vol. 12, no. 1, pp. 11–21, January 2005.
  7. Martin Haenggi, “Energy-balancing strategies for wireless sensor networks”, in the Proceedings of the *IEEE International Symposium on Circuits and Systems (ISCAS 2003)*, Bangkok, Thailand, vol. 4, pp. IV 828–IV 831, May 25–28, 2003.
  8. Vincent Lecuire, Cristian Duran-Faundez and Nicolas Krommenacker, “Energy-efficient transmission of wavelet-based images in wireless sensor networks”, *EURASIP Journal on Image and Video Processing*, vol. 2007, article ID 47345, 11 pages, 2007.
  9. H. Wu and A. A. Abouzeid, “Energy efficient distributed image compression in resource-constrained multihop wireless networks”, *Computer Communications*, Elsevier Science, vol. 28, no. 14, pp. 1658–1668, September, 2005.
  10. H. Wu and A. A. Abouzeid, “Error resilient image transport in wireless sensor networks”, *Computer Networks*, Elsevier Science, vol. 50, no. 15, pp. 2873–2887, October, 2006.
  11. M. Wu and C. W. Chen, “Collaborative image coding and transmission over wireless sensor networks”, *EURASIP Journal on Advances in Signal Processing*, vol. 2007, article ID 70481, 9 pages, 2007.
  12. Q. Gao, K.J. Blow, D.J. Holding, I.W. Marshall and X.H. Peng, “Radio range adjustment for energy efficient wireless sensor networks”, *Ad-Hoc Networks Journal*, Elsevier Science, vol. 4, issue 1, pp. 75–82, January 2006.
  13. Wendi Heinzelman, Anantha P. Chandrakasan and Hari Balakrishnan, “An application-specific protocol architecture for wireless microsensor networks”, *IEEE Transaction on Wireless Communications*, vol. 1, no. 4, pp. 660–670, October 2002.
  14. Theodore S. Rappaport, *Wireless communications: principles and practice*, Second Edition, 2005, Prentice-Hall of India Private Limited, New Delhi–110 001, India.
  15. Rafael C. Gonzalez, Richard E. Woods and Steven L. Eddins, *Digital image processing using MATLAB*, Low price edition 2006, Pearson Education, New Delhi–110 001, India.

# Automated Laser Reflectometer Imaging System

Samrat<sup>1</sup>, Indumathi.J<sup>2</sup>

<sup>1</sup>B.Tech, Biomedical Engineering, <sup>2</sup>Assistant professor  
Centre for Biomedical Research,  
VIT University, Vellore-632014, Tamilnadu, India

**Abstract:** A unique scanner is developed for scanning the curved surface of the body using multi-probe laser reflectometer imaging system. The scanner is designed using a steel frame and two synchronized servomotors. A programmable circuit drives the motors. With laser scanning being noninvasive, this scanner is totally automated, thereby increasing the accuracy and agility of the entire scanning process.

## 1. INTRODUCTION

Non-invasive diagnostic technology has gained significant advantages over the general diagnostic technology using ionizing radiation as the principle for diagnosis. Laser is widely advocated for manipulation in noninvasive methodologies. Few areas, involving Lasers are well established while the others are still under research. Laser could be used for medical purposes only on favorable interactions between human tissue and Laser radiation. The success of this interaction depends on the wavelength, absorption [1] and scattering of Laser. Being more specific, Laser radiation within the definite optical window (600 – 1300 nm) can penetrate deep into soft tissues [2], owing to the low absorption and high scattering of the Laser.

There are different layers of tissue; epidermis, dermis, subcutaneous layer, muscle and bone with their associated blood flow. All of which have different characteristic properties towards Laser radiation. They contribute to the scattering, absorption and transmission of this radiation. However, for diagnostic purpose only two parameters, namely absorption and scattering play an important role.

The coefficient of absorption and scattering within the mentioned layers varies and in the presence of an abnormality, the back-scattered radiation deviates from the normal value. This deviation is exploited in diagnostic procedures. In the current work, our aim was to develop a scanner on to which the laser probe could be fixed, making the scanning process completely automatic. We also propose that this automation in scanning could help in the reduction of error.

## 2. MATERIALS AND DESIGN

### A. Scanner frame:

The entire frame is constructed using steel and iron. The schematic diagram of the scanner is shown in Fig.1. The constructed design is a smaller version designed to scan the human hand. A similar upscale version could be used to scan the entire body.

Our design incorporates two pairs of concentric rings. The first pair of ring is oriented towards the palm (or fist) The dimensions of the first pair of rings is as follows: Breath-6", Diameter of inner ring-6", Diameter of outer ring-7.5". The second pair of rings is placed inner to the outer ones and the diagram of inner ring is shown in Fig. 2.

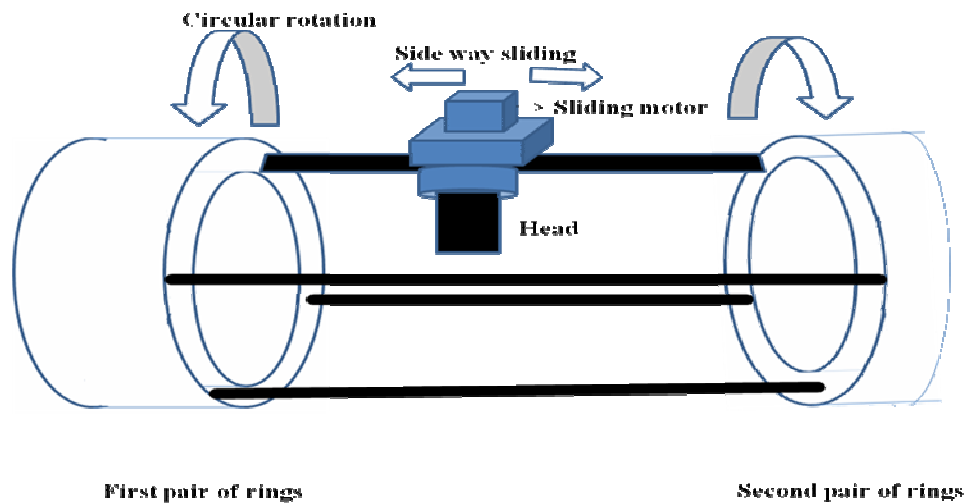


**Fig.1.** Schematic Diagram of Laser Reflectometer Scanner

A plate with a central hole is attached to the inner ring. This hole is used to fix the inner motor, which would provide rotational motion to the spokes. One main (thicker) and three supportive (thin) spokes are connected with the motor. The rotating axis of the motor is outside rather than inside as the hand itself hinders it. In order to overcome this problem, a specialized design with concentric rings is used to instigate an unhindered rotation. The outer ring is used to provide support for the rotation of the spokes and also help in the placement of the scanner and stabilize its support. The spokes are confined in between the two rings. Internally two pairs of rail are made with a wheeled arrangement to aid in the rotation of the spokes. The arrangement for the rotation is shown in Fig.3.

The second pair of ring is used as a supportive ring arrangement. When the hand is inserted inside the system it helps in clamping the arm to avoid unnecessary movement. Also, an extra smooth movement is provided to the spokes by the second pair of rings so that the spokes could rotate freely.

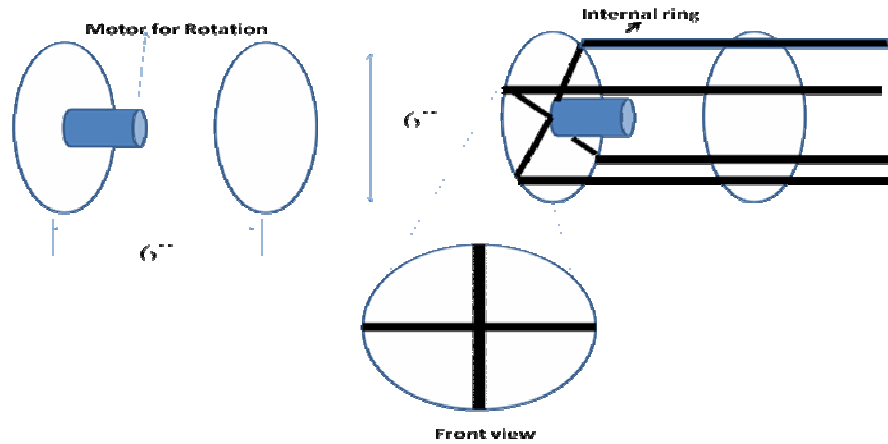


**Fig.2.** Inner Ring (First pair) with Dimension and spoke arrangement

A sliding gear is attached with the main spoke. A specialized head like structure is made to slide on the gears with the help of the motor. The head contains a motor for sliding with an intricate arrangement, facilitating proper functioning of the Laser probe. The schematic diagram of the main spoke with head is shown in Fig.4.

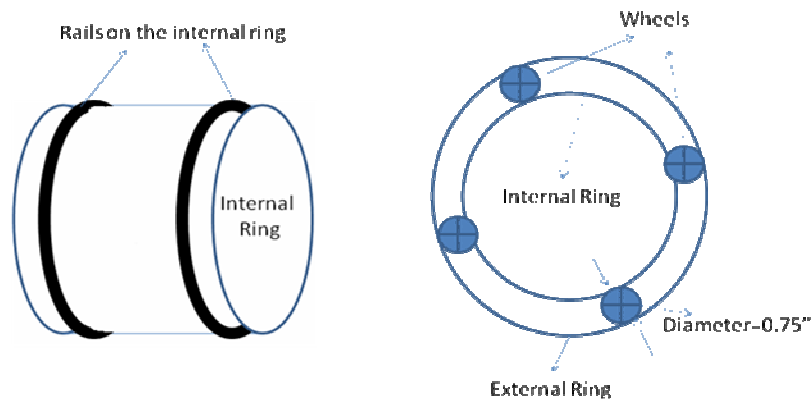


**Fig.3.** Inner Ring with rails (left), confined wheels between two coaxial rings whose axis is made by the spokes (right).

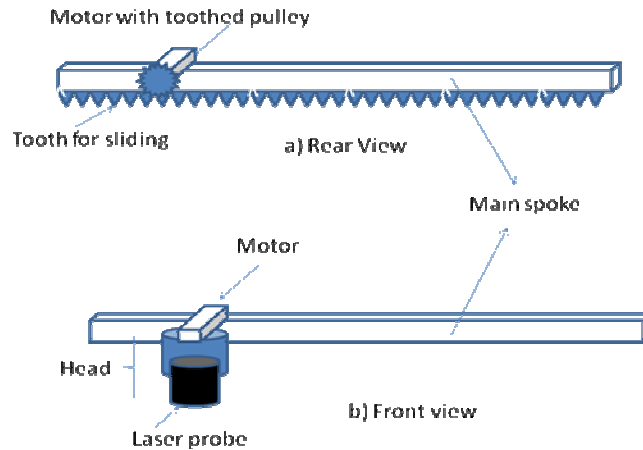


**Fig.4.** a) Rear View of main spoke. b) Front View with head arrangement

The head system is made such that it is free to move with the help of motor. It can move left and right, enabling it to scan the entire length (of the hand). The laser probe is fixed to the main head with the help of springs (of low spring constant), so that when it comes in contact with the soft tissue it automatically takes the desired compression to maintain a right angle with the surface (maintaining this right angle is one of the major necessity of the probe). The tip of the probe is also connected to a ring of 1mm diameter so that it always maintains a constant distance of 1mm from the skin surface.

#### **B. Motors:**

Two servo-controlled DC motor are used for this scanner. Motor I is used to provide circular motion around the hand so that it can scan the entire curvature. Motor II is used to provide the translatory motion to the head so that after completion of one revolution it shifts its position for a distance equivalent to the diameter of the laser probe (i.e. 1"). It is required to complete the entire revolution in the step of 1-5mm. The average wrist circumference is 17 cm approximately and the biceps circumference is 30 cm (average). Considering both these circumferences, the numbers of steps of motor I is taken to be 60. Thus, for entire forelimb the scanning distance comes under 1-5mm. As the motor I completes one revolution, the power supply to it is discontinued and the signal is given to the motor II to shift the position of head. As the shift is completed the rotation process again started. This process is continued until the scanner is done with the whole limb. A reset button is also provided to bring the head to its original position. The timing diagram for both the motors is shown in Fig. 5.

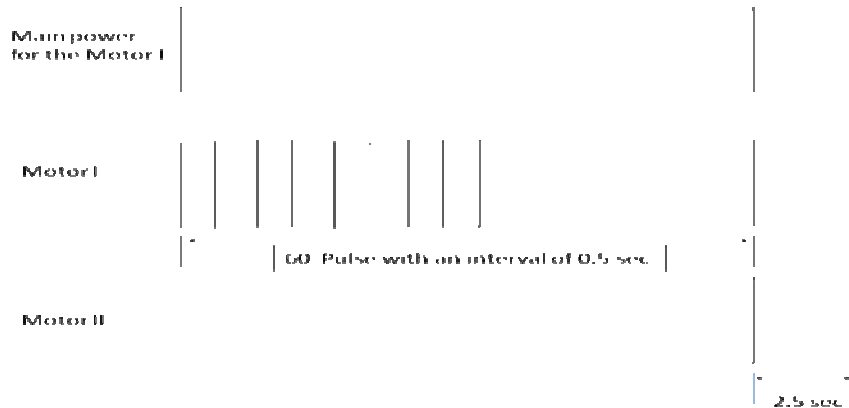


**Fig.5.**Timing Graph of motor.

### **C. Demonstration of the scanner on a subject's hand**

The entire setup is placed on the table. The subject is to be seated on a chair of height such that the hand of the subject can be inserted inside the machine comfortably. After insertion there must be no discomfort and hand must be parallel to the table surface. The subject is asked to clench his or her hand, enabling an easy fixture inside the inner ring with the help of a clamp. On cross checking that the head is properly placed on the hand surface, the instrument is turned on, initialing the motion of the Laser head over the hand. Any minor technical error would be corrected.

## **3. RESULT AND DISCUSSION**

When a laser beam is directed towards a tissue 3% of incident light [3] is reflected. The remaining light in the tissue is absorbed and scattering takes place. The depth of penetration is the function of the wavelength of the Laser [4]. Median filtration [5], a non-linear filtration is performed for shaping the edge, as this does not introduce a fake abnormality. The normal layer of the hand absorbs less and affected layer would absorb more. Thus, this gives a darker color to the affected layer and lighter color to the normal layer. Intensity and other characteristics of the spot help in identifying the type of abnormality. Similar kind of work was done by Mr. T. Arun Kumar et al [6].

The functioning of the computer based scanning system was assessed using a phantom with abnormalities, based on a manual basis. The Monte Carlo Simulation technique [7] was used to perform this. The scanning process was also performed on a subject's hand. The result of the scanning was displayed on the screen without any abnormality. In the phantom, scanning abnormalities were made intentionally to observe the defects shown by the computer. The absorption and scattering capacity of the tissue is

usually altered due to any kind of abnormality. Since there is was no abnormality in the subjects hand the 3D image generated by the computer was found to have no color change. As efficient data collection is required for accurate diagnosis, this scanner could help with better agility and dexterity in the diagnosis.

#### 4. CONCLUSION

Different kind of abnormalities could be detectable using this technology. Complete automation of the system has made data acquisition more accurate, thereby increasing the sensitivity of the diagnosis. In the future, an upscale model of the same automated instrument with specific design modification could be setup to acquire an entire body scan.

#### 5. REFERENCES

1. R. S. Khandpur, *Handbook of Biomedical Instrumentation*, Second Edition, pp. 743, 2003
2. L. Goldman, *The biomedical laser technology and clinical applications*, Springer Verlag, Berlin, 1981.
- 3-4. A. J. Welch, Jorge H. Torres, Wai-Fung Cheong, *Laser Physics and Laser-Tissue Interaction*, Tex Heart Inst J., 16(3), pp. 141–149. 1989.
5. A. K. Jain, *Fundamentals of digital image processing*, Prentice Hall, Englewood Cliffs, NJ 1989.
6. T. Arun Kumar, Megha Singh & M Kumaravel, *Laser Reflectance Imaging of Curved Tissueequivalent Phantoms*, Engineering in Medicine and Biology 27th Annual Conference Shanghai, China, September 1-4, 2005
7. D. Kumar, S. Chacko and M. Singh, *Monte Carlo simulation of photon scattering in biological tissue models*, Indian J Biochem. Biophys. 26, 330. 1999.

# Evaluation of Power Consumption in Adiabatic Universal Gates

Samik Samanta (Member IEEE, Member IAENG)

Assistant Professor ,Department of Electronics & Communication Engineering  
Institute of Technology & Marine Engineering, West Bengal, India.  
samik\_samanta@rediffmail.com

**Abstract:** Demands for low power and low noise digital circuits have motivated VLSI designers to explore new approaches to the design of VLSI circuits. Energy recovery logic is a new promising approach, which has been originally developed for low power digital circuits. Energy recovery logic is also known as adiabatic logic. Adiabatic circuits achieve low energy dissipation by restricting current to flow across devices with low voltage drop and by recycling the dissipated heat. In this paper we have calculated the power dissipation of adiabatic universal gates using VLSI CAD tool and compare it with conventional universal gates.

## 1. INTRODUCTION

The power dissipation is a very important concern in the performance of VLSI circuits. Power dissipation increases proportionally with the operating frequency. Reducing the power dissipation is the main aim of low power portable circuit design. Several methods for low power circuit design like low power supply voltage, ac power supply have been adopted. Reducing power supply voltage is an efficient circuit design method, but it is limited by noise margin and threshold voltage. Using the ac power supply can recover charge to original power supply, which is an advantage for low power circuit design [1]. We call the method namely adiabatic logic. Although adiabatic circuits consume zero power theoretically, they show nonzero power consumption due to resistance in switching the transistor but the energy loss is very lower than standard CMOS circuit [3]. In CMOS dynamic power dissipation plays a vital role over other power dissipations like short circuit power dissipation and static power dissipation.

Let us take fig 1, here a load capacitance is charged using a switch and a source. We know,  $Q = CV$  where  $Q$  is the charge transferred to the load,  $C$  is the value of the load capacitance.

Again,  $I = Q/T = CV/T$  where  $I$  is the current.

Dissipated energy:  $E = I^2RT = (CV/T)^2RT = (2RC/T)(1/2CV^2)$

This is better than CMOS by a factor  $(2RC/T)$ . Here  $T$  is the charging time.

In adiabatic circuits the load capacitance is charged by a constant-current source whereas in conventional CMOS logic we use constant voltage source to charge the load capacitance [3].

In adiabatic switching power dissipation is asymptotically proportional to the inverse of the charging time and directly proportional to the  $R$  and  $C$  values. So increasing  $T$  will reduce power dissipation. In conventional switching energy dissipated per discharge cycle is independent of time period [4].

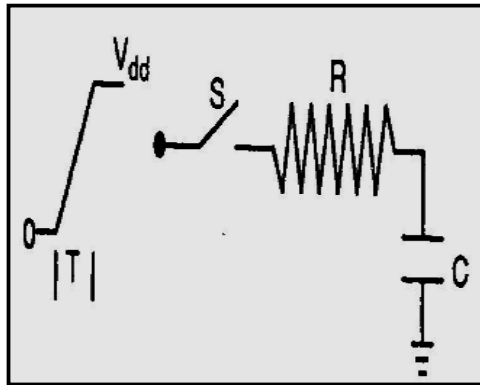


Fig. 1

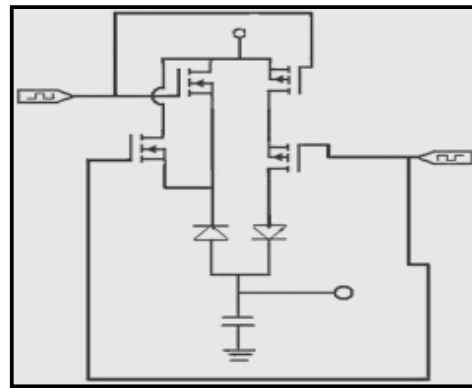


Fig:2

## 2. ADIABATIC GATES

Here we are presenting the universal gates using adiabatic logic. Fig2 shows the circuit diagram of adiabatic nor gate. This circuit consists of two branches in parallel. The first branch consists of two P-channel MOSFETS and a diode in series. The second branch consists of two N-channel MOSFETS in parallel, connected in series with a diode. The two parallel branches are connected in series with the load capacitance. Fig 3 shows the circuit diagram of adiabatic NAND gate. This circuit consists of two branches in parallel. The first branch consists of two P-channel MOSFETS in parallel and a diode in series. The second branch consists of two N-channel MOSFETS and a diode in series. The two parallel branches are connected in series with the load capacitance.

## 3. SIMULATION RESULTS

We have simulated the conventional gates, and compare with the simulation results of adiabatic gates. The simulation is done using SPICE simulator and cadence simulation tools. We have used 75nm technology. The power dissipation of various gates is shown in the table. We have taken various frequencies for evaluating the power dissipation.

**Table: 1**

<i>Gates</i>	<i>Frequency</i>		
	<b>20MHz</b>	<b>50MHz</b>	<b>100MHz</b>
<b>Conventional NOR gate</b>	30 $\mu$ W	45 $\mu$ W	56 $\mu$ W
<b>Conventional NAND gate</b>	25 $\mu$ W	36 $\mu$ W	61 $\mu$ W
<b>Adiabatic NOR gate</b>	14 $\mu$ W	22 $\mu$ W	28 $\mu$ W
<b>Adiabatic NAND gate</b>	10 $\mu$ W	14 $\mu$ W	21 $\mu$ W

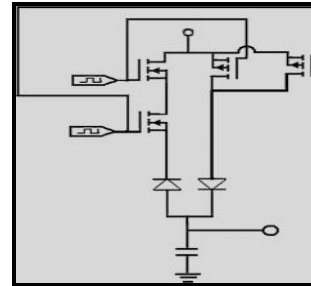


**Fig: 3.**

#### 4. CONCLUSION

From the results we can see that adiabatic gates have nearly  $1/3^{\text{rd}}$  power dissipation compare to conventional gates. These circuits can also be used in building hierarchical circuits as the input and output logic levels. Further, all the circuits can be operated with a single power supply.

#### 5. REFERENCES

1. N. Weste and K. Eshraghian, Principles of CMOS VLSI Design: A Systems Perspective, 2nd ed. New York: Addison - Wesley, 1993.
2. M. Pedram, "Power minimization in IC design: principles and applications," ACM Transactions on Design Automation of Electronic Systems, 1(1): 3-56, January 1996.
3. W. C. Athas, L. J. Svensson, J. G. Koller, et al., "Low power digital systems based on adiabatic-switching principles," IEEE Trans. on VLSI Systems, 2(4): 398-407, December 1994.

4. J. S. Denker, "A review of adiabatic computing," in Proc. of the Symposium on Low Power Electronics, 1994, pp. 94-97.
5. Jan Rabey, Massoud Pedram, Low power Design Methodologies:5-7, Kluwer Academic Publishers, 5<sup>th</sup> edition. 2002
6. PD Khandekar, S Subbaraman, Manish Patil "Low power Digital Design Using Energy-Recovery Adiabatic Logic", International Journal of Engineering Research and Industrial Applications, Vol-1, No.III, pp199-208
7. A.G. Dickinson, J.S. Denker, "Adiabatic dynamic logic", IEEE J.S.S.C., Vol. 30, pp. 311-315, March 1995.
8. A. Kamer, J. S. Denker, B. Flower, et al., "2ND order adiabatic computation with 2N-2P and 2N-2N2P logic circuits," in Proc. of the International Symposium on Low Power Design, 1995, pp. 191-196.

## Dual Band Notched Fractal Ultra-Wideband Antenna

Anirban Karmakar<sup>1</sup>, Shabana Huda<sup>2</sup>

Department of Electronics & Communication Engineering,  
Netaji Subhash Engineering College,  
Kolkata, West Bengal, India

<sup>1</sup>anirban.ece@gmail.com, <sup>2</sup>shabanahuda@gmail.com

**Abstract.** A dual frequency notched ultra-wideband (UWB) fractal printed antenna is presented and analyzed in detail. By introducing Sierpinski carpet fractal, the size of the antenna is reduced significantly and impedance bandwidth is improved. Two open-ended quarter wavelength slots are etched on the ground plane to create the first notched band in 3.3 - 3.7 GHz for WiMAX system. In addition, two half-wavelength U shape slots are cut in the ground plane to generate the second notch band in 5.15-5.825 GHz for IEEE802.11a and HIPERLAN/2. Several properties of the antenna such as impedance bandwidth, frequency notched characteristics, radiation patterns and gain, have been simulated. Two sharp frequency notched bands are achieved, and relatively stable, omnidirectional radiation performance over the entire frequency range has also been obtained.

**Keywords:** Fractal, sierpinski carpet, dual frequency notched, printed antenna, ultra-wideband (UWB)

### 1. INTRODUCTION

Development of components for ultra wideband (UWB) communication band has attracted a lot of attention with the opening up of the UWB bands for 3.1-10.6 GHz by FCC in 2002[1] which is used for high data-rate wireless communication, high-accuracy radar, and imaging systems. The UWB antenna has drawn heavy attention from researchers which displays desirable characteristics such as compact size, low cost, and good omni-directional radiation pattern [2]. However, there is an issue of a possible electromagnetic interference, as over the allocated wide bandwidth of the UWB system, some narrow bands for other communication systems exist, such as WiMAX operating in 3.3-3.7 GHz, IEEE802.11a and HIPERLAN/2 operating in 5.15- 5.825 GHz. UWB antennas with band-notched function have been reported, mostly with single notched band [3-5] in 5.15-5.825 GHz. On the other hand, it is well known that one of the most important characteristics of fractals is size reduction and space-filling. Therefore, traditional fractals have been used to design compact antennas for multiband or broadband operation [6–8]. Based on these concepts, a compact thinned fractal UWB antenna is designed with two band notch characteristics.

## 2. ANTENNA DESIGN

The schematic diagram of the proposed antenna is shown in Fig.1. The antenna is fed by a 50ohm microstrip line like conventional wide slot antennas. The radiator has a dimension of  $(13 \times 10) \text{ mm}^2$  ( $W_0 \times L_0$ ) with feed length  $L_f = 16.5 \text{ mm}$  and feed width  $w_f = 1.5 \text{ mm}$  as shown in figure1 (a). However, a second-order sierpinski carpet fractal concept [6] is used in the antenna and as well as in the ground plane.

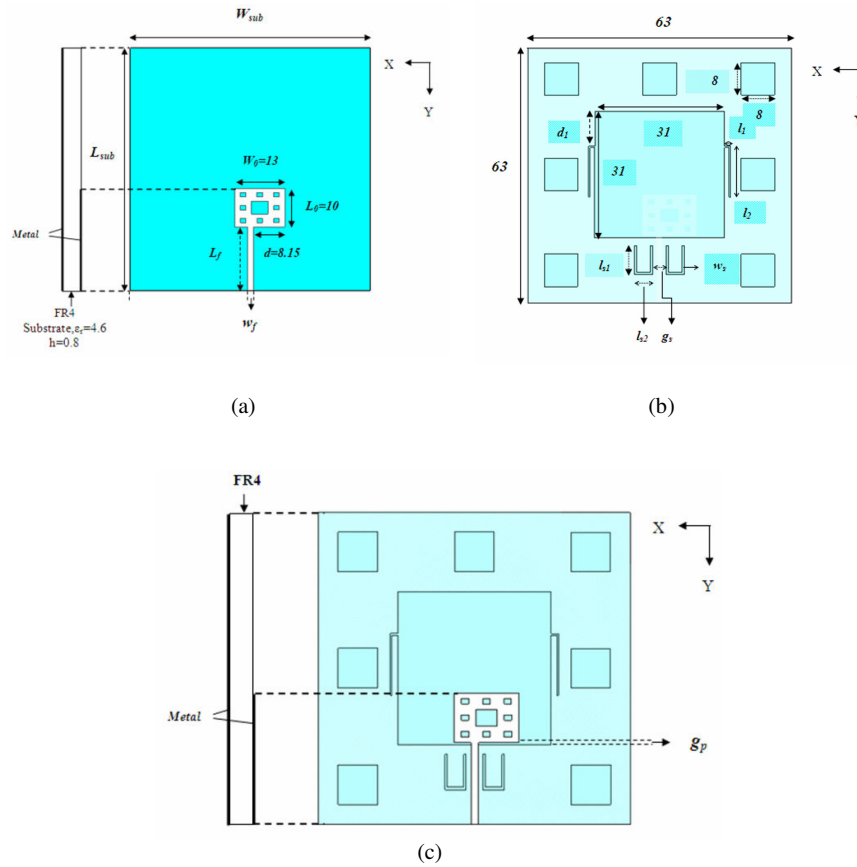


**Fig.1** (a) Fractal antenna of second iterative structure (b) Fractal ground plane of second iterative structure with band notch structures (c) total antenna structure

The antenna has a volume of  $(63 \times 63 \times 0.8) \text{ mm}^3$  ( $W_{\text{sub}} \times L_{\text{sub}} \times h$ ) on FR4 substrate with a relative dielectric constant ( $\epsilon_r$ ) of 4.6 and loss tangent of 0.02. The antenna has a ground plane which is given a modified sierpinski carpet [6] shape whose detail dimensions are shown in figure 1(b). Two U shape slots are etched out from the lower side of the ground plane whose lengths are nearest to half wave length of the center frequency of the corresponding notch band which is 5.5GHz. The total length ( $2l_{s1} + l_{s2}$ ) of each slot is 18.5mm and width ( $w_s$ ) is 0.5mm. Again two inverted open ended L shape slots are etched on the middle of the ground plane and each has a width of 0.35mm and length ( $l_2 + l_1$ ) of 14mm which is nearest to quarter wavelength at the center notch frequency at 3.55GHz. for each notch band. Two notches are etched to produce sharp notch at the corresponding band.

### 3. RESULTS AND DISCUSSION

In this paper, all the simulations are done based on CST Microwave Studio™. Simulated  $S_{11}$  and VSWR characteristics of the proposed antenna are shown in Fig.2 respectively. The proposed antenna's operating band covers wide frequency range starting from 3GHz which also covers the range for UWB. It is seen that the antenna successfully blocks out the 3.3 - 3.7 GHz for WiMAX system and 5.15 - 5.825 GHz for WLAN but still performs good impedance -matching at other frequency in the UWB band.

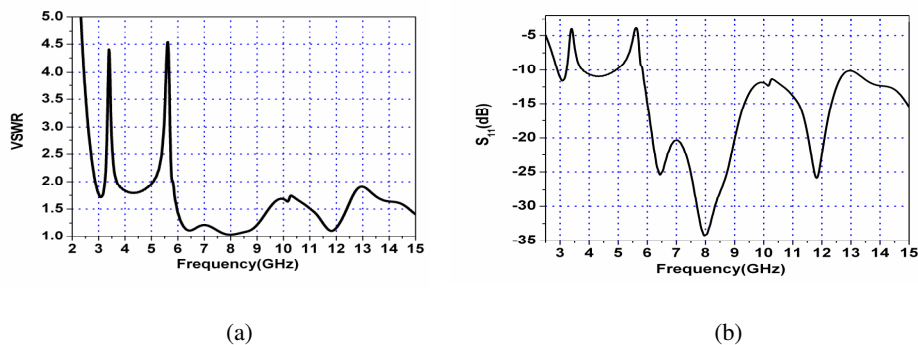


**Fig.2.** (a)  $S_{11}$  and (b) VSWR characteristics of the proposed antenna.

The surface current distributions on the radiating patch and on the ground plane of the antenna at four different frequencies are shown in Fig. 3. At a pass-band frequency of 6.4 GHz and 8 GHz (outside the notched band), the distribution of the surface current is mainly concentrated in the feed, radiator and on the inner edge of the ground plane as shown in Fig. 3(a) and 3(b). On the other hand, in Fig. 3(c) and 3(d), we can see stronger

current distributions concentrated near the edges of slots at the center frequency of the corresponding notched bands.

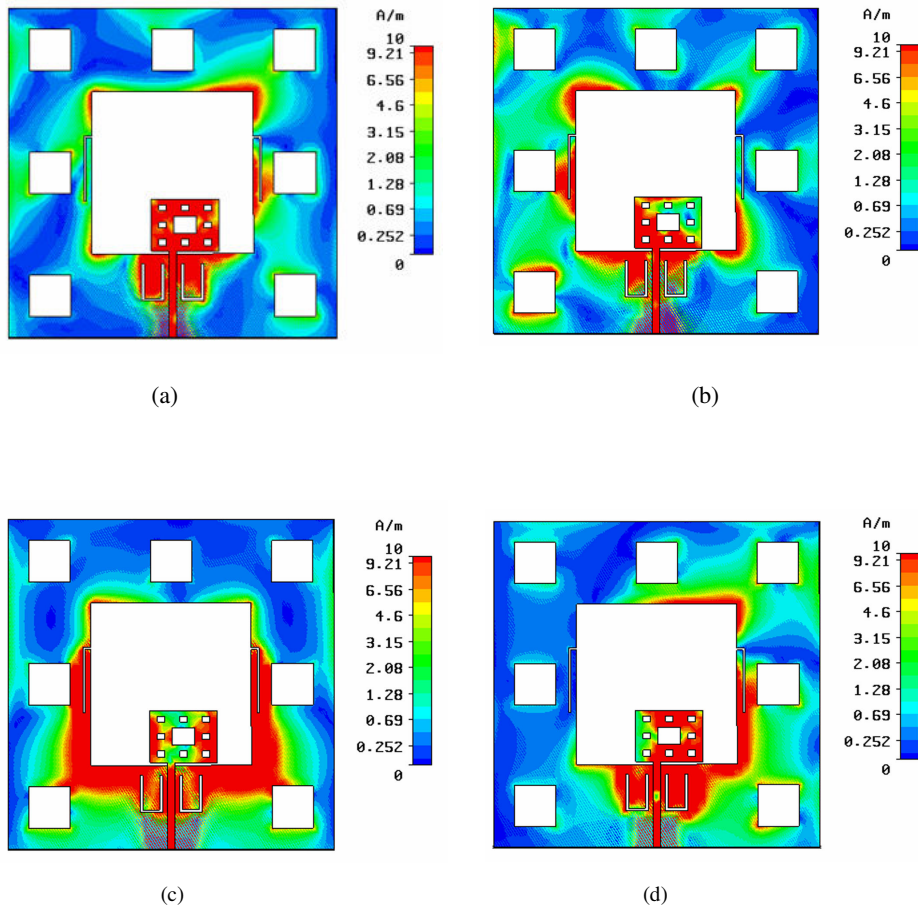


**Fig. 3.** Surface current distributions on the radiating patch at (a) pass-band frequency, 6.4 GHz (b) pass-band frequency, 8 GHz (c) the first notched band, 3.5 GHz, (d) the second notched band, 5.5 GHz

The simulated radiation patterns at 4.5 GHz, 6.4 GHz, 8 GHz are plotted in Fig.4 respectively. The antenna exhibits a stable omnidirectional radiation behavior across the UWB band.

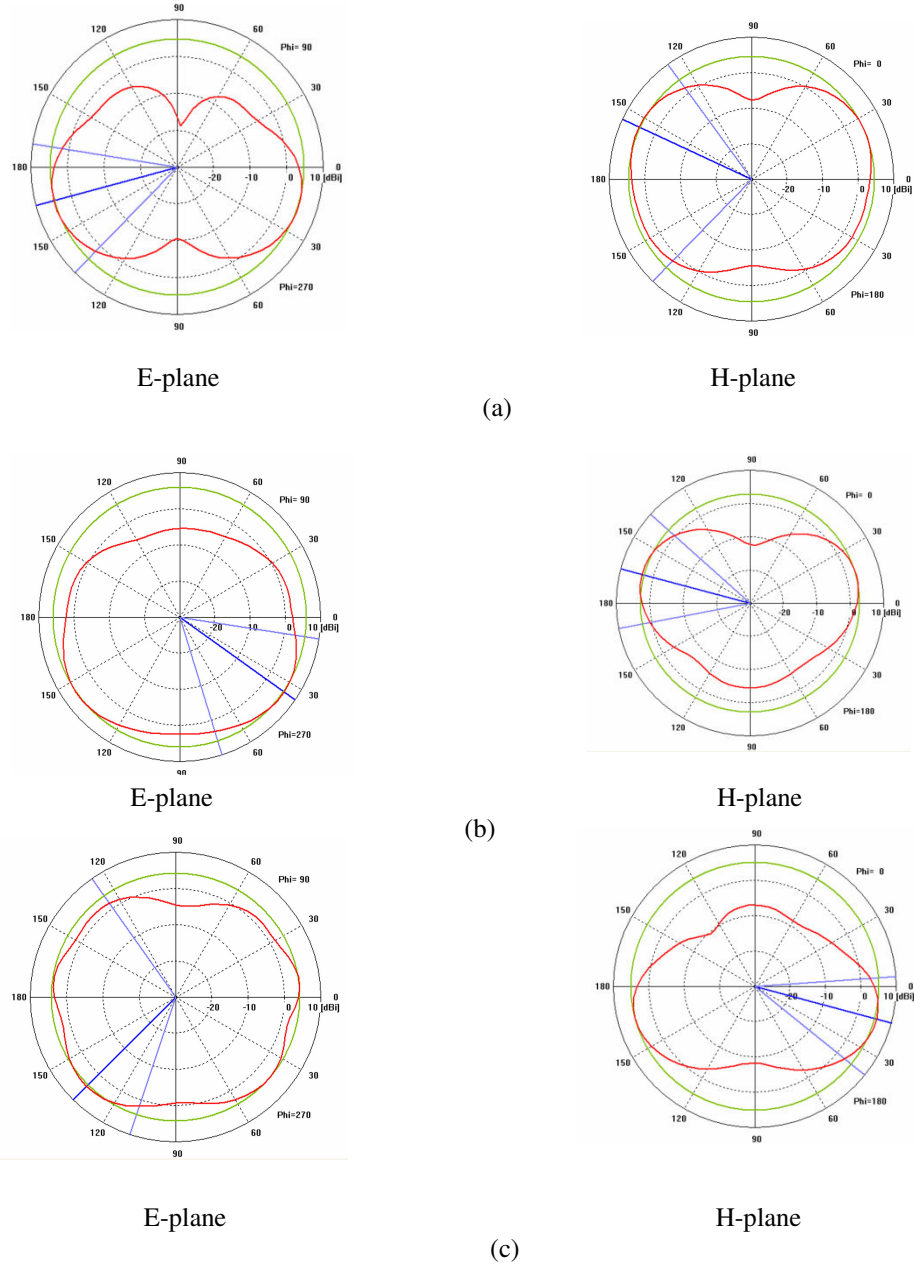


**Fig.4.** Simulated E and H plane patterns of the fractal antenna at (a) 4.5 GHz (b) 6.4GHz, (c) 8 GHz

Fig. 5 shows the simulated gain of the antenna. Two sharp decreases at the vicinity of 3.5 GHz, 5.5 GHz clearly confirm the positive effect of these notched bands in signal-rejection capability.

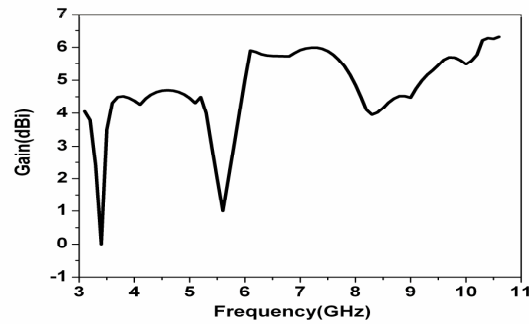


Fig.5. Peak gain is plotted over the UWB band.

UWB antenna system should be distortion free and to ensure this, temporal characterization is desirable. Figure 6 shows the simulated group delay of the antenna systems. The antenna shows a nearly flat response in 3.1 to 10.6 GHz UWB band and the variation of group delay is less than 1ns except in the notched bands, where the group delay makes large excursion. This ensures satisfactory time domain characteristics and distortion free transmission.

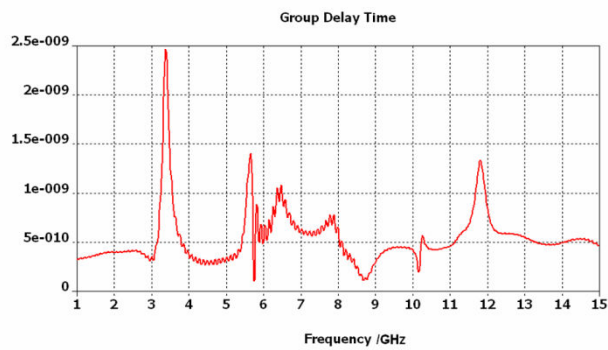


Fig.6.The simulated group delay (sec) of the antenna.

## 4. CONCLUSION

In this paper, a printed microstrip-fed dual band notched UWB fractal antenna has been presented. Size reduction and bandwidth enhancement is achieved using sierpinski carpet fractal concept. To obtain two sharp notched bands, two types of slots, a open-ended quarter-wavelength type and embedded U shape half-wavelength type, are etched in the Ground plane. The antenna shows broad bandwidth, two sharp notched bands, and good Omni-directional radiation patterns throughout the operating band.

## 5. REFERENCES

1. First Report and Order in the matter of Revision of Part 15 of the Commission's Rules Regarding Ultra-Wideband Transmission Systems, Released by Federal Communications Commission, ET-Docket 98-153, 2002.
2. Z. N. Chen, "UWB antennas: from hype, promise to reality," *IEEE Antennas Propag. Conf.*, pp. 19-22, 2007.
3. X. Qu, S. S. Zhong, and W. Wang, "Study of the band-notch function for a UWB circular disc monopole antenna," *Microw. Opt. Technol. Lett.*, vol. 48, no. 8, pp. 1677-1670, 2006.
4. Y. J. Cho, K. H. Kim, D. H. Choi, S. S. Lee, and S. O. Park, "A miniature UWB planar monopole antenna with 5-GHz band-rejection filter and the time-domain characteristics," *IEEE Trans. Antennas Propag.*, vol. 54, no. 5, pp. 1453-1460, May 2006.
5. C. Y. Hong, C. W. Ling, I. Y. Tarn, and S. J. Chung, "Design of a planar ultra wideband antenna with a new band-notch structure," *IEEE Trans. Antennas Propag.*, vol. 55, no. 12, pp. 3391-3397, Dec. 2007.
6. Kenneth Falconer, *Fractal Geometry: Mathematical Foundations and Applications*, 2<sup>nd</sup> edition, New York 2003.
7. C. Puente, J. Romeu, and R. Pous *et al.*, "Small but long Koch fractal monopole," *Electron. Lett.*, vol. 34, no. 1, pp. 9-10, 1998.
8. "On the behavior of the Sierpinski multiband fractal antenna," *IEEE Trans. Antennas Propag.*, vol. 46, no. 4, pp. 517-524, Apr. 1998.

## Fiber Optic Sensor Mechanisms for Biochemical Detection

Ricky Anthony, Sambhunath Biswas

Department of Electronics and Communication,  
Heritage Institute Of Technology, Kolkata 700107,India

**Abstract:** The papers puts light into the key fiber sensor methodologies and types. It gives an account of various researches going on in fiber sensors for chemical and specifically biochemical detection in the last decade, along with analytes specific technologies such as fluorescence surface plasma resonance and ring-down spectroscopy in biosensors. Discussions on the trends in optical fiber biosensor applications in real samples are enumerated.

**Keywords:** FOBS, Evanescent field, Quenching, FRET, SPR, Ring down spectroscopy.

### 1. INTRODUCTION

Fiber optic sensors have an inbuilt advantage when compared to traditional electrical signal based sensors systems as they are insensitive to electrical changes in the nearby environment and are smaller in size and more accurate with lesser noise, especially from the cross talks originating from neighboring fibers as they depend only on the phase, amplitude or wavelength variations of the light rays, which interact with the measurand internally or externally while propagating within the fiber by virtue of total internal reflection (TIR). Moreover these fibers are non-toxic and chemically inert and hence can be inserted in thin hypodermic needles for biomedical use. Even though it is expected that all of the light would undergo total internal reflection, when the cladding diameter is made extremely small, a component of light called the evanescent field propagates through the cladding which can be made to interact with the surroundings through a tapered, etched or side-polished region of the cladding giving a variation of wavelength, phase or amplitude of light. This basic principle is the building block of modern biochemical measurand detection.

A fiber optic sensor as shown in figure1a) can be broadly classified as intrinsic and extrinsic. In case of intrinsic sensors the analyte can directly interact with the fiber and alter the properties of the optical fiber. Extrinsic sensors use fiber cable only as a channel for transmitting light to and from the sensor [1]. Hence intrinsic sensors are more sensitive and generally have lesser loss compared to extrinsic sensing systems.[2,3]. A Fiber optic Biosensor (FOBS) utilizes optical techniques such as absorbance,

fluorescence, chemiluminescence, Surface plasma resonance, refractive index (RI) variation etc. to detect the presence of a chemical molecule and its concentration. The receptors can also be classified as physical, where physical properties such as absorbance, refractive index are exploited and chemical where chemical reactions with the chemical or biochemical analyte modulates the signal.

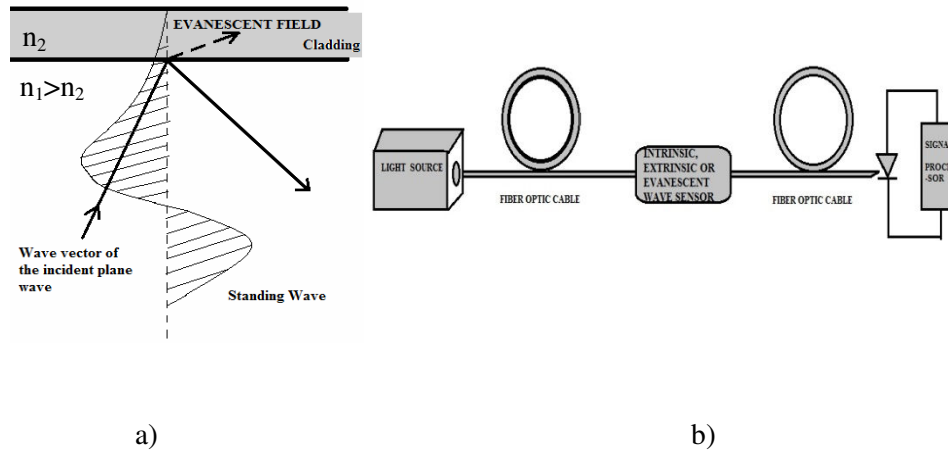


**Fig. 1 a)** Illustration of an exponentially decaying evanescent wave at the cladding region of the fiber.  
**b)** A schematic diagram of a fiber optic sensing system.

## 2. MEASUREMENT TECHNIQUES IN BIOSENSORS

### 2.1 Absorption based Sensor

One of the most basic and simple sensor methods involves the detection of the analyte concentration change by direct absorption of light in a given wavelength. The molecules of the analytes can absorb light (visible and ultra-violet) which causes attenuation. Hence, an increase in attenuation means more absorption of light by the analyte. This absorbance is given by Beers' law:

$$A = \epsilon bc \quad (1)$$

where,  $\epsilon = 2.3 \cdot \epsilon$  is the decadic molar absorption coefficient

$b$  = path length

$c$  = absorbing species

This law is based on Lambert-Bouguer's law with the hypothesis that the gaseous or liquid molecules absorb same amount of light. The table 1 below shows molar absorption coefficient  $\epsilon$  with its corresponding absorption peaks for different chemical compounds.

**Table1. Molar absorption coefficients for different chemical compounds with its corresponding absorption peaks**

Chemical Compounds	$\epsilon$ (liters moles <sup>-1</sup> cm <sup>-1</sup> )	$\lambda$ (nm)	Solvent
Bilirubin	55,000	450.8	Chloroform
Chlorophyll	11,700	417.8	Methanol
Crystal Violet	112,000	509.5	Water
Indocarbocyanine (C3)	133,000	544.25	Methanol
Indotricarbocyanine (C7)	240,000	742.25	Ethanol
Malachite green	148,900	616.5	Water
Nile Blue	76,800	626.75	Methanol

One major example would be pH sensors which are based on red-absorbing colorimetric dyes. Within the biofilms on stainless steel, congo red and neutral red can be immobilized into the cellulose acetate to detect the pH in 3-8.2 range [3, 4]. A similar pH sensor was developed by Wolthuis et al in which pulsed LED from solution is split into long and short wavelength and detected individually by photodiodes to provide a radiometric output. The pH sensor gives an absorption peak of 625nm with the pH range of approximately 6.8-7.8[4]. A linear response by using multiple pH sensors over a broad range was developed by J. Lin and G. Liu which was utilized in sol-gel glass pH sensor by co-entrapping four chemical indicators (bromocresol green, bromicresol purple, phenol red, thymol blue) with a linear characteristic in the range of pH 6.3 to 9.8[5].The absorption bands shown in figure 2.

## 2.2 Fluorescent based Sensor

A fluorescence-based sensor monitors the frequency change of electromagnetic radiation emission stimulated by previous absorption of radiation and subsequent generation of an excited state that only exists for a very short time as shown in figure 3. Since the excitation and emission occur only at distinct energy levels, each fluorescent molecule has a unique fluorescence spectral fingerprint. This technique is of particular importance, since even a weak signal can be efficiently detected, this is because the excitation intensity is directly proportional to the fluorescent intensity. The basis of such measurement lies in Parker's law:

$$I(\lambda_{\text{fluor}}) = KI(\lambda_{\text{excitation}})\psi(\lambda_{\text{excitation}}\lambda_{\text{fluor}})\epsilon(\lambda_{\text{excitation}})Lc \quad (2)$$

where

- $I(\lambda_{\text{excitation}})$ : Intensity of excitation radiation
- $I(\lambda_{\text{fluor}})$  : Intensity of emission radiation
- $L$  : Path length
- $c$  : Concentration
- $\epsilon$  : Absorption Coefficient
- $\psi$  : Quantum yield

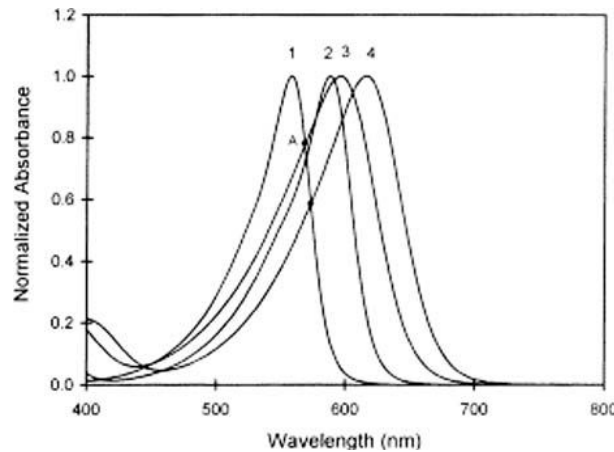


**Fig. 2.** Normalized absorbance with wavelength of four indicators (1 – phenol red, 2 – bromocresol purple, 3 – thymol blue, and 4 – bromocresol green) [5].

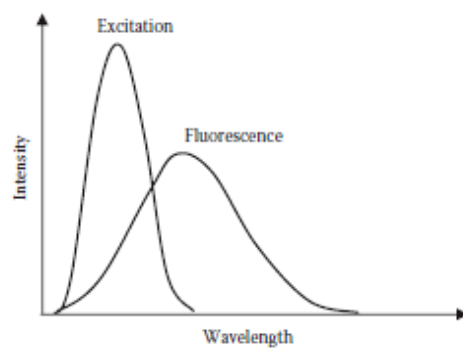


Fig. 3. Excitation and emission (fluorescence) intensity curve

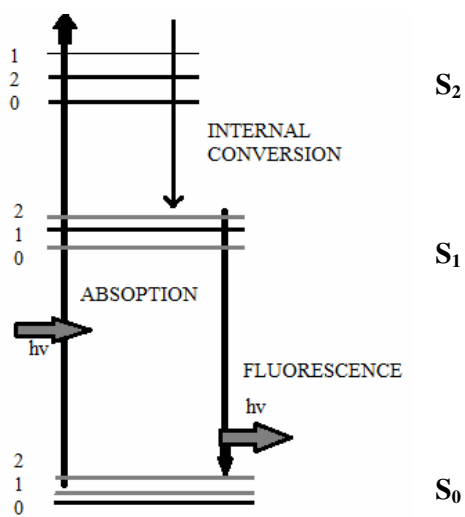


Fig. 4. Jablonski diagram showing Radiative emission

The property of fluorescence in organic molecules was well explained by Jablonski [6]. As shown in figure 4, are the electronic states  $S_0$  (singlet ground state),  $S_1$  and  $S_2$  the excited states. Photons are absorbed at lowest vibration level  $S_1$  and are excited to level  $S_1$  or  $S_2$ . The molecules then rapidly relax to the lowest vibrational level of  $S_1$ , the process known as internal conversion within  $10^{-12}$  seconds. Fluorescence is observed when the molecules settle from  $S_1$  to  $S_0$ , thus reaching thermal equilibrium. The fluorescence lifetime of  $S_1$  is generally in the range of  $10^{-8}$  sec. Due to the energy loss within the excited state, the energy of the emitted photons is lower than the absorption energy. Consequently, the wavelength of the emitted photons is longer than the wavelength of the excitation photons. The difference between the fluorescence wavelength and the absorption wavelength is defined as the Stokes shift. A larger Stokes shift increases the sensitivity of fluorescence measurements as it allows emission photons to be detected against a lower background, better spectrally separated from the excitation photons.

Fluorescence quenching is a process that reduces the intensity of the fluorescence without changing the fluorophore emission spectrum. The fluorescence intensity reduces as it interacts with the quencher or the substance to be detected. This decrease in intensity is given by Stern-Volmer equation:

$$\frac{I_0}{I} = 1 + K [Q] \quad (3)$$

where,

- $I_0$  : Intensity of fluorophore in the absence of quencher
- $I$  : Intensity of fluorophore in the presence of quencher
- $K$ : Sterner-Volmer quenching constant

Fluorescent quenching can be of collision, dynamic and self-quenching types.

**Collision Quenching:** The analyte (quencher) which is to be sensed collides with the fluorophore which results in the decrease in the sensor fluorescence.

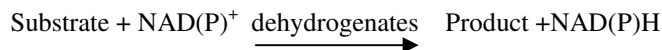
**Self Quenching:** When the concentration of fluorescence dyes or biomolecules is high, fluorophore acts as its own quencher, which occurs due to energy transfer between identical molecules as the Stokes shift is small or by Stern-Volmer process.

Fluorescent based biosensors are of particular importance especially for glucose detection because:

- a) This technique is extremely sensitive and has been able to detect even a single biomolecule. The single molecule can be easily excited and detected repeatedly.[7]
- b) This technique can also provide information about the structure of the molecules and their changes in presence of analytes.
- c) FRET (Fluorescence Resonance Energy Transfer) can be employed for structural analysis of the biomolecules. [8]

Enzyme based reactions rarely produce fluorescent products; hence most cases fluorescent dyes are employed.  $NAD^+$ (nicotinamide adenine dinucleotide) is an example

of enzyme based catalyzed reaction in which NADH or NADPH produced shows fluorescence with  $\lambda_{\text{excitation}}=350\text{nm}$ ,  $\lambda_{\text{fluorescent}}=450\text{nm}$ [9].



FRET( Fluorescence resonance energy transfer) is based on non-radiative excited electronic energy, first proposed by J.Perrin in 1920 which showed that energy can be transferred within close proximities over hundreds or even thousands of angstroms. Forester proposed, in 1946, that FRET can occur at  $100\text{\AA}$  [9]. FRET is a technique in which a fluorescent molecule (fluorophore) non-radioactively transfers energy to a non-fluorescent (static) or fluorescent (dynamic) molecule (acceptor) in close proximity. Due to close distance between the two molecules, they act as dipoles, hence the fluorescence intensity and lifetime of the fluorescent molecule decreases and the rate of energy transfer varies as  $R^6$ , where R is the distance between the centers of the two molecules and it should be in the range of 1-10nm for FRET to occur. This dependency on distance makes FRET a very sensitive technique, with detection even in the order of angstrom. The efficiency of energy transfer is given by Forster theory as:

$$\eta = \frac{R_0^6}{R_0^6 + R^6} \quad (4)$$

Where,  $R_0$  is a constant which depends on the fluorophore/acceptor pair. The acceptor (non-dynamic or static) absorbs the energy which is a function of the analyte to be detected. Hence the variation in intensities can be given by:

$$\frac{I}{I_0} = 1 - \eta \quad (5)$$

If the acceptor is another fluorophore, instead of analyzing intensity variation, it is convenient to analyze the lifetime or time dependent decay of the fluorophore, which decreases with the increases with the increase in quencher concentration.

### 2.3 Surface Plasmon Resonance Based Sensor

The property of surface plasmon resonance (SPR) given by Otto and Kretschmann 1960 is effectively used as a tool for detection and characterization of thin films, gas molecules and biosensors. It is based on the excitation of the evanescent electric field by resonance energy transfer between the evanescent wave and the metal surface plasmon or electron gas. For surface plasmon spectroscopy (SPS), the interface between the core and cladding is coated with a thin layer of metal (e.g. gold); the evanescent field (the exponentially decaying field normal to the boundary surface) transfers its resonant energy to excite the surface plasmons in the metal film. At this interface the resonance takes place when the momentum of the photons in the plane of the metallic layer matches that of the

surface plasmons. The momentum is a function of the metal dielectric  $\epsilon_m(\omega)$  and the dielectric of external layer,  $\epsilon$ , given by:

$$k_{sp} = \frac{\omega}{c} \sqrt{\frac{\epsilon_m(\omega)\epsilon}{\epsilon + \epsilon_m}} \quad (6)$$

**Table 2. Some Fluorescent based Fiber optic biosensors (FOBS)**

APPLICATION	METHODOLOGY
Lactate	Using bacterial cytoplasmic membranes (CPM) as the biological recognition element and an oxygen sensitive dye layer as transducer [10].
Ethanol, Mannintol	Alcohol dehydrogenase + lactate dehydrogenase for ethanol; Mannintol dehydrogenase + lactate dehydrogenase for mannintol [11].
Fructose, glucose	Glucose-fructose-oxidoreductase isolated from <i>Zymomonas mobilis</i> confined in a measurement cell behind an ultrafiltration membrane [12].
Glucose	Biochemical assay based on homogeneous singlet/singlet energy transfer affinity assay [13].
DNA Sensor	Using Lagmuir-Blodgett technique [14].
Proteins	Matrix uses a gold colloid monolayer attached to an end of a fiber as a substrate for protein attachment [15].
Evanescent wave fiber optic biosensor	Combination tapered fibers designed for improved signal acquisition [16].
Evanescent wave biosensor	Fluorescent signal acquisition from step-etched fiber optic probes or from tapered fiber optic probes [17].

If we consider  $\theta$  to be the angle incident on the metallic surface, then the propagation vector parallel to the surface is given by:

$$k_x = \frac{\omega \sqrt{\epsilon_g} \sin \theta}{c} \quad (7)$$

where  $\epsilon_g$  is the dielectric constant of the medium in which the incident light is made to propagate.

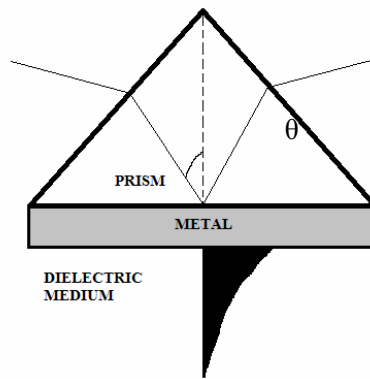


**Fig. 5.** Kretschmann configuration for generation of surface plasma resonance, using prism coupler.

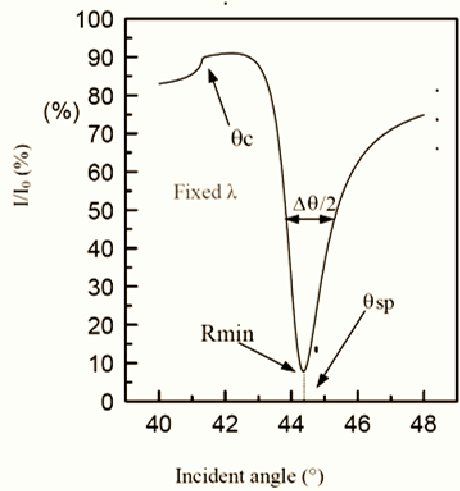


**Fig. 6.** Reflectance curve showing absorption peak due to plasma resonance for thin silver film (50nm) deposited on BK7 prism ( $n=1.514$ ) in air [18].

Kretschmann configuration as shown in figure 5, at a particular angle of  $\theta$  with thin metallic layer,  $k_x = k_{sp}$ , i.e. the evanescent field penetrates the thin metallic layer to couple with the surface plasmon wave. This certain angle at which the reflected angle sharply falls to almost zero value is called the attenuated total reflection (ATR) angle due to resonant coupling of the evanescent waves with the surface plasmons for silver film as shown in figure 6. [18].

SPR based sensors can be implemented to sense both physical and chemical changes. In case of chemical sensing, the change in adsorption of different chemicals with respect to its concentration can be analyzed. SPR has been successfully used to detect chemicals like hydrocarbons, alcohols etc. In biosensors the surface of SPR sensor is prepared with biomolecules with binding capability. The SPR sensor is made to contact the analyte molecules which are to be detected as shown in figure 7. The analyte molecules then adhere and bind to the biomolecule receptors on the surface of the sensor; this increases the refractive index (RI) at the surface. This RI change is dependent on the concentration of the analytes. This leads to a change in the light wave interaction with surface plasma resonance wave.

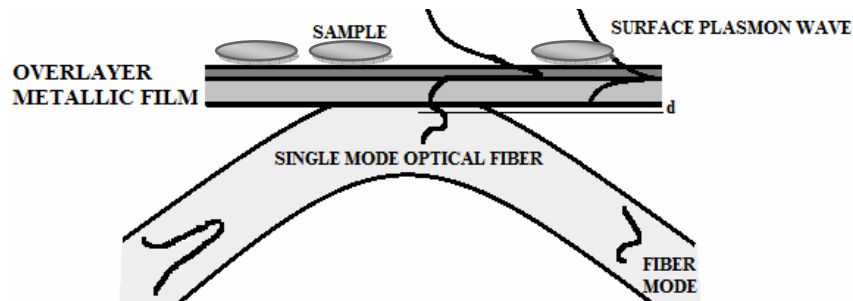


Fig. 7. Generation of SPW at the surface of the metallic film for detection of the sample.

## 2.4 Fiber Cavity Ring Down Spectroscopy (CRDS)

Optical ring resonators are one of the newest sensing technologies used for the detection of analytes both chemical and bio-chemical in gaseous and liquid mediums. It is based on the analyses of the lifetime the photon within the cavity, which is dependent on the optical losses such as scattering and absorption and independent of light intensity. The round trip time of the photon within the cavity is given by:

$$t_{RT} = \frac{nL}{c} \quad (8)$$

where,

- n: effective refractive index of the cavity
- L: cavity length
- c: speed of light in vacuum

The photon life-time  $t$  and transmission per round trip  $t_{RT}$  are related by:

$$t = \frac{t_{RT}}{-\ln(T_{RT})} \quad (9)$$

The technique is based on the measurement of the decay rate which is dependent on the absorbance and scattering losses. The light is made to interact with the sample which results in losses and hence the ring-down times can be determined by the losses. If we consider ' $\alpha$ ' to be the absorption coefficient, then the ring down time is given by:

$$t = \frac{nL}{c(-\ln T_{RT} + \alpha L)} \quad (10)$$

The circulating nature of the resonant mode give along effective interaction length with the analyte compared to traditional fiber sensors. The effective length is given by:

$$L_{effective} = \frac{QL}{2\pi n} \quad (11)$$

where Q is resonator quality factor (Q-factor). Figure 8 shows a surface RI based ring resonator with molecular binding and its sensorgram obtained by monitoring the spectral shift.

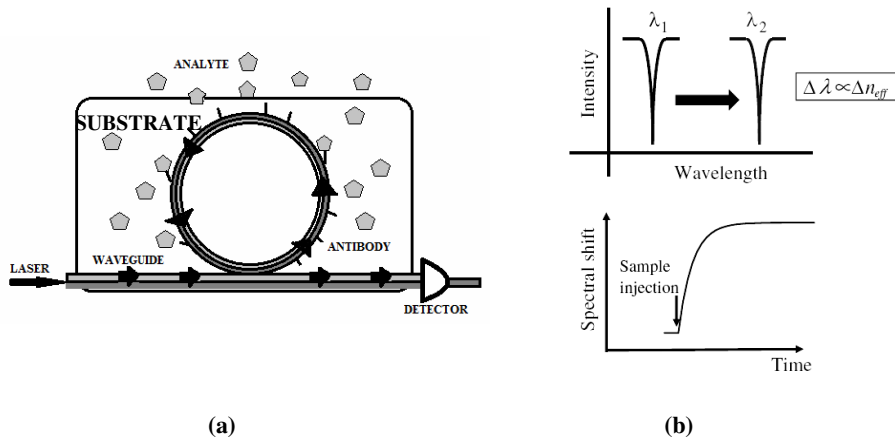


**Fig. 8. a)** A CRDS based biosensor detecting the binding of the analyte. **b)** The wavelength shift due to the RI change induced by the binding and its sensorgram.

CRDS is of particular importance in case of high sensitive sensors due to its long path length, i.e the interaction length with analyte. It has high throughput in order of milliseconds. However it is dependent on analytes which are rare in terms of tunable laser light at a particular wavelength. This technique has been successfully developed in fiber loop ring down (FLRD). The light pulse travels inside the fiber loop for many rounds. At each round only a small fraction of the light pulse couples out of the loop and detected by the photodetector, the rest is are losses. This gives an exponential decay in the detected pulse after each round trip as shown in figure 9. The time between the two successive peaks in the intensity curve is the round trip time [19].

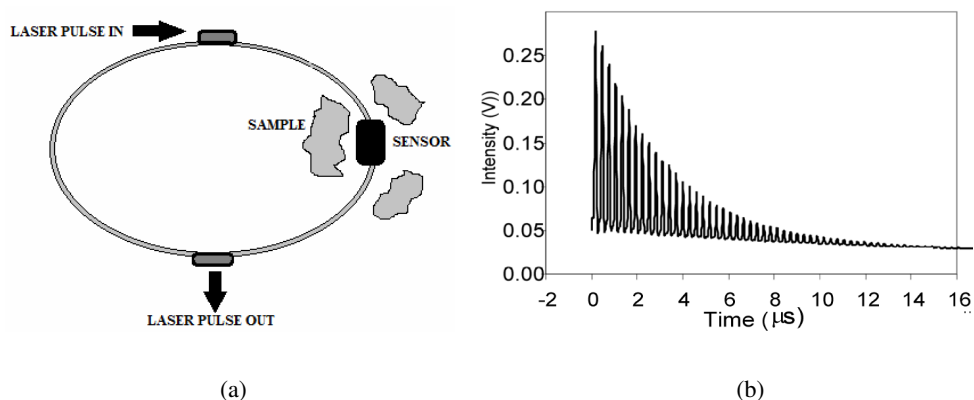


**Fig 9.** (a) The basic fiber loop ring down system. (b) The exponential intensity decay with time, after successive pulses detected by the photodetector. A slower decay rate means lower optical losses of the light in the loop, and vice versa. FLRD measures time to determine a quantity.

### 3. CONCLUSION

Fiber optic sensors in biochemical detection have played a pivotal role in the last few years and will continue to do so because of its miniature size and insensitive nature to electric changes. These fibers can monitor changes in glucose, proteins and biochemical like hemoglobin in patients' blood over a long distance. Recent trends indicate the use of nanosensors and etched (surface, side-polished and tapered) fibers for sensing applications. Hence fiber sensors have and will continue to find applications in biomedical field as well in industrial, chemical and space shuttles for monitoring physical changes like temperature, pressure etc.

#### 4. ACKNOWLEDGEMENT

The authors would like to acknowledge Dr. Tarun Kumar Gangopadhyay (Principal Scientist E-II), Fiber Optics and Photonics Division, Central Glass and Ceramic Research Institute (CSIR) and Prof.(Dr.) Sambhunath Biswas, Principal, Heritage Institute of Technology, Department of Electronics and Communication for their guidance and support.

#### 5. REFERENCES

1. C Righini., Giancarlo,Tajani, Antonella, “*An Introduction to optoelectronic Sensors*”, World Scientific Publishing Co. Pte. Ltd, pp. 5-12 (2009).
2. Davis, A., R., Bush, C., Harvey, J. C. and Foley, M. F., “*Fresnel lenses in rear projection displays*”, SID Int. Symp. Digest Tech. Papers 32(1), pp. 934-937 (2001).
3. Ganesh. A. B, Radhakrishnan, T. K. Sens. Actuators, B: Chem.2007, 123, pp. 1107-1112.
4. Ganesh. A. B, Radhakrishnan, T. K., Fiber Integrated Opt., 2006, 25, pp. 403-409.
5. Baldini.F, Chester. A.N, Homola. J, Martellucci. S; “*Optical Chemical Sensors*”, Springer Publication, pp. 86-87 (2004).
6. Lakowicz, J.R., “*Principles of Fluorescence Spectroscopy*”, Plenum Press, New York, pp. 367-377 (1999).
7. Weiss, S., 1999. Fluorescence spectroscopy of single molecules. Science 283, pp. 1676–1683.
8. Selvin, P.R., 1995. Fluorescence resonance energy transfer. Method. Enzymol 246, pp. 300–334.
9. Forester, Th. Discuss.Faraday Soc.; 1959; 27; pp. 7-17.
10. Iganatov, S.G.; Ferguson, J.A.; Walt, D.R. “A fiber-optic lactate sensor based on bacterial cytoplasmic membranes”, Biosensors and Bioelectronics 2001, 16, pp. 109-113.
11. Sheper, T.; Brandes, W.; Graw, C.; Hundecck, H.G.; Reinhardt, B.; Ruther, F.; Poltz, F.; Shelp, C.; Schugerl, K.; Schneider, K.H.; Giffhorn, F.; Rehr, B.; Sahm, H. “Applications of biosensor systems for bioprocess monitoring”, Analytica Chimica Acta 1991, 249, pp. 25-24.
12. Scheper, T. “A fluorometric fiber-optic biosensor for dual analysis of glucose and fructose using glucose - fructose-oxidoreductase isolated from *Zymomonas mobilis*”. Journal of Biotechnology 1994, pp.36,39-44.
13. Meadows, D. L.; Schultz, J. S. “ Design, manufacture and characterization of an optical fiber glucose affinity sensor based on an homogeneous fluorescence energy transfer assay system.” Analytica Chimica Acta 1993, 280, pp. 21-30.

14. Furch, M.; Ueberfeld, J.; Hartmann, A.; Bock, D.; Seeger, S. "Ultrathin oligonucleotide layers for fluorescence-based DNA sensors". Proceedings of SPIE - The International Society for Optical Engineering 1996, 2928, pp. 220-226.
15. Clark, H. A.; Merritt, G.; Kopelman, R. "Novel optical biosensors using a gold colloid monolayer substrate". Proceedings of SPIE - The International Society for Optical Engineering 2000, 3922, pp. 138-146.
16. Anderson, G. P.; Golden, J. P.; Ligler, F. S. "A fiber optic biosensor: Combination tapered fibers designed for improved signal acquisition". Biosensors and Bioelectronics 1993, 8, pp. 249-256.
17. Anderson, G. P.; Golden, J. P.; Cao, L. K.; Wijesuriya, D.; Shriver-Lake, L. C.; Ligler, F. S. "Development of an evanescent wave fiber optic biosensor". IEEE Engineering in Medicine and Biology Magazine 1994, 13, pp. 358-363.
18. T.Liebermann, Knoll.W, Sluka.P and Herrmann.R, colloids surface A, 169, pp. 337 (2000).
19. Stewart, G.; Atherton, K.; Yu, H.; Culshaw, B. "An investigation of an optical fibre amplifier loop for intra-cavity and ring-down cavity loss measurements" Meas. Sci. Technol. 2001, 12, pp. 843-849.

## Design and realization of solar internal lighting system for homes and office spaces

Kavitha K.G., Upkar Kumar, Retheesh R., A.Mujeeb, P.Radhakrishnan,  
V.P.N.Nampoori.

International School of Photonics,  
Centre of Excellence in Lasers & Optoelectronic Sciences  
Cochin University of Science and Technology, Cochin-22, Kerala, India

**Abstract.** Solar energy is fundamental to the creation and sustenance of life that there is no life without the daily flows of the sun to the earth. Being a clean and inexhaustible source, reliable methods for extraction and usage of solar energy can meet the ever growing demand in the most judicious manner. The present paper reports the design and realization of a solar internal lighting system. The system presented is aimed at reducing the power consumption for internal lighting of homes and office spaces during the sun lit hours. The reported system is realized indigenously at a moderate cost and tested effectively in the laboratory premises for lighting. Full visible spectrum solar light can be focussed using a suitable solar concentrator to a light lead and transported to the desired spots. It is expected that such full spectrum light has advantages of causing reduced eye strain and of increasing work efficiency of the people.

**Keywords:** solar lighting, solar concentrator

### 1. INTRODUCTION

Achromatic retarders are one of the most important components in different scientific and engineering applications. Such retarders can be constructed by several methods. Pancharatnam proposed one of the most successful combinations of three plates fabricated from the same material, showing a reasonably good achromatism over a range of wavelengths [1]. However, in such a system the orientation of the principal axis varies with the wavelength. Achromatic retarders for the visible spectrum using two plates of different birefringent materials having appropriate thickness ratio was suggested by Hariharan [2]. Nicolas Passily *et al* [3] studied achromatic phase retardation based on sub-wavelength dielectric diffraction grating in both the visible and near-infrared regions. Retarders based on total internal reflections were investigated by Korte *et al* [4]. Several studies have been done on thin-film retarders [5] and liquid crystal retarders [6]. A combination of five retarders was suggested to design super-achromatic zero-order wave plates by Samoylov *et al* [7]. Recently an achromatic quarter wave plate has been

designed by Masson *et al* for the terahertz range which consists of six wave plates of varying thicknesses [8].

In the present study, we have proposed the design an achromatic zero-order quarter-wave retarder using plates of crystalline quartz and KDP. These retarder materials have been selected so as to have high optical transmittance in the intended wavelength spectrum. The achromatic system is designed to work in the visible spectrum of 450 nm to 700 nm. The same design can be scaled to obtain a retardation of a half-wave.

## 2. SYSTEM DETAILS

The layout of the developed system is presented in figure (1). The system mainly consists of five components that include a solar concentrator, IR filter or water column, Light lead, sunlight tracker.

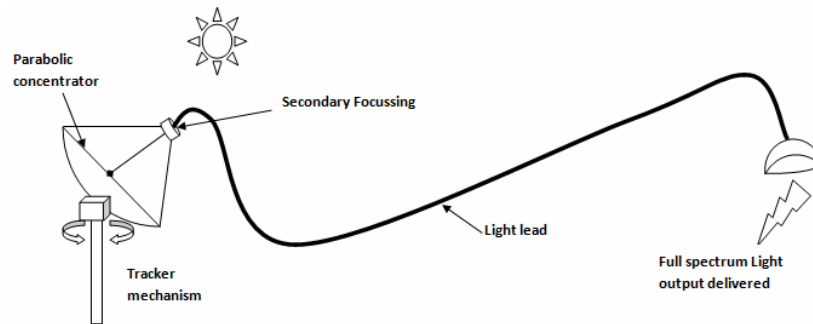


**Fig1.** Layout of the system proposed.

The solar concentrator is basically an arrangement used for collecting the sunlight and focusing it at a point. A parabolic reflector is required for the purpose. The parabolic surface can be approximated using an array of flat surfaces (small plane mirrors) on a parabolic dish provided that the size of each reflector is kept small so that the focussing errors can be neglected. The size of individual mirror needs to be smaller than the target. The main parameters associated with the parabolic reflector are the light gathering capacity of the reflector, the reflectivity of material and its focal length.

The light gathering capacity of the reflector depends on the surface area of the reflector on which light is incident. The area of the paraboloid designed for a radius  $a$  with height  $h$  is given by

$$S = \frac{\pi a [(a^2 + 4h^2)1.5 - a^2]}{4R^2} \quad (1)$$

The focal length of the parabolic reflector depends on the diameter and the depth of the parabolic dish. If 'D' is the diameter of the parabolic surface and 'c' is its depth then the focal length of the parabolic surface is given by

$$f = \frac{D^2}{16c} \quad (2)$$

In the present case, it has been noted that the 'f' value is to be in the range of 25cm to 40cm so that we can effectively collect the light from the focal point. Thus the value of 'D' and 'c' are fixed accordingly. The initial experiments were done by pasting reflective sheets on a parabolic aluminium vessel but the performance was not as per our expectations. Then we tried to achieve better result by pasting mirror pieces on a toy umbrella. The toy umbrella set up is shown in figure (2). Here the light got scattered in different directions instead of converging at a point.

Then the experiment was repeated with small embroidery mirror pieces. These small mirrors were pasted on the parabolic aluminium vessel. The photograph the parabolic aluminium vessel is shown in figure 3. The parabolic aluminium vessel pasted with small mirrors gave satisfactory results since all light are focussed at a required particular point. But as the focal length of the aluminium vessel used was very small, light was getting focused inside the vessel. This was expected due to the larger depth of the vessel as per equation (2).



**Fig.2.** Toy umbrella pasted upon with mirrors



**Fig.3.** Parabolic aluminium vessel pasted upon with smaller mirrors

Thus in order to increase the focal length of the solar concentrator, the experiment was repeated with a parabolic dish having small depth and maximum diameter. The parabolic dish used in this setup was the dish used for providing satellite television in India. This set up with 2000 mirror pieces on the parabolic dish produced good results with a large focal length which is important in order to collect light effectively from the

focus. The set up is shown in the figure (4). Square shaped mirror pieces of average area of the order of  $1\text{cm}^2$  were used.

#### Characterization of the solar concentrator:



**Fig.4.** The arrangements for characterization of solar concentrator

A set up shown in the figure (4) was used to find the temperature at the focus. The aim was to confirm the need to use an IR filter and find the suitable IR filter. Then the temperature rise for the required volume of water kept at the focus was also found.

To check the feasibility of use of reflective pipes for light lead the efficiency of such light leads were calculated. A series of mirrors were used to reflect light through a distance of around 4m to calculate the efficiency. The setup did not produce satisfactory result. The light was then guided through polymer fibres of 0.5mm drawn in our laboratory and we achieved a very high efficiency of light transmission.

### 3. RESULTS AND DISCUSSIONS

The focal length of the parabolic dish thus designed was found to be 35cm. The temperature at the focus was found to be raised to  $130^{\circ}\text{C}$  in a time span of 1 minute and 40 seconds. This high temperature implied that a proper IR filtering would be needed for the process before the light is concentrated on to the light lead. The temperature rise of water kept at the focus was found to increase to about  $60^{\circ}\text{C}$  over a period of half an hour during the peak hours of the day (11 am -2:00PM). This also led us to draw the inference that a water column could be used as the IR filter before focussing the light into the bundle of optical fibres.

The efficiency of light coming from the receiving end of the polymer fibres was found to be nearly 100% which was only 85% in the case of reflecting mirrors. This was the reason behind the use of polymer fibres in the present setup.

#### 4. CONCLUSIONS

A solar internal lighting system has been designed using easily available material of reasonably lower cost. The solar concentrator designed with about 2000 numbers of (1cmx1cm) dimension mirrors gave rise to considerably large losses due to reflection and scattering occurring at the edges of such huge number of mirrors. Thus a solar concentrator with a larger diameter and less number of mirrors without compromising the parabolic shape of the concentrator would give a better concentration of light intensity at the focus. A secondary focussing mechanism can also be used for efficient focussing and coupling of the light focussed by the parabolic concentrator into the fibre bundle. The polymer optic fibre bundle used in the system also contributes to losses due to its limited core diameter in addition to the inherent losses.

#### 5. REFERENCES

1. Khan, N., Mariun, Z., Saleem, N., Abas, N. "Fossil Fuels, New Energy Sources and the Great Energy Crisis". *Renewable and Sustainable Energy Rev* (2007), doi:10.1016/j.rser.2007.11.011.
2. Joseph B. Murdoch, *Illumination Engineering*, McMillan, 1985.
3. David Jenkins and Tariq Muneer, *Modelling light-pipe performances—a natural daylighting solution*, *Building and Environment*, Volume 38, Issue 7, July 2003, Pages 965-972
4. J. D. Muhs, "Design and Analysis of Hybrid Solar Lighting and Full-Spectrum Solar Energy Systems", *Solar 2000, July 16-21, 2000*, American Solar Energy Society.
5. D. Dye, B. D. Wood, L. Fraas, and J. Muhs, *Optical Design of an Infrared Non - Imaging Device for a Full-Spectrum Solar Energy System*, *J. Solar Energy Eng.* 126 (1),pp. 676–679, 2004.

## Low Temperature DC conductivity of Graphite Kaolinite composite

R.Goswami<sup>1</sup>, S.C.Chakravartty<sup>1</sup>, E.Bose<sup>1</sup>, U.Mukherjee<sup>1</sup>, P.Saha<sup>1</sup>, P.Mondal<sup>2</sup>

<sup>1</sup> Department of Engineering Physics  
B.P.Poddar Institute of Management and Technology  
137, V.I.P. Road, Kolkata-700052

<sup>2</sup> Saha Institute of Nuclear Physics,  
1/AF, Bidhan Nagar, Kolkata-700064

**Abstract.** The d.c conductivity of graphite clay composite within the temperature range  $77 \leq T \leq 300$  K has been measured for various concentrations of graphite in clay. Attempt has been made to interpret the d.c. conductivity in terms of variable range hopping theory. The high value of  $\gamma > 0.5$  and high value of  $\sigma_{dc}$  suggest that the electronic transport property is different from standard VRH model.

**Keywords:** graphite, clay, d.c. conductivity, VRH.

### 1. INTRODUCTION

The study of the transport properties of the composite having conducting filler in insulating host has been initiated by various workers due to its manifold applications in optoelectronics and microelectronics, its versatile utility as microwave absorbers and reflectors in both civil and military applications, as solid state devices such as solar cells and Schottky junctions and as EMI shielding material [1,2,3]. The study of the conducting filler graphite in insulating polymer host has been studied in recent years to meet the increased demand of microwave absorbing material for EMI shielding and stealth technology. Such studies however have not yielded conclusive result and the research is still underway. On the other hand the study of the conducting filler graphite in the insulating inorganic host has been more promising because of the easier and cheaper mechanism of the incorporation of the conducting filler in the host. The composite of graphite in clay (kaolinite) was therefore prepared and the study of the d.c. conductivity was initiated to get an insight into the transport property of the composite. Since kaolinite is a natural semiconductor and graphite has good conductivity, a composite of graphite with kaolinite would provide a easy regulation of the transport and thereby the semiconducting characteristics of the composite. The d.c. conductivity within the temperature range  $77 \leq T \leq 300$  K was initiated to study the characteristic mode of

transport within the composite. The charge transport mechanism has been investigated and explained by variable range hopping mechanism. The parameters extracted from the calculation have been discussed by focusing on the possible transport phenomena of the composite.

## 2. EXPERIMENT

The clay matrix used was commercial grade ball clay having dielectric constant in the range between 2 to 4 and were obtained from Central Glass and Ceramic Research Institute of CSIR and graphite was obtained from Graphite India Limited, India. Graphite had the density  $1750\text{kg/m}^3$ , modulus of elasticity (Young's modulus) 4.8 GPa, electrical resistivity  $7.5 \times 10^{-5} \Omega\text{-m}$ , melting point of about  $3600^0\text{K}$  with average particle size between 10-20  $\mu\text{m}$ .

0.01kg clay powder in the kaolinite was sieved through a 300mesh and mixed with different proportions of graphite powder of the same size. Four batches of the samples were prepared with 40, 50, 60 and 63 wt. % of graphite. The samples were then subjected to ball milling in air for ten hours using a high energy planetary ball mill. The ball-powder mass ratio (B.P.M.R) was kept at 10:1. After milling, the powder was pressed into small rectangular samples of dimension  $3\text{mm} \times 2.5\text{mm} \times 1.0 \text{mm}$  by applying a pressure of  $300 \text{kg/m}^2$  and heated to  $1100^0\text{C}$  for two hours in a reducing atmosphere. The sample was then cooled slowly to room temperature and kept in a desiccator to avoid atmospheric and humidity effects and change in the conductivity. Four probes were connected to the sample using conducting silver paint and copper electrodes were attached to it.

The temperature dependent dc conductivity was measured by the standard four-probe method using a Keithley multimeter. Liquid nitrogen cryostat was used to study the temperature dependent resistivity by the Lake Shore 340 Temperature Controller. Temperature was varied from 300K to 77K.

## 3. RESULT AND DISCUSSIONS

We have measured the dc conductivity ( $\sigma_{dc}$ ) of graphite clay composite having 40, 50, 60 and 63% graphite in clay. It is observed in Fig.1 that the d.c conductivity increases with temperature for 40%, 50%, 60% and 63% graphite in clay. Hence, within the temperature range of  $77 \leq T \leq 300 \text{K}$  all the composites show a semiconducting trend. It is observed in Fig.1 that the conductivity of the composite increases with the wt% increase of graphite in clay. Usually in disordered semiconductor the temperature dependence of dc conductivity  $\sigma_{dc}$  is described by the variable range hopping model (VRH),

$$\sigma_{dc}(T) = \sigma_0 \exp\left(-\frac{T_0}{T}\right)$$

Where  $\sigma_0$  is the conductivity as  $T \rightarrow \infty$  and  $T_0$  is the characteristic temperature which is related to the electronic structure and energy distribution of the localized state and  $\gamma$  is the VRH exponent depending on the dimension of the system. The value of  $\gamma$  is 1/4 for three dimension, 1/3 for two dimension and 1/2 for one dimension, respectively. Least square fitting has been done and the values of  $\sigma_0$ ,  $\gamma$  and  $T_0$  has been extracted. The obtained values of the parameters are shown in Table 1. The VRH exponent  $\gamma$  is observed to decrease systematically from 1.0 to 0.66 with increasing wt % of graphite in clay. This has also been observed in other studies [4]. The higher values of conductivity and the exponent  $\gamma$  indicate that the transport properties are different from standard VRH model. The higher values indicate superlocalization of electronic states formed by the metallic islands of graphite in clay host [5]. The superlocalization exponent  $\xi$  given by  $\xi = \frac{\gamma}{1-\gamma}$  has value greater than 1 for all concentrations of graphite in clay. This is an indication of conduction taking place by hopping within the superlocalized states.

#### 4. CONCLUSION

The d.c conductivity of graphite in clay host has been measured within the temperature range of  $77 \leq T \leq 300$  K. The conductivity increased with the increase of temperature indicating a semiconducting characteristic of the composite. The temperature dependence of the conductivity was fitted to the VRH model and the extracted parameters indicated superlocalization of the electronic state within the composite.

**Table-1 Different physical parameters of graphite-clay composite.**

Parameters	40% graphite	50% graphite	60% graphite	63% graphite
$\sigma_1$ (300K) $\Omega^{-1}\text{cm}^{-1}$	$9.22 \times 10^{-5}$	$5.32 \times 10^{-3}$	$1.0 \times 10^{-2}$	$1.35 \times 10^{-1}$
$\gamma$	1.02	0.82	0.83	0.66
$T_0$	870.9	761.06	758.22	881.32
$\sigma_0$ ( $\Omega^{-1}\text{cm}^{-1}$ )	$6.488 \times 10^{-5}$	$3.31 \times 10^{-3}$	$6.36 \times 10^{-3}$	$8.30 \times 10^{-2}$

#### 5.

## ACKNOWLEDGEMENT

One of the authors (R.G.) wishes to thank Prof. B. G. Ghosh for his kind permission to work at S.I.N.P. She would also like to acknowledge the Management of the B. P. Poddar Institute of Management and Technology for their kind support.

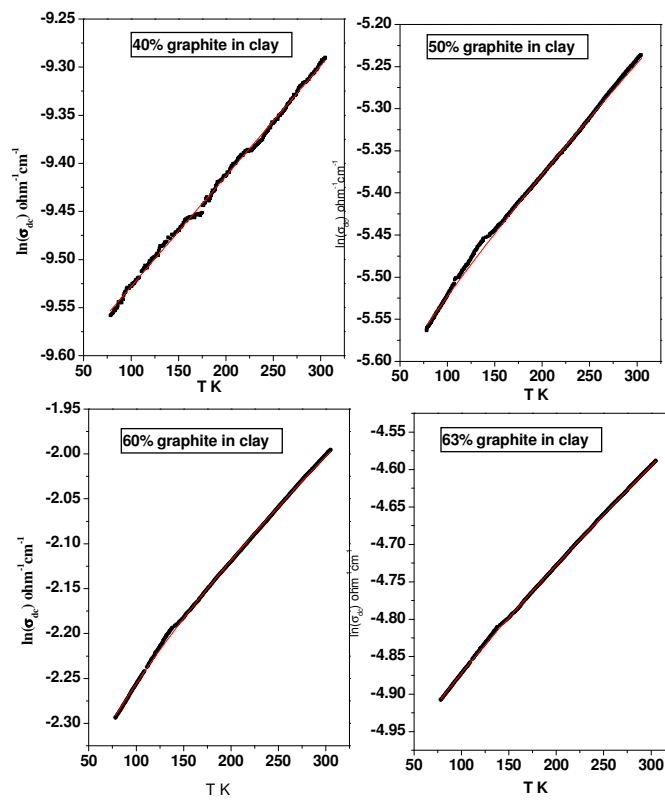


**Fig.1.** Variation of conductivity with temperature for different concentrations of graphite in clay. The black dots are experimental points and the red line is the theoretical fit.

## 6. REFERENCES

1. A.G. Mac Diarmid, *Conjugated Polymers and Related Materials*, W.R.Salaneck, L.Lundstrom, B.Ranby, Eds. Oxford University , London, 1993.
2. H.Naarmann In *Science and Application of Conducting Polymers*, W.R.Salaneck, D.I.Clark, E.J. Samuelsen, Eds: Adam Hilger, Bristol, p81,1991.
3. D.A.Seanor, *Electronic properties of Polymers*,D.A. Seanor Ed.: Academic:New York, p1,1992.
4. P.Dutta, S.Biswas, M.Ghosh S.K.De and S.Chatterjee, *Synth.Met.* 122, 455 (2001).
5. P.Ghosh *et. al*, *Jour. App.Phys.*97,1,(2005).

## A Zero-Order Achromatic Quarter-Wave Retarder

<sup>1</sup>Arijit Saha (Member SPIE),  
<sup>2</sup>Kallol Bhattacharya (Member SPIE), <sup>2</sup>Ajoy Kumar Chakraborty

<sup>1</sup>Department of Electronics & Communication Engineering,  
B. P. Poddar Institute of Management & Technology,  
137, VIP Road, Kolkata-700052, India  
Telefax: +91-33-25739401, email: arijit\_sh@yahoo.com

<sup>2</sup>Department of Applied Optics and Photonics, Calcutta University  
92, A.P.C. Road, Kolkata-700 009, India.  
Telefax: +91-33-23522411, email: kbaphy@caluniv.ac.in, akc\_000@rediffmail.com

**Abstract.** Phase retarders normally exhibit strong wavelength dependence. Such retarders cannot be used in experimental situation where polychromatic light is used. The present investigation relates to a technique to design and study the characteristics of an achromatic combination of birefringent plates for 450 nm to 700 nm range. A composite half-wave retarder has been designed using crystalline quartz and KDP. The thicknesses of the plates are calculated to be 183.90  $\mu\text{m}$  and 37.28  $\mu\text{m}$  respectively. The new arrangement of two birefringent plates proposed has the promise of producing a zero-order quarter wave achromatic combination with fairly good accuracy.

**Keywords:** Birefringent plate, Achromatic retarder, Quarter wave plate

### 1. INTRODUCTION

Achromatic retarders are one of the most important components in different scientific and engineering applications. Such retarders can be constructed by several methods. Pancharatnam proposed one of the most successful combinations of three plates fabricated from the same material, showing a reasonably good achromatism over a range of wavelengths [1]. However, in such a system the orientation of the principal axis varies with the wavelength. Achromatic retarders for the visible spectrum using two plates of different birefringent materials having appropriate thickness ratio was suggested by Hariharan [2]. Nicolas Passily *et al* [3] studied achromatic phase retardation based on sub-wavelength dielectric diffraction grating in both the visible and near-infrared regions. Retarders based on total internal reflections were investigated by Korte *et al* [4]. Several studies have been done on thin-film retarders [5] and liquid crystal retarders [6]. A

combination of five retarders was suggested to design super-achromatic zero-order wave plates by Samoylov *et al* [7]. Recently an achromatic quarter wave plate has been designed by Masson *et al* for the terahertz range which consists of six wave plates of varying thicknesses [8].

In the present study, we have proposed the design an achromatic zero-order quarter-wave retarder using plates of crystalline quartz and KDP. These retarder materials have been selected so as to have high optical transmittance in the intended wavelength spectrum. The achromatic system is designed to work in the visible spectrum of 450 nm to 700 nm. The same design can be scaled to obtain a retardation of a half-wave.

## 2. THEORY

Consider two birefringent plates of thicknesses  $d_1$  and  $d_2$  with their optical axes parallel so that the total phase retardation introduced by them is  $\pi/2$ . Let the two selected design wavelengths be  $\lambda_a$  and  $\lambda_b$ . If the values of the birefringence of the two materials be  $\Delta n_{1a}$ ,  $\Delta n_{2a}$  at  $\lambda_a$  and  $\Delta n_{1b}$ ,  $\Delta n_{2b}$ , at  $\lambda_b$ , the retardation of the system will be equal to quarter a wave at these two design wavelengths when

$$\left| \begin{array}{cc} \Delta n_{1a} & \Delta n_{2a} \\ \Delta n_{1b} & \Delta n_{2b} \end{array} \right| \left| \begin{array}{c} d_{1q} \\ d_{2q} \end{array} \right| = \pm \frac{1}{4} \left| \begin{array}{c} \lambda_a \\ \lambda_b \end{array} \right| \quad (1)$$

The overall phase difference between two orthogonal directions of light may be either  $+\pi/2$  or  $-\pi/2$ , which signifies that if the input is a linearly polarized light at  $45^\circ$  then the output light will be either left or right circularly polarized. Hence in equation (1), either the positive or negative values of retardation may be considered. Here the positive values are considered. For normal materials whose birefringence decreases with wavelength, a solution of the equations mentioned above is possible only by using a combination of both positive and negative birefringence [9]. This requirement may be satisfied with a combination of crystalline quartz (positive) and KDP (negative).

## 3. COMPUTATION OF THE THICKNESSES

The values of birefringence for crystalline quartz and KDP for the wavelength range of 450 nm to 700 nm are presented in table 1 [10]. We have considered  $\lambda_a = 450$  nm and  $\lambda_b = 700$  nm. Setting these values in equation (1) we have the relations

$$\begin{vmatrix} 0.00937 & -0.0432 \\ 0.00898 & -0.0396 \end{vmatrix} \begin{vmatrix} d_{1q} \\ d_{2q} \end{vmatrix} = \frac{1}{4} \begin{vmatrix} 450 \\ 700 \end{vmatrix} \quad (2)$$

These equations may be solved to obtain

$$d_1 = 183.90 \mu\text{m} \quad (\text{Crystalline Quartz}) \quad (3)$$

$$d_2 = 37.28 \mu\text{m} \quad (\text{KDP}) \quad (4)$$

The variation of birefringence of crystalline Quartz and KDP are plotted in figures 1 and 2 respectively. The retardation of the combination is plotted in figure 3. Also the percentage deviation of the overall retardation from the intended quarter wave retardation is shown in figure 4.

**Table 1. Values of birefringence**

Wavelength (nm)	Birefringence ( $n_e - n_o$ )	
	Crystalline Quartz	KDP
450	0.00937	-0.0432
500	0.00925	-0.0424
550	0.00917	-0.0417
600	0.00909	-0.0410
650	0.00903	-0.0403
700	0.00898	-0.0396

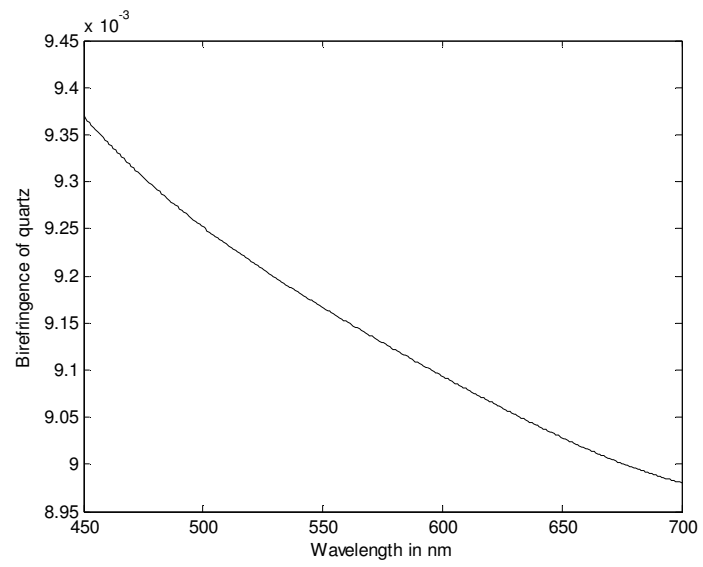


**Fig. 1.** Variation of birefringence of  $\text{MgF}_2$  with wavelength.

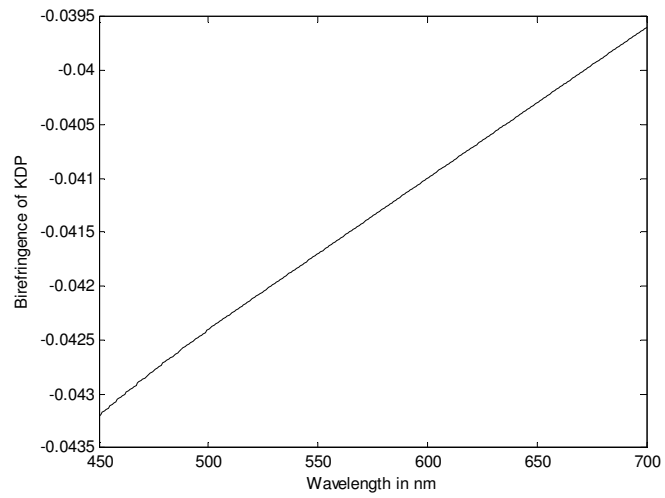


**Fig. 2.** Variation of birefringence of KDP with wavelength.

#### 4. DISCUSSIONS AND CONCLUSION

A simple technique using birefringent plates of two different materials has been employed to design and characterize a system which works as an achromatic quarter wave plate. The combined system designed exhibits a reasonably good achromatic behaviour over the visible spectrum ranging from 450 nm to 700 nm. Computation of the values of overall retardation of the composite plate proposed at different wavelengths within entire visible range show that the variation of retardance is maximum  $-4.5\%$  within the entire visible range as seen in figure 4.

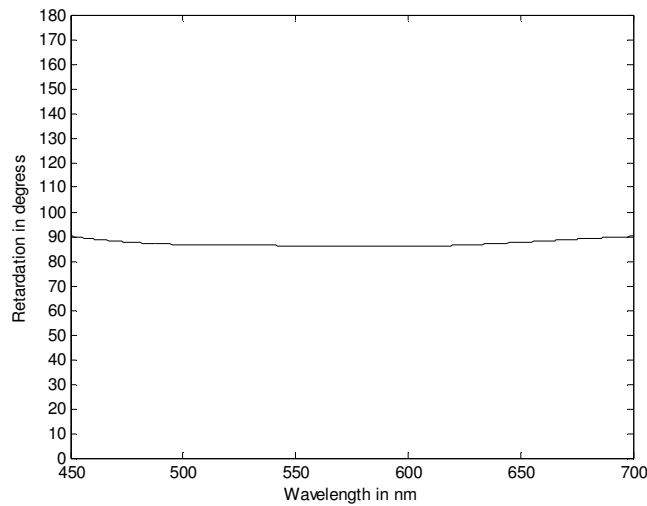


**Fig. 3.** Variation of retardation with wavelength for a combination of a crystalline quartz plate and KDP plate behaving as achromatic quarter wave plate.

Of the two different materials considered in the construction of the proposed filter, KDP is known to be hygroscopic at  $0^{\circ}\text{C}$ , whereas the other material  $\text{MgF}_2$  has very low hygroscopic susceptibility. However, at temperature higher than  $40^{\circ}\text{C}$  KDP does not retain its hygroscopic property. It is therefore convenient to maintain the temperature of the assembly at  $40^{\circ}\text{C}$  or higher. It is also observed that since the thickness of the materials to be used are calculated to be in the micrometer range, it is expected that overall spectral transmission characteristics of the assembly will not vary appreciably.

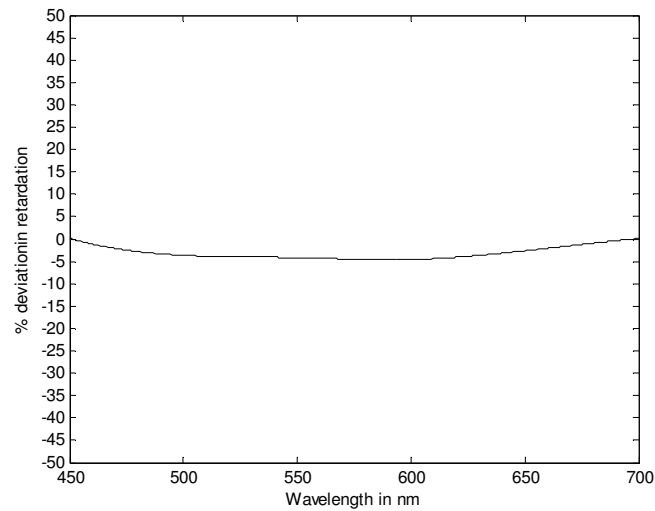


**Fig. 4.** Percentage deviation of quarter wave retardation with wavelength for the combination.

Obviously an achromatic half-wave plate may be constructed using plates of the same materials with double thicknesses. This will create a zero-order half-wave plate. Preliminary computations reveal that increase in the number of plates will lead to better achromatic behaviour.

## 5. REFERENCES

1. S. Pancharatnam, "Achromatic Combinations of Birefringent Plates, Part II. An Achromatic Quarter-Wave Plate", Proceedings of the Indian Academy of Sciences, Vol. XLI, No. 4, Sec A, pp. 137-144 (1955).
2. P. Hariharan, "Achromatic retarders using quartz and mica", Measurement Science and Technology, Vol. 6, No.7, pp. 1078-1079 (1995).
3. Nicolas Passilly, Kalle Ventola, Petri Karvinen, Jari Turunen and Jani Tervo, "Achromatic phase retardation by subwavelength gratings in total internal reflection", Journal of Optics A: Pure Applied Optics, Vol. 10, No.1, 015001(6 pp) (2008).
4. E.H Korte, B. Jordanov, D. Kolev, D. Tsankov, "Total Reflection Prisms as Achromatic IR Retarders", Applied Spectroscopy, Vol. 42, Issue 8, pp. 1327-1577 (1988).

5. Ian Hodgkinson and Qi hong Wu, "Thin-film angle-tuned retarders: theory and fabrication", *JOSA A*, Vol. 18, Issue 4, pp. 975-979 (2001).
6. Hubert Seiberle, Thomas Bachelors, Carsten Benecke and Mohammed Ibn-Elhaj, "*Volume Photo-Aligned Retarders*", *IEICE Transactions*, Vol. E90-C, No. 11, pp. 2088-2093 (2007).
7. A.V.Samoylov and V.S.Samoylov, "*Achromatic and Super-achromatic Zero-order Waveplates*", *Proceedings of LFNM 2003*, IEEE, pp. 119-121 (2003).
8. Jean-Baptiste Masson and Guilhem Gallot, "*Terahertz achromatic quarter-wave plate*", *Optics Letters*, Vol. 31, No. 2, pp. 265-267 (2006).
9. D Clarke, "*Achromatic halfwave plates and linear Polarization rotators*", *Optica Acta*. Vol. 14, No.4, pp. 343-350 (1967).
10. J M Bennet, "*Polarizers*", *Handbook of Optics*, Chapter 3, Vol. 2 edited by M Bass, pp. 3.46-3.49 (McGraw-Hill, New York, 1995).

# Texture Matching of Gray Level Images Using Legendre Moment Technique

Ivy Majumdar<sup>1</sup>, Suvankar Das<sup>1</sup>, Avirup<sup>1</sup>, Avijit Kar<sup>2</sup>, B.N.Chatterji<sup>1</sup>

<sup>1</sup>Department of Electronics & Communication Engineering,  
B P Poddar Institute of Management & Technology,  
137, VIP Road, Kolkata, Pin 700052, India

<sup>2</sup>Department of Computer Science & Engineering,  
Jadavpur University, Kolkata

**Abstract:** Content Based Image Retrieval (CBIR) system applying invariant image moments, viz., Zernike Moment, Moment Invariants (MI) are available. But they show poor reconstruction and non-orthogonality. So there is a need for an efficient and orthogonal moment based CBIR system. Being orthogonal and computationally faster Legendre moment (LM) is suitable for this. In this paper a novel method is proposed for the retrieval of the gray scale texture images from a database after feature matching using exact Legendre moment (ELM). It is a fast algorithm and the obtained results show the superiority of this method over the other methods both on accuracy as well as speed.

**Keywords:** LM, Gray level Images, Feature Matching, CBIR

## 1. INTRODUCTION

With the development of World Wide Web (www) a large amount of research work has been found for image data base searching. Content Based Image Retrieval (CBIR) is widely used for searching image data base. It finds its application in internet, medical image archives, crime prevention etc.

Over the years a lot of moment functions have been used in the field of Image processing and various algorithms were developed for Image recognition and information retrieval from a database after the works of Hu [1]. With orthogonal moments (e.g. Legendre moment (LM) and Zernike moment) problem of information redundancy [2] in representation of an image can be minimised. Many algorithms [3, 4, 5] are suggested for LM calculation. The two most important factors while using moments for CBIR are speed and accuracy. None of the methods could improve both the factors simultaneously and improve the efficiency of the method as many approximations were imposed on the calculations.

In this work we have used a sophisticated method, known as exact Legendre moment (ELM) technique by which we could improve both speed and accuracy of the computation for CBIR.

This paper is organised as follows. In Section 2 an overview of the Legendre moment is given along with the used formulae. The proposed method is illustrated in Section 3. In Section 4 some experimental results have been discussed. Concluding remarks are given in Section 5.

## 2. LEGENDRE MOMENT

LM are continuous and orthogonal moments; these are generally used to represent an image with minimum amount of information redundancy. Many algorithms are developed for the computation of LM [3, 4, 5], but these methods mainly deal with 2D geometric moments. While applying these to a digital image, a numerical approximation is necessary. Error due to approximation increases with the order of the moment. An accurate method for computing the exact Legendre moments given by Hosney [6] is as follows.

Legendre moments of order  $(p + q)$  for an image with intensity function  $f(x, y)$  are defined as

$$L_{pq} = \frac{1}{4} \int_{-1}^1 \int_{-1}^1 P_p(x) P_q(y) f(x, y) dx dy \quad (1)$$

where,  $P_p(x)$  is the  $p$ th order Legendre polynomial defined as

$$P_p(x) = \sum_{k=0}^p a_{k,p} x^k = \frac{1}{2^p p!} \left[ \frac{d}{dx} \right]^p [(x^2 - 1)^p] \quad (2)$$

where  $x \in [-1, 1]$ , and the Legendre polynomial  $P_p(x)$  obeys the following recursive relation: -

$$P_{p+1}(x) = [(2p+1)x / (p+1)] P_p(x) - [p / (p+1)] P_{p-1}(x) \quad (3)$$

With  $P_0(x) = 1$ ,  $P_1(x) = x$  and  $p > 1$ .

A Digital Image of size  $M \times N$  is nothing but an array of pixels. Centre of these pixels are the points  $(x_i, y_j)$ , where the image intensity function is described for discrete set of points  $(x_i, y_j)$ .

$$\Delta X = 2/M$$

$$\Delta Y = 2/N$$

$$X_i = -1 + (i-1/2)\Delta X$$

$$Y_j = -1 + (j-1/2)\Delta Y$$

With  $i = 1, 2, 3, \dots, M$  and  $j = 1, 2, 3, \dots, N$  for discrete space version of the images Eq. (1) is generally approximated by

$$L_{pq} = ((2p+1)(2q+1)/MN) * \sum_{i=1}^M \sum_{j=1}^N P_p(x_i) P_q(y_j) f(x_i, y_j) \quad (4)$$

Eq. (4) is the direct method of Legendre moment calculations.

Now a day's LM is used for different purpose in image processing viz. pattern recognition [7], face recognition [8], object classification [9], template matching [10] etc. We have used this ELM for texture matching and image retrieval.

### 3. THE PROPOSED METHOD

Fast and accurate CBIR algorithms are needed for practical applications. Here we have used quantisation to improve the speed and accuracy. The basic algorithm of the method is as follows:

**Step 1:** Exact Legendre moments for the database images are computed.

**Step 2:** Intensity levels of the images are quantized

**Step 3:** Feature database is generated by feature vector  $f_{\text{database}} = (f_1, f_2, \dots, f_N)$  for the image database consisting of  $N$  images. Each feature vector  $f_i$ , for  $i = 1, 2, \dots, N$ , is a set of ELM of order  $(p + q) = g$

**Step 4:** The name of the query image is used as input.

**Step 5:** Then the users are asked to select the starting position from where they want to extract the intensity information from the query image. This method is called Window Extraction.

**Step 6:** After quantisation of the intensity level of query image a feature vector  $f_q$  of ELM of order  $(p + q) = g$  for the query image is prepared.

**Step 7:** Distance between the query image feature vector  $f_q$  and each feature vector of the database images  $f_i$  is calculated by using Manhattan distance  $D_1$

$$D_1 = \sum_{i=1}^N |f_q - f_i| \quad (5)$$

**Step 8:** based on minimum distance  $D_1$  all the images are retrieved.

### 4. EXPERIMENTAL RESULT

#### 4.1. THE DATABASE

Texture database used is taken from Brodatz album [11] (1966) and Freefoto [12]. Total 111 images each of size 643 X 643 starting from D1- D112 except D14 ( not available in net ) was taken from Brodatz album and 9 images were taken from freefoto. Each 643 X 643 image was divided into sixteen nonoverlapping 160 X 160 sub-images. So the database consists of total 1920 images. A query image is any one of these 1920 database images. For every query image  $q$  there are 16 ground truth images  $S_q$ . Retrieval rate  $RR_q$  for each image is given as

$$RR_q = \frac{\| S'_q \|}{\| S_q \|} \quad (6)$$

where  $S'_q$  is the set of images retrieved from  $S_q$  and  $\| \cdot \|$  shows the cardinality of the set. For the whole database average retrieval rate is given by

$$\text{Average Retrieval Rate} = \frac{\sum_{q=1}^N RR_q}{N} \quad (7)$$

Here  $N$  is the number of query images.

In Fig.1 eighteen images from our database are shown.

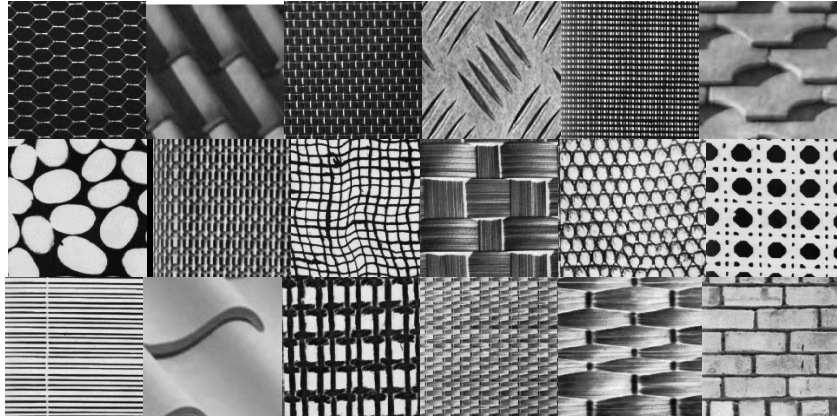


Fig.1. Eighteen images from database

#### 4.2 RESULT

The Accuracy of the ELM method was compared with two existing methods, viz., normalised cross-correlation (NCC) and Canberra Distance Metric (CDM) as discussed by Kokare et al [13].

Table 1 shows the Average Retrieval Rate of database using NCC, CDM and ELM. Fig.2 illustrate the retrieval example of texture image D1 using different matching methods.

**Table 1.** Average Retrieval Rate of database using NCC, CDM and ELM

NCC	CDM	ELM
45%	71.71%	97.5%

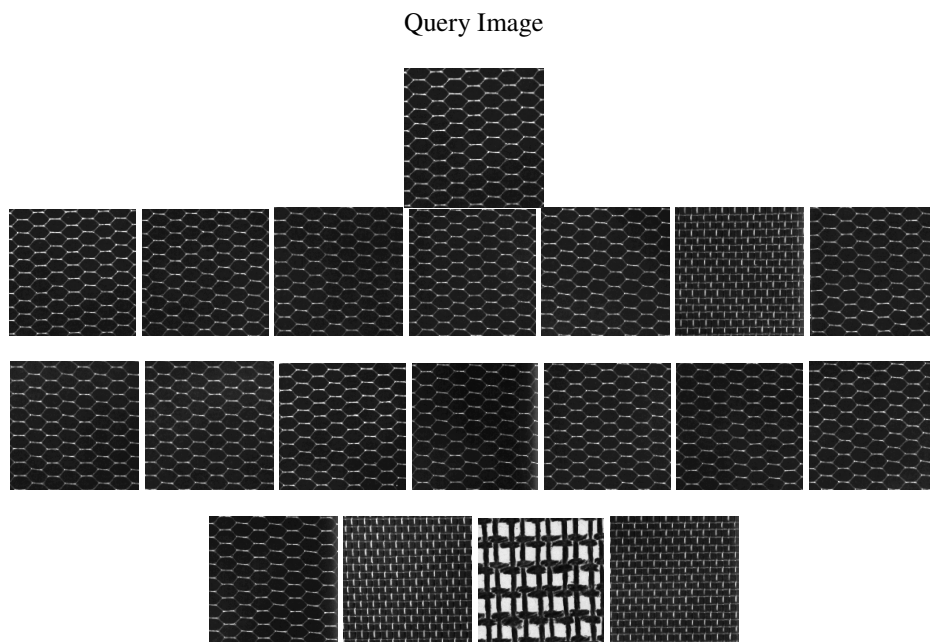


**Fig 2.** Retrieval examples for query image using Legendre moment

It is expected that the first sixteen retrieved images will be the ground truth images which belong to the same category. We have retrieved twenty images. It has been observed that using NCC the number of retrieved images from the same category are very few. More over some of the retrieved images are irrelevant. Using CDM result improved slightly. But with ELM, in most of the cases out of the twenty retrieved images fourteen to sixteen images are from ground truth images. More over other retrieved images are

very close to the query image. We evaluate the performance in terms of average rate of retrieving ground truth images as a function of the number of top twenty retrieved images.

## 5. CONCLUSION

Recently we find the use of texture feature for image matching, searching and indexing in CBIR system. Researchers are trying to establish the use of soft computing techniques for this purpose. ELM have been used for different types of image processing. But in this paper we have discussed ELM methods and have shown its superiority over other generally used matching methods using texture features. In future we will report the performance of ELM on images under intensity variation and noisy environment and the use (with comparison) of other soft computing methods.

## 6. REFERENCES

1. M.K.Hu, "Visual Pattern Recognition by moment invariants (1962)", IRE Trans. Inf. Theory 8 (1), pp 179-187.
2. C.H. The, R.T. Chin(1988), "On image analysis by the method of moments", IEEE Trans. Pattern Anal. Mach. Intell. 10 (4), pp 496-513
3. J. D. Zhou, H. Z. Shu, L. M. Luo, W. X. Yu, (2002), "Two new algorithms for efficient computation of Legendre moments", Pattern Recognition, Vol.35(5), pp. 1143-1152.
4. P. T. Yap and R. Paramesaran, (2005), "An Efficient Method for the Computation of Legendre Moments," IEEE Transactions on Pattern Recognition and Machine Intelligence, Vol.27, No.12, pp.1996-2002.
5. S. X. Liao, M. Pawlak, (1996), "On image analysis by moments," IEEE Transactions on Pattern Analysis and Machine Intelligence, Vol. 18(3), pp. 254-266.
6. Khalid M. Hosney, (2007), "Exact Legendre moments computation for gray level images", Pattern Recognition, Vol. 40, pp. 3597-3605.
7. C.W.Chong, R. Paramesran, R.Mukundan(2004), "Translation and scale invariants of Legendre moments", Pattern Recognition, Vol. 37, No.1, pp119-129.
8. JHaddadnia, K.Faez, P.Moallem (2001), "Neural network based face recognition with moment invariants", Proceedings of International Conference on Image Processing, vol.1, pp 1018-1021.
9. Thawar Arif, Zyad Shaaban, Lala Krekor, Sami Baba (2009), "Object classification via geometrical, zernike And legendre moments", Journal of Theoretical and Applied Information Technology, vol 7, no. 1, pp 31-37.

10. Khalid M. Hosny(2010), "*Robust Template Matching Using Orthogonal Legendre Moment Invariants*", Journal of Computer Science, vol. 6 (10), pp 1083-1087.
11. P Brodatz (1966), "*Texture: A Photographic Album for Artists & Designer*"s, New York: Dover.
12. [www.freefoto.com](http://www.freefoto.com)
13. Manesh Kokare, B.N.Chatterji and P.K.Biswas ( 2003 ), "*Comparision of Similarity Metrics for Texture Image Retrieval*", IEEE conference on convergent technology for Asia pacific region, TENCON 03, pp 571-575.

## Imaging Characteristics of a Birefringent Lens in the Infrared Region

Surajit Mandal<sup>1</sup> (Member SPIE), Ajay Ghosh<sup>2</sup>

<sup>1</sup>Department of Electronics & Communication Engineering,  
B. P. Poddar Institute of Management & Technology,  
Kolkata, Pin 700052, India

<sup>2</sup>Department of Applied Optics & Photonics,  
University of Calcutta,  
Kolkata, Pin 700009, India  
surajitmandal@yahoo.co.in

**Abstract.** In this communication, a new and novel design of an optical imaging system is presented which may be used to work in the infrared broadband illumination. The proposed system consists of a crystal quartz lens sandwiched between two linear polarizers. The optic axis of the crystal is perpendicular to the lens axis. The same system offers enhanced resolution or apodization depending on the relative orientations of the polarizers under infrared illumination having large bandwidth. It can also be fabricated to provide either large depth-of-focus or double focus even for broadband illumination.

**Keywords:** Optical imaging science; Infrared imaging; Chromatic aberration characteristics

### 1. INTRODUCTION

The techniques for pre-specified modification of the imaging characteristics of an optical system received considerable attention since the early days of systematic investigation of optical imagery [1-2]. It was found that the pupil function of any optical system plays an important role in this regard. The desired modification of the imaging characteristics is usually implemented by using a mask on the pupil of the optical system. Extensive studies have been carried out in this direction and the use of amplitude masks and phase masks have been reported [3-7]. Usually each mask is dedicated to a specific purpose and on-line modification of such masks is not possible. At the same time, synthesis of the pupil function for yielding a specific imaging characteristic is indeed a formidable task and remains practically insolvable except for some limitingly terminal and simple cases.

It has been recognized that the polarization properties of light, if ingeniously used, offers additional flexibilities to the optical designers that are unachievable by scalar wave properties alone [8-16]. The advantage of these polarization-based optical systems is that their imaging properties can be continuously altered *in situ*. Polarization is used as a parametric variable to introduce a variation in the complex amplitude of the pupil. Obviously, two degrees of freedom due to two orthogonal states of variation are available to continually change the imaging properties of these systems by varying the relative contributions of the two orthogonal components. However, fabrication and accurate alignment of such masks are quite troublesome and a considerable loss of light due to absorption, scattering etc. takes place in the masking element. Thus, a system, easily realizable, equally effective as well as free from the previously stated problems, had long been a requirement. Optical systems fabricated with birefringent materials have this potential and this motivated us to investigate the behaviour of a birefringent lens made of a uniaxial crystal [17-26]. A uniaxial birefringent lens sandwiched between two linear polarizers with its optic axis perpendicular to the lens axis behaves like an ordinary lens with a radially varying complex filter at its pupil plane [17-18]. Since the filter is generated because of the interference phenomenon, the problem associated with the alignment is removed. The imaging characteristics of the said system can be altered continuously just by changing the orientation of the any of the two polarizers. This makes the proposed system more versatile.

The imaging characteristics of the proposed system under diffraction-limited condition were studied [17-21]. The same system may be adapted either for enhanced resolution or for apodization just by rotating any polarizers included in the system. This system behaves as a double focus lens in general and by varying the birefringent lens parameters it is possible to change the separation between the two foci. The proposed system may be designed to obtain noticeably high depth-of-focus compared to an identical ordinary lens [19]. The imaging characteristics of the proposed system in presence of pre-specified on-axis and off-axis aberrations were studied [22-24]. It shows higher tolerance to the aberrations than an identical conventional lens. The effect of polychromatic visible light on the performance of the system was also investigated [25]. The study revealed that the focusing characteristics of the proposed system do not change appreciably under polychromatic illumination from that under strictly monochromatic illumination.

The need for appropriate infrared imaging devices and components has been on the rise [27-34]. The applications of proposed system under monochromatic or polychromatic beam illumination in the infrared region have not been explored till date. We study the viability of the proposed system considering crystal quartz as the birefringent lens material in the infrared region. In this connection it may be mentioned that the coefficient of absorption for the crystal quartz is less than  $0.030 \text{ cm}^{-1}$  in the region approximately from 190 nm to 2900 nm [35]. The infrared band is often subdivided into smaller sections though the divisions are different for different applications [36]. We consider the range of wavelengths for which infrared photography (700 nm to 900 nm) and short-wave infrared (SWIR) defence applications (900 nm to 1700 nm) usually take place. The wavelength of around 1550 nm is used for modern fiber-optic communication [37]. Thus the proposed

system may find applications in multiple domains, such as SWIR defence and surveillance purposes, infrared photography, medicine, archaeology, modern fiber-optic communication systems and many other infrared imaging devices. The axial irradiance distribution function and the intensity point spread function are considered as the image assessment parameters. The results show that all the above properties of the said system are retained even under infrared illumination having large bandwidth.

## 2. MATHEMATICAL FORMULATION

The proposed system is shown in a self-explanatory schematic diagram (Fig. 1).

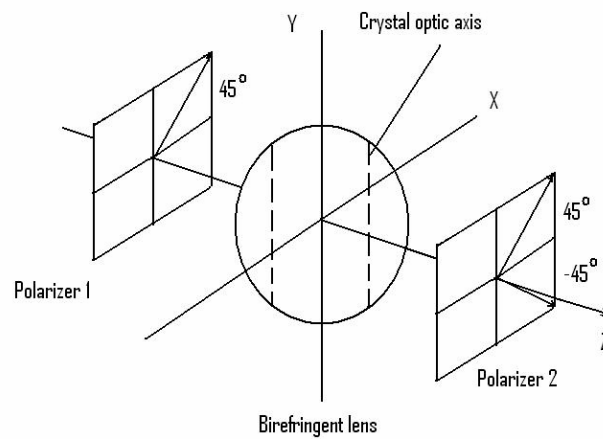


**Fig. 1.** The proposed system

When illuminated with a monochromatic beam of light, the IPSF of the proposed system under focused and defocused conditions with both parallel- and crossed-polarizers configurations may be given as [18-19]

$$\text{IPSF}(W_{20}) = 4 \left| \int_0^1 \frac{\cos}{\sin} [k\alpha(1-r^2)] \exp[ik(W_{20} - \sigma)r^2] J_0(\rho r) r dr \right|^2 \quad (1)$$

where  $k=2\pi/\lambda$  is the propagation constant,  $W_{20}$  is the defocus coefficient,  $\alpha = \delta n \frac{\Delta}{2}$  and  $\sigma = (\bar{n} - 1)\Delta = \frac{2(\bar{n} - 1)}{\delta n} \alpha$  are two design parameters of the birefringent lens,  $n_o$  and  $n_e$  are the ordinary and extraordinary refractive indices respectively,  $\delta n = n_e - n_o$  is the birefringence of the lens material,  $\bar{n} = \frac{n_o + n_e}{2}$  is the mean refractive index of the lens material and  $\Delta$  is the central thickness of the lens [17-19]. It may be mentioned in this connection that the parameter  $\alpha$  determines the number of interference rings formed on the aperture of the birefringent lens and  $\sigma$  indicates a shift of the focus for the said system with respect to the Gaussian image plane for an ordinary lens of similar dimensions [17-19]. The IPSF (1) is symmetric about  $W_{20} = \sigma$  [Figs. 4(b) and (c) of Ref. 19].

In order to evaluate the imaging behaviour of the proposed system under infrared broadband illumination, we employ the above IPSF expression under strictly monochromatic illumination. The wavelength dependent parameters are then identified and the modified expression is integrated over the specified wavelength range of the given polychromatic light with due consideration of the nature of variation of the wavelength dependent parameters with  $\lambda$ . Now,  $n_o$  and  $n_e$  vary with wavelength and so are  $\delta n$  and  $\bar{n}$ . It makes both  $\alpha$  and  $\sigma$  wavelength dependent parameters. The nature of variation of these parameters with  $\lambda$  is, however, a property of the crystal and is different for different crystals.

Identifying the  $\lambda$ -dependent terms, expression (1) may be rewritten as

$$\begin{aligned} \text{IPSF}_\lambda(W_{20}) &= 4 \left| \int_0^1 \frac{\cos[k_\lambda \alpha_\lambda (1-r^2)]}{\sin[k_\lambda \alpha_\lambda (1-r^2)]} \exp[ik_\lambda (W_{20} - \sigma_\lambda) r^2] J_0(\rho r) r dr \right|^2 \quad (2) \\ &= 4 \left| \int_0^1 \frac{\cos[k_\lambda \alpha_\lambda (1-r^2)]}{\sin[k_\lambda \alpha_\lambda (1-r^2)]} \cos[k_\lambda (W_{20} - \sigma_\lambda) r^2] J_0(\rho r) r dr \right. \\ &\quad \left. + i \int_0^1 \frac{\cos[k_\lambda \alpha_\lambda (1-r^2)]}{\sin[k_\lambda \alpha_\lambda (1-r^2)]} \sin[k_\lambda (W_{20} - \sigma_\lambda) r^2] J_0(\rho r) r dr \right|^2 \\ &= 4 \left[ \int_0^1 \frac{\cos[k_\lambda \alpha_\lambda (1-r^2)]}{\sin[k_\lambda \alpha_\lambda (1-r^2)]} \cos[k_\lambda (W_{20} - \sigma_\lambda) r^2] J_0(\rho r) r dr \right]^2 \\ &\quad + 4 \left[ \int_0^1 \frac{\cos[k_\lambda \alpha_\lambda (1-r^2)]}{\sin[k_\lambda \alpha_\lambda (1-r^2)]} \sin[k_\lambda (W_{20} - \sigma_\lambda) r^2] J_0(\rho r) r dr \right]^2 \quad (3) \end{aligned}$$

For a polychromatic illumination having flat-top spectral profile with mean wavelength  $\lambda_0$  and a spread of  $2\delta\lambda$ , the above expression becomes

$$\begin{aligned}
\text{IPSF}_{\text{poly}}(W_{20}) = & \frac{4}{2\delta\lambda} \int_{\lambda_0-\delta\lambda}^{\lambda_0+\delta\lambda} \left[ \int_0^1 \frac{\cos[k_\lambda \alpha_\lambda (1-r^2)] \cos[k_\lambda (W_{20} - \sigma_\lambda) r^2]}{\sin[k_\lambda \alpha_\lambda (1-r^2)]} J_0(\rho r) r dr \right]^2 d\lambda \\
& + \frac{4}{2\delta\lambda} \int_{\lambda_0-\delta\lambda}^{\lambda_0+\delta\lambda} \left[ \int_0^1 \frac{\cos[k_\lambda \alpha_\lambda (1-r^2)] \sin[k_\lambda (W_{20} - \sigma_\lambda) r^2]}{\sin[k_\lambda \alpha_\lambda (1-r^2)]} J_0(\rho r) r dr \right]^2 d\lambda
\end{aligned} \tag{4}$$

The above integral may be evaluated numerically by using 96-point Legendre-Gauss quadrature technique of integration [38] provided the nature of variation of  $\alpha_\lambda$  and  $\sigma_\lambda$  with  $\lambda$  is known. The variation of both  $\delta n_\lambda$  and  $\bar{n}_\lambda$  with  $\lambda$  for quartz crystal in the infrared region can be obtained using standard table [35].

For a polychromatic illumination with flat-top spectral profile having mean wavelength  $\lambda_0$  and a spread of  $2\delta\lambda$ , the axial irradiance distribution function for the proposed system (under diffraction-limited condition) with parallel and crossed-polarizers configurations is given by [19,25]

$$\begin{aligned}
I_{\text{poly}}(W_{20}) = & \frac{1}{2\delta\lambda} \frac{1}{4} \int_{\lambda_0-\delta\lambda}^{\lambda_0+\delta\lambda} \left[ \sin c^2\{W_{20} - (\alpha_\lambda + \sigma_\lambda)\} + \sin c^2\{W_{20} + (\alpha_\lambda - \sigma_\lambda)\} \right. \\
& \left. \pm 2 \sin c\{W_{20} - (\alpha_\lambda + \sigma_\lambda)\} \sin c\{W_{20} + (\alpha_\lambda - \sigma_\lambda)\} \cos\left(\frac{2\pi}{\lambda} \alpha_\lambda\right) \right] d\lambda
\end{aligned} \tag{5}$$

The above integral may again be calculated numerically by using 96-point Legendre-Gauss quadrature technique of integration [38].

### 3. RESULTS AND DISCUSSIONS

It was reported [26] that for  $\alpha \leq 0.375\lambda$ , the birefringent lens offers enhanced resolution under parallel-polarizers configuration while with crossed-polarizers configuration the same system acts as an apodizer under monochromatic illumination. We consider  $\alpha_{\lambda_0} = 0.25\lambda_0$  for further study. Fig. 2 and 3 show the variation of the IPSF for the said system at the Gaussian image plane under parallel- and crossed-polarizers configurations respectively at an operating wavelength ( $\lambda_0$ ) of 1300 nm with spectral spreads ( $2\delta\lambda$ ) of 0 nm, 200 nm, 400 nm and 800 nm. The IPSF for an ideal lens at the Gaussian image plane for monochromatic illumination has also been drawn for comparison.

It is revealed from the figures that a polychromatic input illumination does not affect considerably the inherent characteristics of enhanced resolution of such low-power birefringent lens (small  $\alpha$ ) under parallel-polarizers configuration even when the spectral

spread is 800 nm. The same system retains the property of apodization under the crossed-polarizers configuration when the spread is as high as 400 nm.

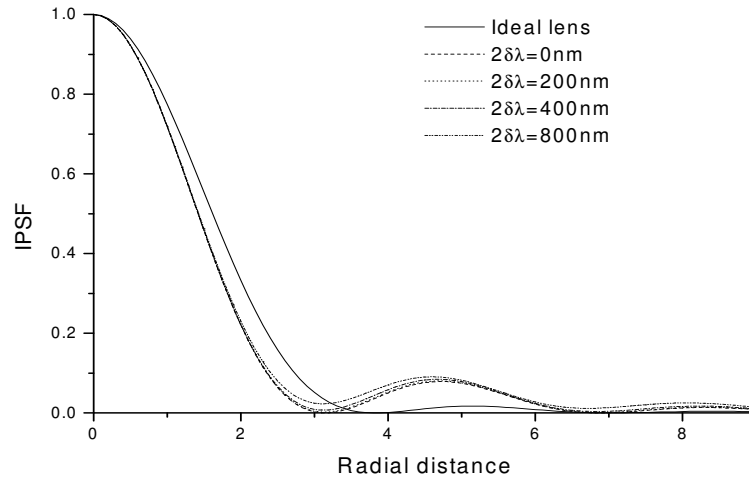


**Fig. 2.** The IPSF of a quartz crystal lens with  $\alpha = 0.25\lambda_0$  at the Gaussian image plane under parallel-polarizers configuration. Ideal lens: solid line, birefringent lens: dotted/dashed line.

It was also reported [26] that for  $0.375\lambda < \alpha \leq 0.625\lambda$  with crossed-polarizers configuration, the system gives enhanced resolution for monochromatic input illumination. Fig. 4 shows the influence of polychromatic illumination on the IPSF curve for  $\alpha_{\lambda_0} = 0.6044\lambda_0$  with crossed-polarizers configuration. In this connection it is to be mentioned that the said system offers the maximum depth-of-focus under diffraction-limited condition for  $\alpha = 0.6044\lambda$  with crossed-polarizers configuration for monochromatic input illumination [Fig. 3 of Ref. 19]. Now, an appreciable change in the IPSF curve takes place; in fact, the said system loses its characteristic of enhanced resolution at such a high value of  $\alpha$  as depicted in Fig. 4. With further increase of  $\alpha$ , the proposed system starts behaving as a double focus lens. Figs. 5 and 6 show the IPSF curve for  $\alpha_{\lambda_0} = \lambda_0$  under crossed-polarizers configuration at a mean wavelength of 1300 nm and spectral spreads 100 nm and 250 nm respectively. The said system retains its bifocal nature when the spread is 100 nm. However, the birefringent lens loses this property at higher spectral spreads (Fig. 6) due to incoherent superposition of resultant monochromatic vectors and unequal phase retardation suffered by different wavelengths constituting the polychromatic beam along the system axis.

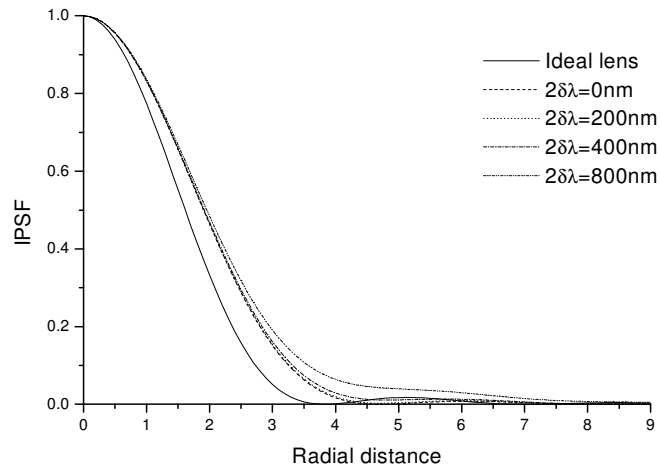


**Fig. 3.** Same as Figure 2 except that the proposed system is under crossed-polarizers configuration

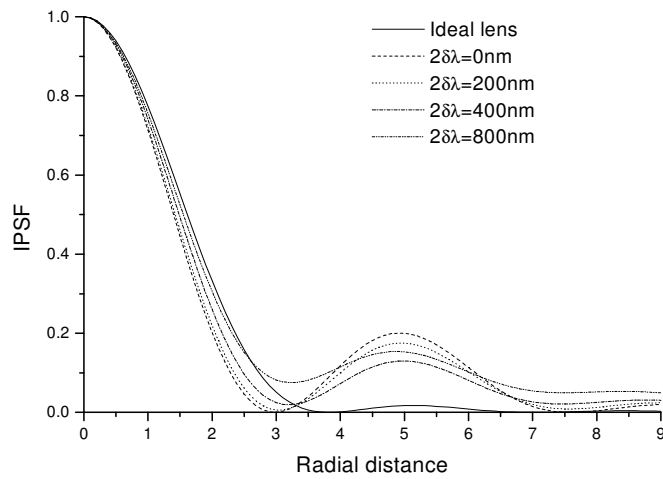


**Fig. 4.** Same as Figure 2 except that the said system is under crossed-polarizers configuration and  $\alpha = 0.6044\lambda_0$

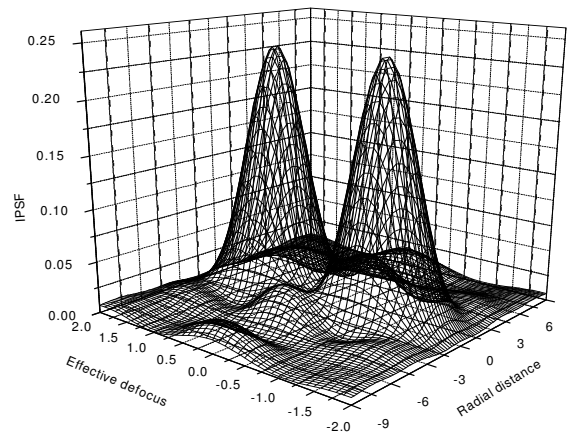


**Fig. 5.** Variation of IPSP with defocus for  $\alpha = \lambda_0$  under crossed-polarizers configuration when illuminated with a polychromatic beam of mean wavelength 1300 nm and spectral spread 100 nm

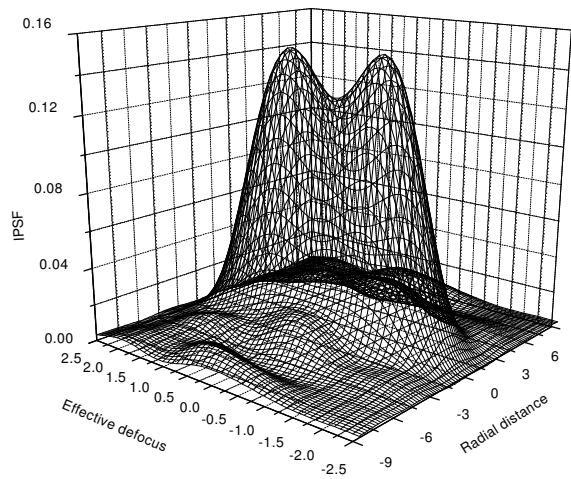


**Fig. 6.** Same as Figure 5 except that the spectral spread is 250 nm

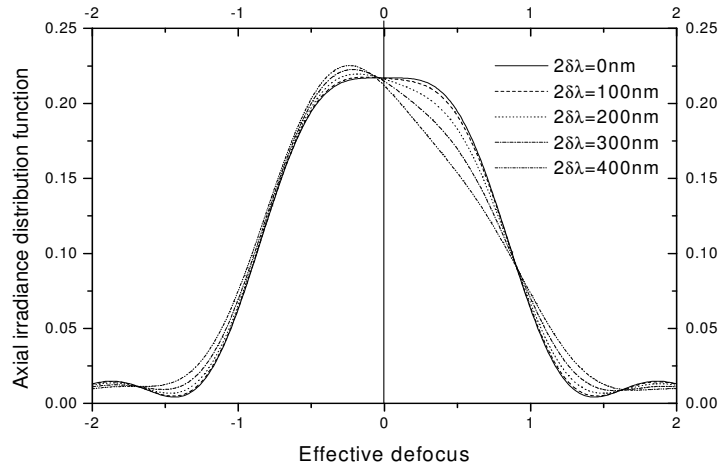


**Fig 7.** The axial irradiance distribution for a crystal quartz lens with  $\alpha = 0.3142\lambda_0$  under parallel-polarizers configuration

The proposed system offers the maximum depth of focus under diffraction-limited condition for  $\alpha = 0.3142\lambda$  with parallel-polarizers configuration for monochromatic input illumination (Fig. 2 of Ref. 13). This motivated us to study the focusing characteristics of the system under infrared broadband illumination for this specific value of  $\alpha$ . The axial irradiance distribution is computed for the proposed system under parallel-polarizers configuration at 1300 nm operating wavelength with spectral spreads of 0 nm, 100 nm, 200 nm, 300 nm and 400 nm (Fig. 7). It has been found that the allowable spectral bandwidth is approximately 100 nm at 1300 nm. The variation of the refractive indices as well as the birefringence with wavelength in this region is less and almost linear for crystal quartz. Thus the asymmetry of the axial irradiance distribution becomes less even when the spectral spread is 100 nm.

The results for our proposed system shown so far are for the mean wavelength of 1300 nm. However, the system retains the same property throughout the wavelength range from 700 nm to 1700 nm.

#### 4. REFERENCES

1. R. Straubel, *Peter Zeeman Verhandelingen*, Nijhoff, The Hague (1935).

2. R. K. Luneburg, *Mathematical Theory of Optics*, Brown University Press, Providence, R.I., p-391 (1944).
3. H. Osterberg and J. E. Wilkins Jr., "The resolving power of a coated objective", *J. Opt. Soc. Am.* 39, 553-557 (1949).
4. P. Jacquinet and B. Roizen-Dossier, "Apodization", *Progress in Optics III*, ed. E. Wolf, p- 29-186, North-Holland, Amsterdam, (1964).
5. B. J. Thompson, "Diffraction by semitransparent and phase annuli", *J. Opt. Soc. Am.* 55, 145-149 (1965).
6. T. Asakura and H. Mishina, "Diffraction by circular apertures with a ring shaped  $\pi$ -phase change", *Japan. J. Appl. Phys.* 9, 195-202 (1970).
7. J. W. Y. Lit, "Effects of a half wave filter in a portion of an aperture of a perfect lens", *J. Opt. Soc. Am.* 61, 297-302 (1971).
8. A. K. Chakraborty and H. Mukherjee, "Modification of PSF by polarisation mask", *J. Opt. (India)* 5, 71-74 (1976).
9. A. K. Chakraborty, B. Mondol Adhikari and R. Roychoudhury, "The optical transfer function of a perfect lens with polarization masks", *J. Opt. (Paris)* 9, 251-254(1978).
10. A. Ghosh, A. K. Chakraborty and K. Murata, "Imaging characteristics of a perfect lens partially masked by a linear polarizer", *Optik* 76, 153-156 (1987).
11. A. Ghosh, J. Basu, P. P. Goswami and A. K. Chakraborty, "Frequency response characteristics of a perfect lens partially masked by a retarder", *J. Mod. Opt.* 34, 281-289 (1987).
12. A. Ghosh, K. Murata and A. K. Chakraborty, "Frequency response characteristics of a perfect lens masked by polarizing devices", *J. Opt. Soc. Am. A.* 5, 277-284(1988).
13. K. Bhattacharya, A. Ghosh and A. K. Chakraborty, "Realization of phase and amplitude steps on lens aperture using polarization masks", *J. Opt.* 20, 128-131 (1991).
14. K. Bhattacharya, A. Ghosh and A. K. Chakraborty, "Vector wave imagery with a lens masked by polarizers", *J. Mod. Opt.* 40, 379-390 (1993).
15. K. Bhattacharya, A. K. Chakraborty and A. Ghosh, "Simulation of effects of phase and amplitude coatings on the lens aperture with polarization masks", *J. Opt. Soc. Am. A.* 11, 586-592 (1994).
16. S. N. Datta, A. Ghosh and A. K. Chakraborty, "Imaging characteristics of a lens zonally masked by polarizers and retarder", *Optik* 100, 1-7 (1995).
17. S. Sanyal, P. Bandyopadhyay and A. Ghosh, "Vector wave imagery using a birefringent lens", *Opt. Eng.* 37, 592-599(1998).
18. S. Sanyal and A. Ghosh, "Imaging characteristics of birefringent lenses under focused and defocused condition", *Optik* 110, 513-520 (1999).
19. S. Sanyal and A. Ghosh, "High focal depth with a quasi-bifocus birefringent lens", *Appl. Opt.* 39, 2321-2325 (2000).
20. S. Sanyal and A. Ghosh, "Frequency response characteristics of a birefringent lens", *Opt. Eng.* 41, 592-597 (2002).
21. S. Sanyal and A. Ghosh, "Image assessment of a birefringent lens based on the factor of encircled energy", *Opt. Eng.* 42, 1058-1064 (2003).
22. S. Sanyal and A. Ghosh, "High tolerance to spherical aberrations and defects of focus using a birefringent lens", *Appl. Opt.* 41, 4611-4619 (2002).
23. S. Sanyal, Y. Kawata, S. Mandal and A. Ghosh, "High tolerance to off-axis aberrations with a birefringent lens", *Opt. Eng.* 43, 1381-1386 (2004).

24. S. Sanyal, Y. Kawata, A. Ghosh and S. Mandal, "Frequency response characteristics of a birefringent lens with off-axis aberrations", *Appl. Opt.* 43, 3838-3847 (2004).
25. S. Mandal, S. Sanyal and A. Ghosh, "Imaging characteristics of a birefringent lens under broadband illumination", *Optik* 118, 335-339 (2007).
26. S. Sanyal, Ph D thesis, "Vector wave imagery using a birefringent lens", 2001.
27. G. Muyo, A. Singh, M. Andersson, D. Huckridge, A. Wood and A. Harvey, "Infrared imaging with a wavefront-coded singlet lens," *Opt. Exp.* 17, 21118-21123 (2009).
28. G. Muyo and A. R. Harvey, "Wavefront coding for athermalization of infrared imaging systems", *Proc. SPIE* 5612, p. 227-235 (2004).
29. G. Muyo, A. R. Harvey, and A. Singh, "High-performance thermal imaging with a singlet and pupil plane encoding", *Proc. SPIE* 5987, 162-169 (2005).
30. G. Muyo, A. Singh, M. Andersson, D. Huckridge, and A. Harvey, " Optimized thermal imaging with a singlet and pupil plane encoding: experimental realization", *Proc. SPIE* 6395, U211-U219 (2006).
31. D. J. Benford, M. C. Gaidis, and J. W. Kooi, "Optical properties of Zitex in the infrared to submillimeter", *Appl. Opt.* 42, 5118-5122 (2003).
32. A. Lompadó, E. A. Sornsin, and R. A. Chipman, "HN22 sheet polarizer, an inexpensive infrared retarder", *Appl. Opt.* 36, 5396-5402 (1997).
33. E. Oliva, S. Gennari, L. Vanzi, A. Caruso and M. Ciofini, "Optical materials for near infrared Wollaston prisms", *Astron. Astrophys. Suppl. Ser.* 123, 179-182 (1997).
34. S. Hejazi, R. A. Spangler, "A multi-wavelength thermal imaging system", *Engineering in Medicine and Biology Society*, 1989. *Images of the Twenty-First Century*, Proc. of the Annual International Conference of the IEEE Engineering 4, 1153-1154 (1989).
35. [http://www.mt-berlin.com/frames\\_cryst/crystals\\_frameset1.htm](http://www.mt-berlin.com/frames_cryst/crystals_frameset1.htm)
36. <http://en.wikipedia.org/wiki/Infrared>
37. J. M. Senior, *Optical Fiber Communications: Principles and Practice*, pp. 91, Prentice-Hall of India, 2<sup>nd</sup> Ed., New Delhi (2003).
38. M. Abramowitz and I.A. Stegun, *Handbook of Mathematical Functions*, Dover Publications, INC., NY (1972).

# A New Modulation and Coding Scheme for Free Space Optical Communication Using Turbo Coded BICM – ID with 16 QAM

A. Sarkar<sup>1</sup>, P. Saha<sup>2</sup>

<sup>1</sup>Dept. of ECE,  
Netaji Subhash Engineering College,  
Kolkata, India

<sup>2</sup>Dept. of ECE,  
B. P. Poddar Institute of Management and Technology,  
Kolkata, Pin-700052, India

**Abstract.** The main focus of this study is to enhance the performance of the existing terrestrial FSO links by introducing a well suited modulation and channel coding scheme. A major problem of FSO communication is the scintillation effect which causes the loss of a large amount of data as transient bursts. So, selecting an appropriate modulation and error control coding scheme for the FSO systems is an important issue today. Here we have introduced a new scheme using Turbo Coded BICM – ID (bit interleaved coded modulation with iterative decoding) with 16 QAM. This scheme would result in higher coding gain as well as lower bit error rate.

**Keywords:** BICM, FSO, Iterative decoding, QAM modulation, Turbo code.

## 1 INTRODUCTION

Free-space optical communication has attracted considerable attention recently for a variety of applications. This is because optical wireless systems can solve many of the long standing problems of providing low-cost, time-constrained, high – bandwidth communication in a variety of network scenarios. But their unreliability due to variations in atmospheric channel makes them the least deployed solutions so far. Atmospheric turbulence can degrade the performance of free-space optical links [1], particularly over ranges of the order of 1 km or longer. Inhomogeneities in the temperature and pressure of the atmosphere lead to variations of the refractive index along the transmission path. These index inhomogeneities can deteriorate the quality of the received image and can cause fluctuations in both the intensity and the phase of the received signal. These fluctuations can lead to an increase in the link error probability, limiting the performance

of communication systems. Aerosol scattering effects caused by rain, snow and fog can also degrade the performance of free-space optical communication systems. For the complexity associated with phase or frequency modulation, current free-space optical communication systems typically use intensity modulation with direct detection (IM/DD) [2]. An important issue with FSO communication is the scintillation effect which causes the loss of large amounts of data as transient bursts. Error control codes have been considered as a means for reducing the resulting bit errors. Atmospheric intensity variations due to scintillations in FSO channels can be modeled using a variety of distributions.

## **2. USE OF TURBO CODE IN FREE-SPACE OPTICAL COMMUNICATION**

Now a day, Turbo codes have caught coding theory researchers' attentions due to its near-Shannon-limit data transmission [4], very efficient forward error correction as well as high power efficiency. This coding scheme has been used in many applications such as data storage, wireless communications, third generation mobile system, satellite communications, telemetry and deep space communications as well as broadcasting system. Due to Turbo Codes' superior ability in error correction and power consumption to Convolution code and Reed-Solomon code, modern wireless technologies adopts the codes as a current standard coding scheme. Turbo Codes shift the complex coding functions to the receiver, which enhances the transmission communication performance very close to channel capacity. Moreover, turbo-codes are particularly efficient under strong turbulence conditions [3]. For relatively weak turbulence, however, a simple convolutional code makes a good compromise between decoding complexity and performance.

FSO, in the present, has already been used turbo codes with different types of modulation schemes such as intensity modulation/direct detection [2], PPM & MPPM [5], CDMA [6] etc. Also, Turbo Trellis coded modulation is used in FSO with PSK and QAM schemes [7]. With turbo codes, the transmitted data will definitely have lower bit error rates. However, the implementation might be costly and difficult.

The burst lengths of errors in the atmospheric channel are found to be ranging from a few milliseconds to hours making the channel highly unreliable. A rate-adaptive coding scheme [2] using variable length turbo codes has been proposed for single link FSO systems. Interleaving with error control coding can improve the code performance in case of small scale channel fluctuations. However, system outages due to extreme conditions can make the link completely useless. In such situations, along with error control codes, range reduction using multiple hops for communication has been proposed to increase availability. For a single FSO link with a fixed rate code, a fair throughput is obtained in good channel conditions provided the code used is of high rate. However, with a low rate code, the channel utilization is low. This system is unavailable for other channel

conditions. The fixed rate code was generated using the irregular LDPC code. The block length was set to be 11390. The code used is found to produce good rate-adaptive codes with rates between 0.5 and 0.9. Using an adaptive code leads to a better channel usage. However, in medium or bad channel conditions, the availability of this system also falls to zero.

### 3 THE NEW SCHEME USING TURBO CODED BICM\_ID WITH QAM

Inspired by BICM-ID schemes [8, 9], a new FSO scheme may be introduced using Turbo coded BICM – ID (bit interleaved coded modulation with iterative decoding) with 16 QAM. BICM-ID has a smaller free Euclidean distance compared to trellis coded modulation (TCM) but a larger diversity order. With iterative decoding, soft bit decision can be employed to significantly improve the conditional intersignal Euclidean distance. The block diagram of the FSO system using turbo coded BICM-ID is shown in Fig. 1.

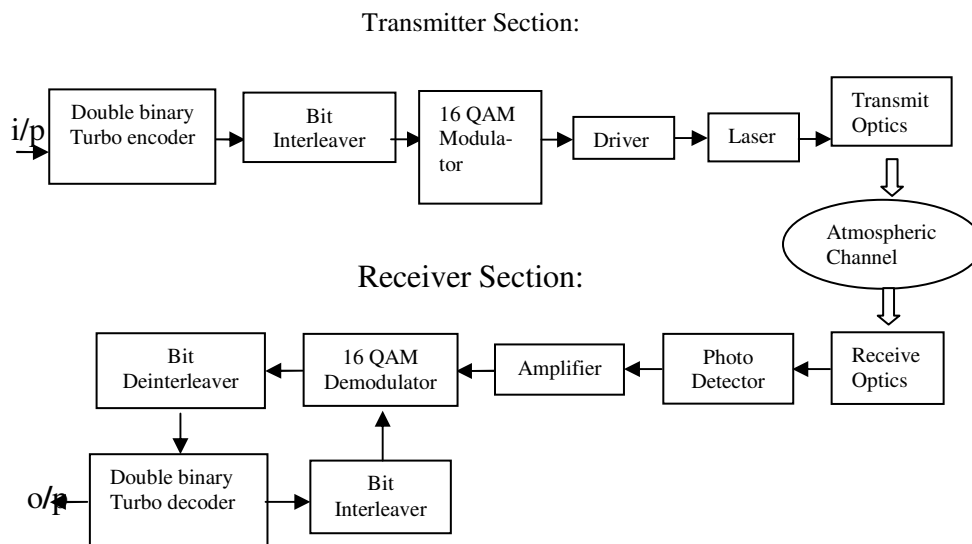


**Fig. 1.** Block diagram of FSO system using turbo coded BICM-ID with 16 QAM.

In this system, BICM introduces the use of an interleaver separating the encoder from the modulator. It produces a significant performance improvement over fading channels due to an increased diversity order. In receiver side, a joint decoding and demodulation scheme is used. The new system has two levels of iterations: turbo encoder and

demodulator feedback iterations. This whole system when joined with FSO, would improve the performance of FSO system.

#### 4. CONCLUSION

Using turbo code, this FSO system leads to a large coding gain. This scheme is already found to be very useful for flat fading Rayleigh channels. This approach should offer significant performance gains, but for a small increase in system complexity. For high SNR, turbo coded BICM-ID FSO system would converge to a high performance error free system.

#### 5. References

1. Xiaoming Zhu and Joseph M. Kahn, "Free-Space Optical Communication Through Atmospheric Turbulence Channels" – IEEE Transactions on Communications, vol. 50, no. 8, August 2002.
2. Jing Li (Tiffany) and Murat Uysal, "Achievable Information Rate for Outdoor Free Space Optical Communication with Intensity Modulation and Direct Detection" – GLOBECOM, IEEE, 2003.
3. Fang Xu, Mohammad-Ali Khalighi, Patrice Caussé and Salah Bourennane, "Performance of coded Time-Diversity Free-Space Optical Links" - 24th Biennial Symposium on Communications.
4. Claude Berrou and Alain Glavienx, "Near optimum Error correcting coding and decoding : Turbo – Codes" – IEEE Transactions on Comm. vol. 44, no. 10, October 1996.
5. Ivan B. Djordjevic, Bane Vasic, and Mark A. Neifeld, "Multilevel Coding in Free-Space Optical MIMO Transmission With Q-Ary PPM Over the Atmospheric Turbulence Channel" IEEE Photonics Technology Letters, vol. 18, no. 14, July 15, 2006.
6. Tanveer Ahmed Bhuiyan, Samiul Hayder Choudhury, Asif Al - Rasheed, and S.P. Majumder "Performance Analysis of a Free-Space Optical Code Division Multiple Access through Atmospheric Turbulence Channel" World Academy of Science, Engineering and Technology 56 2009.
7. Patrick Robertson and Thomas Wörz, "Bandwidth-Efficient Turbo Trellis- Coded Modulation Using Punctured Component Codes" – by IEEE Journal on Selected Areas in Communications, vol. 16, no. 2, February 1998.
8. X. Li and J. A. Ritcey, "Bit-interleaved coded modulation with iterative decoding" - IEEE Communications Letters, vol. 1, pp. 169-171, 1997.
9. Charbel Abdel Nour and Catherine Douillard, "Performance improvement using Turbo Coded BICM-ID with 16-QAM over Gaussian and Flat Fading Rayleigh Channels" - Proceedings / EXT / IST 05 / Papers/288.

# Implementation of an Audio Equalizer with User Specified Cut-off Frequencies in MATLAB GUIDE Using a Peak Filter

Saatwik Katiha

Department of Computer Science & Engineering,  
B.P. Poddar Institute of Management & Technology,  
Kolkata, Pin-700052, India

**Abstract.** This paper presents the implementation of an audio equalizer with user specified passband cutoff frequencies. This equalizer works on WAVE (Waveform Audio File Format) format audio files by the application of a peak filter and the ultimate implementation is achieved by a graphical user interface (GUI) designed using MATLAB GUIDE (graphical user interface development environment). Within the GUI, the user can equalize, play and save an equalized WAV file. The ultimate goal of such an equalizer is to allow the user specify the passband cutoff frequencies, thereby enhancing the usability of the equalizer in comparison to usual equalizers which provide no such control to the user. The equalizer designed herein presents the user with the option of specifying cutoff frequencies and a particular peak gain value for one pass band.

**Keywords.** Audio equalizer, MATLAB GUIDE, peak filter.

## 1. INTRODUCTION

Audio equalizers are used to boost or attenuate the levels of certain frequencies in an audio signal. They constitute the most common and important application of signal processing in the field of audio engineering and are used universally for recording as well as in live performances. Equalizers can, primarily, be divided into two categories [1] as:

### Graphic equalizers:

These contain a system of filters which individually correspond to a particular frequency band, each band being represented by the respective center frequency. Each of these filters can be individually controlled to provide a boost or cut to the corresponding frequencies.

### Parametric equalizers:

These provide the user with the option of specifying the gain, center frequency and bandwidth for equalization of the audio signal. These three parameters may or may not be independent of each other.

While graphic equalizers provide a simple interface for equalization purposes, they are not specific as the frequency bands which can be affected are predefined. Parametric equalizers allow for a more independent approach, but they still do not provide direct control of the passband cutoff frequencies to the user.

The equalizer implemented in this paper tries to provide the user with more control over the equalization process by providing total control of the passband frequencies as required.

The developmental tool used for this purpose is MATLAB GUIDE, which is a graphical user interface (GUI) development environment for MATLAB. Utilizing the tools provided in GUIDE, the process of creating the GUI layout and programming the GUI is simplified greatly. GUI components deployed for this equalizer allow the user to preview the equalized file by playing the equalized file back, pausing or resuming it, and saving the equalized WAV file.

## 2. BASIC THEORY

### (a) Theory of peak filters:

Peak filters are commonly used to shape the audio spectrum by boosting or suppressing frequencies in a particular range while allowing the frequencies outside this range to remain unaffected.

The following are the primary parameters used for design of a peak filter:

- G, the gain at the passband center frequency (in dB)
- $f_c$ , the center frequency (in Hz)
- $f_s$ , is the sampling frequency (in Hz)
- Q, the Q-factor.

Considering the transfer function of a digital biquad filter in the Z domain as:

$$H(z) = \frac{b_0 + b_1 z^{-1} + b_2 z^{-2}}{a_0 + a_1 z^{-1} + a_2 z^{-2}} \dots\dots(i)$$

To calculate biquad coefficients for the peak filter, the procedure [2] initially requires calculation of a few intermediate variables as follows:

$$A = \sqrt{10^{\frac{G}{20}}}$$

$$\omega_0 = 2 \cdot \pi \cdot \frac{f_c}{f_s}$$

$$\alpha = \frac{\sin(\omega_0)}{2 * Q}$$

Using the above, the values of the biquad coefficients are as follows:

$$b_0 = 1 + \alpha * A$$

$$b_1 = -2 * \cos(\omega_0)$$

$$b_2 = 1 - \alpha * A$$

$$a_0 = 1 + \frac{\alpha}{A}$$

$$a_1 = -2 * \cos(\omega_0)$$

$$a_2 = 1 - \frac{\alpha}{A}$$

To allow the user to specify the cutoff frequencies, basic formulae are used to calculate the center frequency ( $f_c$ ) and the Q-factor (Q) from the upper and lower cutoff frequencies ( $f_l$  and  $f_u$ , respectively) which are taken as inputs.

$$f_c = \sqrt{f_l * f_u}$$

$$Q = \frac{f_c}{f_u - f_l}$$

A point to be noted here is that the cutoff frequencies correspond to the points where the gain values are half of the gain at the center frequency [2].

(b) Working of MATLAB GUIDE

Using GUIDE allows the programmer to create the GUI layout along with a connected program file to control the operation of the GUI.

The GUI layout is created using the Layout Editor. Components such as text fields, panels, buttons, axes, sliders, menus etc. can be added to the layout area and their properties and position on the layout area manipulated within the layout editor.

To control this GUI, GUIDE automatically generates a code containing M-file, which provides code to instantiate the GUI and contains callback functions, which control how GUI components behave when a user interacts with them. These callback functions can be modified to control the behavior of the GUI to implement the required application. The

code file may also contain any further functions which might be required for the functioning of the GUI.

### 3 IMPLEMENTATION OF THE EQUALIZER

#### (a) GUI Layout

The GUI for the equalizer consists of the following components:

- (i) 'Edit Text' components to specify the upper and lower cutoff frequencies of the passband and the passband peak gain.
- (ii) 'Push Buttons' to open a WAV audio file, to play the file from the start, to pause/resume playing of the file and to save the equalized file as another WAV file.

To conform to the limits of audible audio frequencies, the cutoff frequencies are bound between 20Hz and 20000Hz. Similarly, to implement gain values which do not overly clip or suppress the signal, the limits for gain values are bound between -24 dB and +24 dB. These bounds are indicated as labels associated with the corresponding editable text fields.

The following figure displays the layout of the GUI:

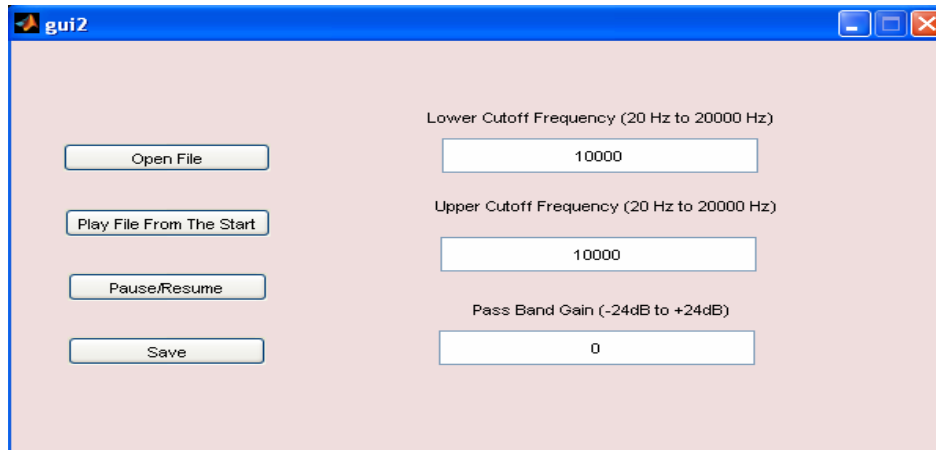


**Fig. 1.** Screenshot of the equalizer GUI

(b) GUI code M-file

The code file associated with the equalizer GUI is an M-file automatically generated by GUIDE. This code file contains the default initialization function which contains the initialization code to create an instance of the GUI, the creation and callback functions for the GUI components and a function which implements the peak filter. The callback functions and the peak filter implementation function are of relevance for implementation of the equalizer and are discussed below:

1) Callback functions

All the interactive components of the GUI have an associated callback function in the code file corresponding to the GUI. These callback functions are initialized by GUIDE itself along when the code file is generated. The callback functions associated with the equalizer GUI and the associated actions are as follows:

- i) **Opening function:** This is the first callback in a GUI code file. The tasks performed herein are those which need to be performed before the user accesses the GUI. In the current GUI, three primary flag variables are declared here: the 'isplaying' variable is set to 1 if the file is playing and to 0 if the file is not playing; the 'ispause' variable is set to 1 if the file is paused and to 0 if the file is playing and the 'wasplayed' variable is set to 1 if the file has been played and to 0 if it has not. These variables are initialized to 0 and set as global to allow for access by other functions in the code.
- ii) **Lower cutoff frequency editable text field callback function:** This function takes as input the value of the editable text box for the lower cutoff frequency of the passband. The input is taken as a string, so it needs to be converted to a double value for calculations. It is checked if this value is between 20Hz and 20000 Hz (conforming approximately to the bounds of human hearing) and if the value is found to violate this range, an appropriate error message is displayed using the `errordlg()` function.
- iii) **Upper cutoff frequency editable text field callback function:** This function works in exactly the same way as the callback function for the lower cutoff frequency editable text field.
- iv) **Gain editable text field callback function:** This function receives the values from the text field wherein the peak gain of the passband is specified. The range for gain, to avoid excessive suppression or clipping of the audio signal is from +24dB to -24dB. If the gain value specified by the user crosses this range, an error message is displayed.
- v) **'Open File' button callback function:** This callback function is used to display a dialog box whereby the user can select an audio file in the WAV format using the `uigetfile()` function. The path name of the file is stored in a variable called 'pathname' which is set to global for further use.

- vi) 'Play' button callback function: This function is associated with the 'Play File From The Start' button in the GUI. It takes the values of the upper and lower cutoff frequencies and peak gain from the corresponding text fields and gets filter coefficients from the peak filter implementation function using these. If the value of the lower cutoff frequency is found to be higher than that of the upper cutoff frequency, an error message is displayed. The actual filtering is done using the `filtfilt()` function (which applies the bidirectional audio filtering to the audio signal and allows for zero phase distortion [3][4]) and the `audioplayer()` function is used to create an audioplayer object which allows the file to play. The data array that stores the filtered data is declared global for further use. The `play()` function is used to play the file.

The play button, when pressed, sets the `wasplayed` variable to 1. When activating the entire playing and filtering sequence, it is checked if the file is already playing (using the `isplaying` variable). If not, filtering is applied as per user specified values and the file is played. The `isplaying` variable is set to 1 and `isplayed` variable is set to 0. If the file is already playing, the file is stopped, the filtering is applied again and the file is played from the start. The `isplayed` variable is set to 0. Algorithmically,

```

If (isplaying is zero)
  Apply the filter
  Play the file
  Set isplaying to 1
  Set isplayed to 0
Else
  Stop the file
  Apply the filter
  Play the file
  Set isplayed to 1.

```

- vii) 'Pause/Resume' button callback function: This function utilizes the `isplaying` and `isplayed` variables to check if the file is playing or is in a paused state. If the file is playing, the `pause()` function is used on the object created using the `audioplayer()` function. The `isplayed` variable is set to 1 and `isplaying` to 0. If the file is paused, the `resume()` function is used. The `isplayed` variable is set to 0 and `isplaying` to 1. Algorithmically,

```

If (isplayed is zero)
  Pause file
  Set isplaying to 0
  Set isplayed to 1

```

```

Else
Resume                               file
Set isplaying to 1
Set ispaused to 0.

```

- viii) 'Save' button callback function: This function is used to save the equalized WAV file to another WAV file. It is initially checked whether the 'wasplayed' variable is 0 or 1. If it is zero, the filter is applied and the file is saved directly. If the file is not zero, the filtered data from the callback function for the Play button is directly used and stored into a file using the wavwrite() function. This file (where the equalized file is to be saved) is specified by the user using the dialog box generated using the uiputfile() function.

#### 2) Peak filter implementation function

The implementation of the peak filter is done by creating a function that accepts the lower and upper cutoff frequencies, peak gain and the sampling frequency to generate the filter coefficients for the peak filter. The coefficients are calculated as per the formulae used in section II (a). To generate the filter, the filter coefficients are returned in a form consistent with the digital biquad filter form of equation (i). These coefficients can be used to filter the audio file using filtfilt() function.

## 4. RESULTS AND ANALYSIS

For analysis of the peak filter and the equalizer designed therefrom, an audio signal that has been provided a gain of +6dB in the frequency band from 8000 to 12000 Hz is considered. The coefficients for this peak filter obtained are as  $b_0 = 1.2839$ ,  $b_1 = -0.3479$ ,  $b_2 = 0.7161$  (numerator coefficients) and  $a_0 = 1.1423$ ,  $a_1 = -0.3479$ ,  $a_2 = 0.8577$  (denominator coefficients). To analyze the frequency response of the peak filter, MATLAB's freqz() function can be used, which plots the frequency response of a digital filter. For normalized frequency from 0 to  $f_s/2$ , the following plots are obtained:

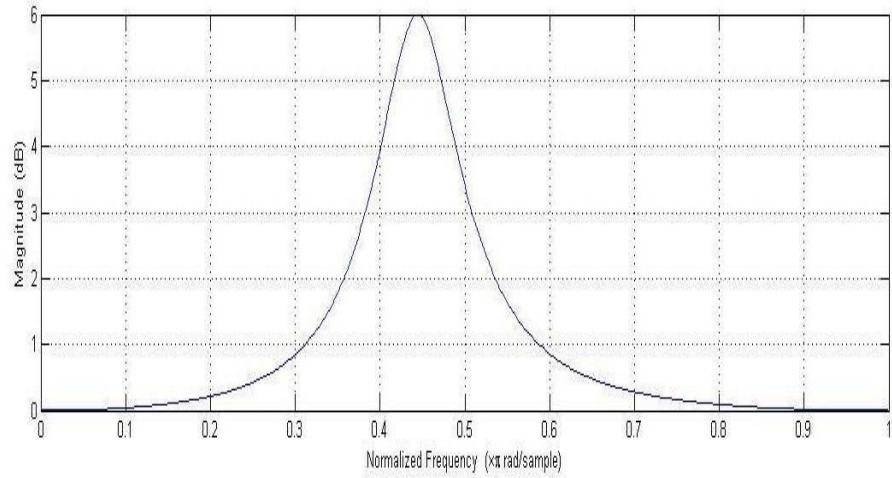


**Fig. 2.** Magnitude Response

The magnitude response shows that the peak gain is achieved at the center frequency of the passband, viz. from 8000Hz to 12000Hz.

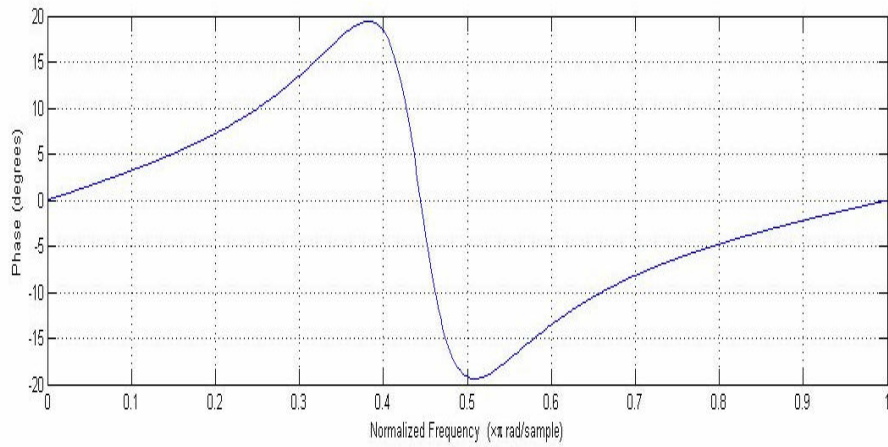


**Fig. 3.** Phase Response

The peak filter being an IIR filter, the phase response is non linear in nature. The use of the `filtfilt()` function nullifies this problem during the actual audio filtering operation by applying bidirectional filtering to achieve zero phase distortion[4-5].

The frequency analysis of application of equalization on an audio file can be done using by using the Fast Fourier transform (`fft()`) function[6]. Considering a sample WAV file, which has been treated to equalization in accordance with the above mentioned values, the amplitude spectrum for the input and output values are shown below:

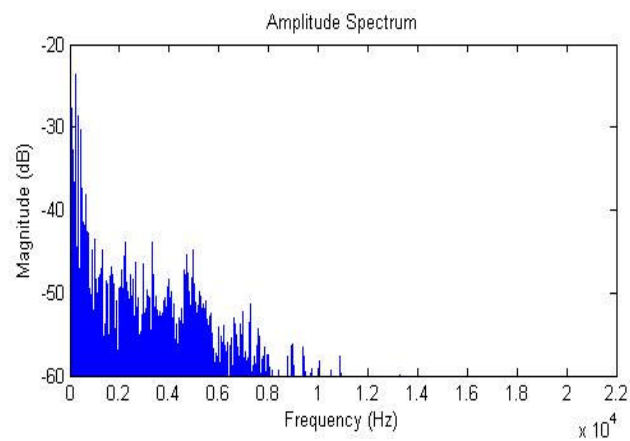


**Fig. 4.** Amplitude Spectrum of input file

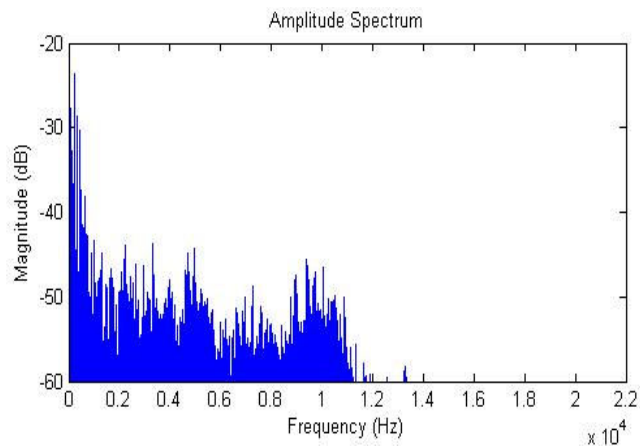


**Fig. 5.** Amplitude Spectrum of output file

The amplitude of the output file demonstrates a noticeable boost in the specified passband, compared to the input file.

## 5. CONCLUSION

The presented equalizer provides the user with an efficient way of equalizing an audio file with absolutely basic variables, i.e. cutoff frequencies and the peak gain for the passband. Thus, the implementation is more intuitive compared to other kinds of equalizers. The control of the Q-factor is also, in effect, in the hands of the user as the bandwidth and gain are also specified by him/her. By providing the file playing options, the equalizer allows the user to play the file as a preview and save the equalized file.

This equalizer design presents further scope for expansion. As it provides a conceptual implementation of equalization using user specified frequencies, it has been designed for only one adjustable band in the entire frequency range for an audio file. The provision for multiple effectible bands can enhance the usability of such an equalizer.

## 6. REFERENCES

1. Bohn, D. *Equalizer Designs & Choices*, 115<sup>th</sup> Convention of the AES, 2003, available at: [www.wildhoginthewoods.com](http://www.wildhoginthewoods.com).
2. Bristow-Johnson, R. *Cookbook formulae for audio EQ biquad filter coefficients*, available at: [www.music-dsp.org](http://www.music-dsp.org).
3. MATLAB Lecture 10.3 Audio processing, *UN/ESA/NASA/UAE Workshop, 2005*, available at: [www.aquaphoenix.com](http://www.aquaphoenix.com).
4. *Zero-phase digital filtering- MATLAB*, Product Documentation: Signal Processing Toolbox, available at: [www.mathworks.in](http://www.mathworks.in).
5. Smith, S. W. *Digital Signal Processing: A Practical Guide for Engineers and Scientists*, Newnes, pp. 329-332, 2002.
6. *Fast Fourier transform – MATLAB*, Product Documentation: MATLAB, available at: [www.mathworks.in](http://www.mathworks.in).

# Lasing Without Population Inversion

Lipika Adhya

Department of Engineering Physics  
B. P. Poddar Institute of Management and Technology  
Kolkata, Pin-700052, India

**Abstract.** In a non-conventional lasing action, amplification of radiation is possible without the inversion of the population between the two lasing levels in the active medium. The two-photon Adhya-Rai Dastidar absorption profile inputs an additional advantage in the gain profile in comparison to the single photon scheme.

**Keywords:** Amplification, population inversion

## 1. INTRODUCTION

Studies [1] on the emission from autoionizing (AI) states have shown that one of the ways to obtain the gain in the probe field is to search for the situation for which the absorption profile shows minima and hence the major part of the emission contributes to the gain in the probe field. If a system can be chosen such that the emission from a state results in a positive gain, although the population in the upper level is less than that in the lower level, lasing is said to occur without population inversion. It has been shown [2] that the minimum in the absorption of energy to the autoionizing states in the Fano profile [3] can be utilized to obtain a single-peak gain without population inversion. However the minimum in the absorption of energy to the autoionizing states in the Adhya-Rai Dastidar profile [4] can be utilized to obtain inversionless gain at different frequencies.

By LWOP or AWOP we mean **Lasing or Amplification** of weak probe radiation by atomic/molecular system **With Out Population Inversion** between upper and lower lasing levels of the system. For this new type of laser-LWOP, the idea of population inversion is no longer the criterion of lasing. It is the positive balance of photons emitted to photons absorbed, which has become the primary criterion for amplification. Depending on inversion and non-inversion of the population, the laser is labelled as conventional laser or a new type laser (LWOP) respectively.

The non-inversion lasing (LWOP) is possible due to the interference between energy absorbing transitions in the atoms/molecules of the lasing medium, making the probability of absorption of the photons drop to near zero, maintaining the probability of emission. As a result a few atoms in the excited state are enough to produce lasing.

To operate this type of LWOP, two well controlled lasers are required, one to create the interference and the other to trigger light emission, and a source of ordinary incoherent light to pump the upper lasing level by passing the blocked level.

There are two mechanisms for amplification without population inversion. One mechanism is based on atomic interference and the other is based on Fano-type interference. The first mechanism involves interference of different transitions, when there is a coherent superposition of atomic levels. There are two types of atomic level superposition formulating two schemes. In the  $\Lambda$ -type the interference of transitions are between the two closely spaced lower levels and an excited upper level (FIG), while in the V-type, the interference of transition is between two closely spaced excited levels and a lower level(. The Fano type interference, the upper lasing level is an autoionizing level, which lies above the lowest ionizing threshold. A destructive interference between the direct ionization channel and the auto-ionization channel, creates an asymmetric absorption profile, whereas the interference is absent for stimulated emission.

Using the Adhya-RaiDastidar type mechanism, we have considered a  $(1+1')$ -photon transition scheme involving bound Rydberg levels and autoionizing levels in H2 molecule. The effect of close lying rovibrational levels in the intermediate step and the presence of higher AI states embedded in the same continuum give rise to new features. (i) LWOP can be obtained from the higher AI state, although it is not being externally pumped and (ii) lasing at different closeby frequencies can be obtained when probe field frequency is tuned through resonances with intermediate rovibrational levels. This has been found to be suitable for obtaining gain in UV and VUV frequency range.

## 2. THEORY

The model system considered here is shown schematically in Fig. 1. A two photon transition from the lower lasing level  $|g\rangle$  to the upper lasing level  $|a\rangle$ , which is an autoionizing state, occurs via a resonant state  $|i\rangle$ .  $|b\rangle$  is another AI state embedded in the continuum  $|c\rangle$  adjacent to  $|a\rangle$  and is connected to it via configuration interaction through  $|c\rangle$ .  $V_{ac}$  and  $V_{bc}$  are the configuration-interaction couplings between  $|c\rangle$  and the AI states  $|a\rangle$  and  $|b\rangle$ , respectively.  $D_{pq}$ 's are the dipole transition moments between different product states.

Using the resolvent operator equation [5]

$$(z - H) G(z) = \mathbf{1},$$

where  $H = H_o + H_{rad} + H_{int}$  and where  $H_o$  is the Hamiltonian for the free atomic or molecular system,  $H_{rad}$  is the Hamiltonian for the free radiation field and  $H_{int}$  is the interaction between the atomic or molecular system and the radiation. One can derive a set of equations involving the matrix elements of the resolvent operators:

$$G_{pq}(z) = \langle p | \frac{1}{(z-H)} | q \rangle,$$

where  $|p\rangle$  and  $|q\rangle$  are the product states (i.e.,  $|g\rangle|n\rangle$ ,  $|i\rangle|n-1\rangle$ ,  $|a\rangle|n-2\rangle$ ,  $|b\rangle|n-2\rangle$  and  $|c\rangle|n-2\rangle$ ) and the choice of  $|q\rangle$  will be different for different boundary conditions.

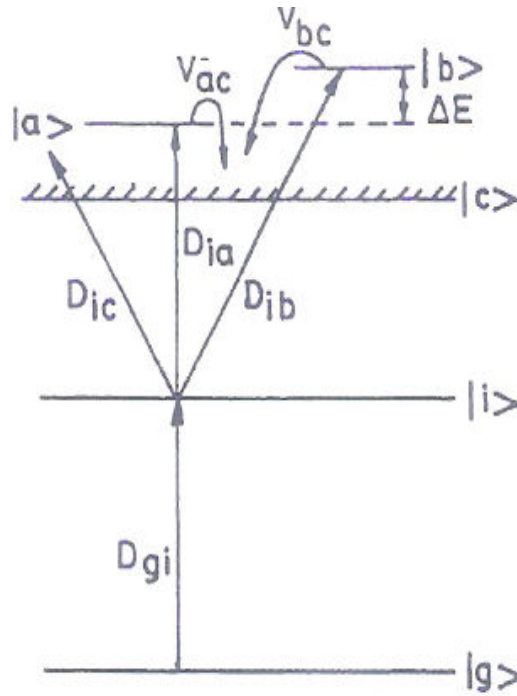


Fig. 1. Energy level diagram of the transition scheme.

By solving exactly for the poles of  $\mathbf{G}_p(z)$  which corresponds to the dressed-state energies (ref), one can obtain the corresponding matrix elements of the evolution operators  $|\mathbf{U}_p(t)|$  by the inverse Laplace transform  $\mathbf{G}_p(z)$  both for absorption and emission. Hence the population in the respective states are given as  $|\mathbf{U}_p(t)|^2$ , and the absorption and emission probabilities at a particular time  $t$  are obtained as

$$\mathbf{P}_{\text{abs}}(t) = 1 - |\mathbf{U}_a^g(t)|^2 - |\mathbf{U}_i^g(t)|^2,$$

$$\mathbf{P}_{\text{ems}}(t) = 1 - |\mathbf{U}_a^e(t)|^2 - |\mathbf{U}_i^e(t)|^2.$$

The superscripts a and e denote that the  $\mathbf{U}_p$ 's are obtained by solving for absorption and emission, respectively.

The gain in the system can be written as

$$\mathbf{G} = S_a \mathbf{P}_{\text{ems}}(t) - S_g \mathbf{P}_{\text{abs}}(t),$$

Where,  $S_a$  is the pumping rate to the upper lasing level  $|a\rangle|n-2\rangle$  and  $S_g$  that to the lower lasing level  $|g\rangle|n\rangle$ .

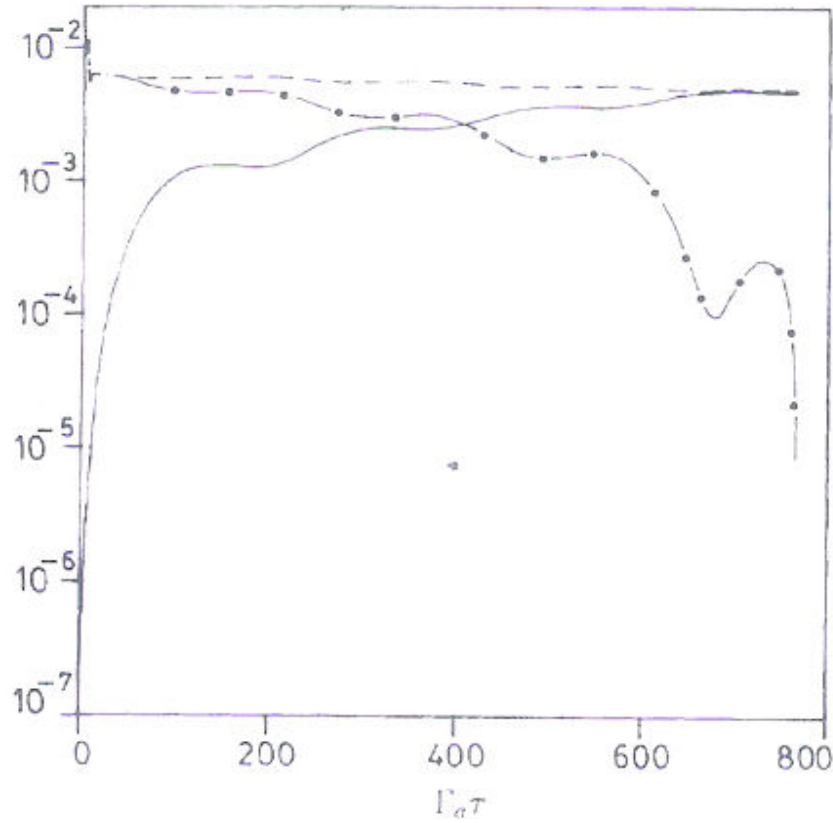


**Fig. 2.** Time dependence of total absorption  $\{P_{abs}\}$ , emission  $\{P_{ems}\}$  probabilities, and total gain  $(G)$ . Full line curve denotes  $P_{abs}$ ; dashed curve,  $P_{ems}$ ; dot-dashed curve, gain, all in arbitrary units

### 3. RESULTS AND DISCUSSIONS

The absorption, emission and gain profiles have been calculated as a function of time in units of AI lifetime  $\epsilon_a$  of state  $|a\rangle$  at a particular value of  $\epsilon_a$  and also corresponding line shapes as functions of  $\epsilon_a$ . Evolution of absorption, emission and gain with time for the present four-level scheme is shown in Fig 2. Comparing these results with that for the case

of (1+1)-photon amplification from a single AI state [5], it has been found that the gain persists for a longer period of time. The presence of the resonant intermediate state creates a bottleneck to the net absorption. This feature makes the (1+1)-photon scheme advantageous over the single photon.

In the (1+1)-photon transition scheme [6, 7] to the autoionization state, the Adhya-Rai Dastidar absorption profile (Fig.3) obtained exhibits a broad minimum extending over wide range of frequencies. Therefore, in the present scheme, the gain is possible in wide range of frequencies and it is peaked in two spectral ranges. However, there are two probes to measure the gain in this scheme. One is the single photon gain and the other is the two photon gain. It is quite apparent that compared to the single photon gain, the two photon gain is much stronger and peaked at two different regions (Fig.4).

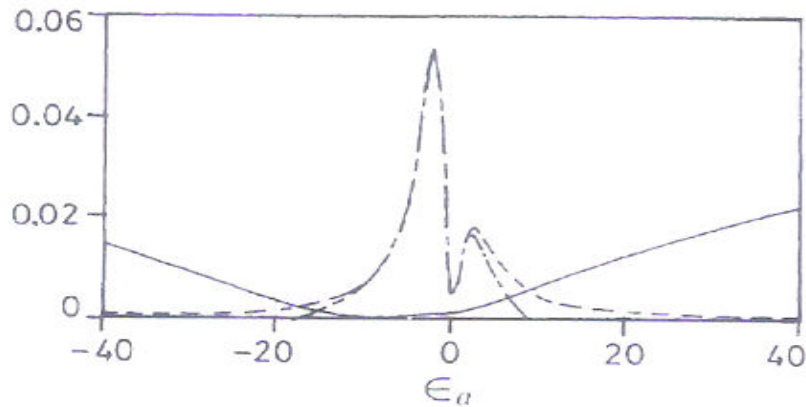


**Fig.3.** Profiles of total absorption, emission and gain for the (1+1)-photon scheme. Full line curve is absorption; dashed curve is emission; dot-dashed curve is gain.

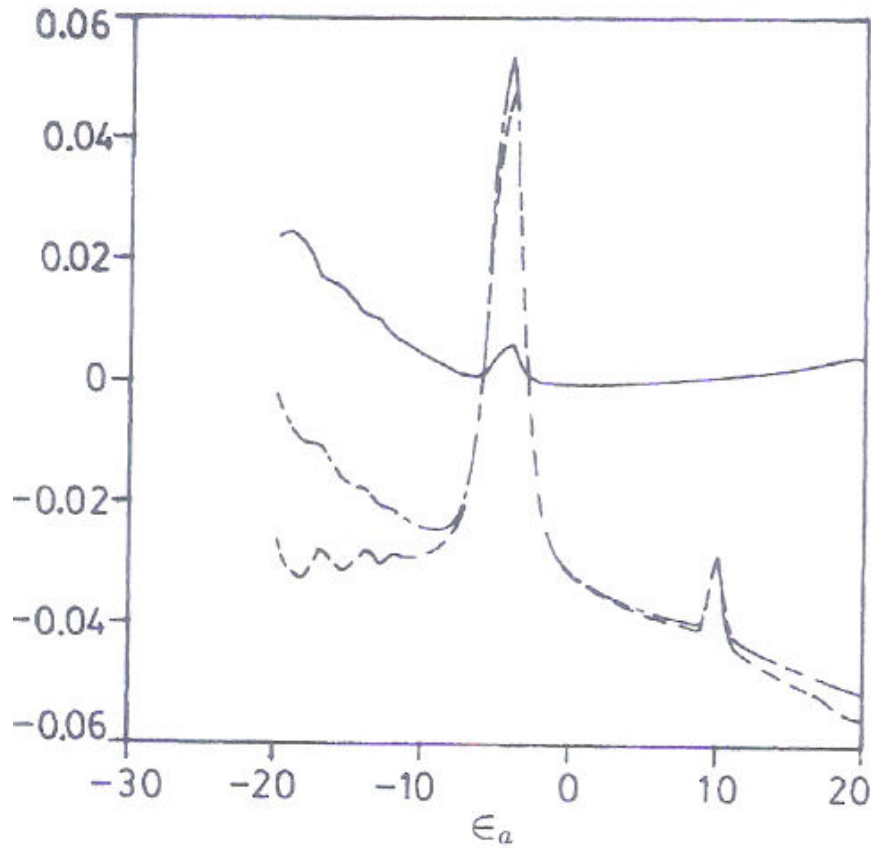


**Fig.4.** Profiles for single-photon, (1+1)-photon and total gain. Dashed curve is (1+1)-photon gain; full line curve is single-photon gain; dot-dashed curve is total gain.

In conclusion, it is shown that the unconventional lasing (LWOPI) is possible, even though the population of the higher lasing level has less population than the lower lasing level, giving the society a cost effective, energy saving laser. This LWOPI is still under investigation experimentally.

## References

1. G.S.Agarwal, S.Ravi and J.Cooper: Phys. Rev A, 41, 4721 (1990); 41, 4727 (1990).
2. O.A.Kocharovskaya and P.Mandel: Phys. Rev. A, 42, 523 (1990).
3. U.Fano, Phys. Rev. A 124, 1866 (1961).

4. L.Adhya and K.Rai Dastidar: Phys. Rev. A, 50, 3537 (1994).
5. P. Lambropoulos and P. Zoller, Phys. Rev. A 24, 379(1981); K. Rai Dastidar and P. Lambropoulos, *ibid.* 29,183 (1984).
6. L.Adhya and Rai Dastidar.K; Lasing without population inversion from autoionizing states; *Il Nuovo Cimento*, 14D, 643 (1992).
7. L. Adhya, S. Sanyal, and K. RaiDastidar, Phys. Rev. A 52, 4078 (1995); Nuovo Cimento D 20, 1283 (1998); K. Rai Dastidar, L. Adhya, and R. Das, *Pramana* 52, 281 (1999); G. Vemuri, K. V. Vasavada, and G. S. Agarwal, Phys. Rev. A 52, 3228 (1995).

## A three-element variable retarder for infrared monochromatic light using crystalline quartz

<sup>1</sup>Arijit Saha (Member SPIE),  
<sup>2</sup>Kallol Bhattacharya (Member SPIE), <sup>2</sup>Ajoy Kumar Chakraborty

<sup>1</sup>Department of Electronics & Communication Engineering,  
B. P. Poddar Institute of Management & Technology,  
137, VIP Road, Kolkata-700052, India  
Telefax: +91-33-25739401, email: arijit\_sh@yahoo.com

<sup>2</sup>Department of Applied Optics and Photonics, Calcutta University  
92, A.P.C. Road, Kolkata-700 009, India.  
Telefax: +91-33-23522411, email: kbaphy@caluniv.ac.in, akc\_000@rediffmail.com

**Abstract.** A technique for continuous variation of resultant retardance and effective privileged directions of a cascaded system of three retarders has been studied. The system consists of a rotatable retarder sandwiched between two fixed identical parallel retarders. Although the primary aim is to develop a simple technique for a variable retarder for monochromatic light, the robustness of the system for a narrow band on either side of the design wavelength is also studied. Simulated plots show that a linear variation of the effective retardance from 0 to  $2\pi$  is achievable, as also a linear variation of effective azimuth from 0 to  $\pi$ . It is also shown that these two parameters may be varied independently of each other. The system has been studied for quartz waveplates. The thicknesses have been calculated for the quarter and half waveplates at 1500 nm.

**Keywords:** Birefringent plate, Variable retarder

### 1. INTRODUCTION

Optical retarders are one of the major tools widely used in the study of polarization optics and laser-based instrumentation. Of the diverse types of optical retarders that are available, some show achromatism over a range of wavelengths [1], whereas in some cases these are wavelength sensitive and need to be reconfigured when used for different wavelengths. The necessity for retarders exhibiting variable retardation for monochromatic light is also in demand. Different methods have been employed for obtaining such types of variable retarders

Conventionally, wedge shaped uniaxial crystals have been used to fabricate variable retarders, e.g. Babinet-Soleil compensator. Variable retardance can also be realized by tilting a thin slice of uniaxial crystal plate cut normal to its optic axis. Such types of variable retarders, commonly known as Berek compensator, have been realized by utilizing the uniform frozen stress in resins [2]. Variable retardance can also be effected through the use of electro optic effects such as the Pockel effect. The major disadvantage of such retarders are the high operating voltages, 4 KV being the typical half wave voltage for a Pockel cell using  $\text{KD}^* \text{P}$  [3]. More recently, liquid crystal variable retarders are being widely used, where increasing voltage applied across the cell causes the liquid crystal molecules to rotate away from the optical windows, thereby modifying its retardance [4-8]. Switchable phase shifters using a combination of quarter and half waveplates have also been studied [9].

In the present study, we have considered a simple setup consisting of a cascaded system of three birefringent plates, of which the two end plates are retarders identical in all respects. It will be shown that this cascaded system of the three retarders behaves as a single zero-order variable retarder, showing a maximum variation of retardation from 0 to  $2\pi$ , simply by rotating the central plate from 0 to  $\pi$  without any change of the azimuth of the resultant polarization ellipse. On the contrary it is also possible to achieve a continuous variation of the azimuth from 0 to  $\pi$  of the resultant vibration, for a fixed magnitude of retardation. The simple technique of Jones calculus is used in the analysis.

## 2. THEORY

Consider a combination of three birefringent plates, the two extreme plates having their retardations identical, and the central plate having a different retardation value. The two extreme plates have their privileged directions mutually parallel, whereas the central plate is rotated by an angle  $\phi$  with respect to the two outer plates. It will be shown that the combination of these three birefringent plates will behave as a single equivalent retarder whose retardation value can be varied over a wide range by rotating the central plate.

With reference to figure 1,  $\delta_1$  is the common retardation of the two outer plates and  $\delta_2$  is that of the central plate. The angle between the fast axis of the central plate and that of the two extreme plates is given by  $\phi$  as shown in Fig.1.

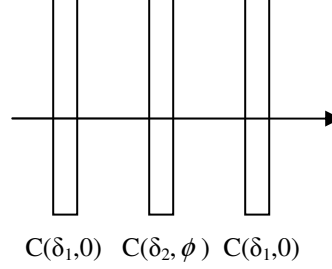


**Fig 1.** Configuration of the three birefringent plates.

The Jones matrix of a retarder whose fast axis coincide with the X-axis is given by

$$C(\delta, 0) = \begin{vmatrix} e^{i\delta/2} & 0 \\ 0 & e^{-i\delta/2} \end{vmatrix} \quad (1)$$

where  $\delta$  is the phase difference introduced by the retarder.

The Jones matrix of an oblique retarder whose fast axis makes an angle  $\phi$  with the X-axis is given by

$$C(\delta, \phi) = \begin{vmatrix} \cos \frac{\delta}{2} + i \sin \frac{\delta}{2} \cos 2\phi & i \sin \frac{\delta}{2} \sin 2\phi \\ i \sin \frac{\delta}{2} \sin 2\phi & \cos \frac{\delta}{2} - i \sin \frac{\delta}{2} \cos 2\phi \end{vmatrix}. \quad (2)$$

Hence, the Jones matrix of the cascaded system considered above is

$$C(\Delta, \psi) = C(\delta_1, 0)C(\delta_2, \phi)C(\delta_1, 0) \quad (3)$$

where  $\Delta$  and  $\Psi$  are the equivalent retardation and orientation of the effective fast axis of the combination respectively.

Using the appropriate Jones matrices we may write

$$C(\Delta, \psi) = \begin{vmatrix} e^{i\delta_1/2} & 0 \\ 0 & e^{-i\delta_1/2} \end{vmatrix} \begin{vmatrix} \cos \frac{\delta_2}{2} + i \sin \frac{\delta_2}{2} \cos 2\phi & i \sin \frac{\delta_2}{2} \sin 2\phi \\ i \sin \frac{\delta_2}{2} \sin 2\phi & \cos \frac{\delta_2}{2} - i \sin \frac{\delta_2}{2} \cos 2\phi \end{vmatrix} \begin{vmatrix} e^{i\delta_1/2} & 0 \\ 0 & e^{-i\delta_1/2} \end{vmatrix}$$

$$= \begin{vmatrix} e^{i\delta_1} \cos \frac{\delta_2}{2} + i e^{i\delta_1} \sin \frac{\delta_2}{2} \cos 2\phi & i \sin \frac{\delta_2}{2} \sin 2\phi \\ i \sin \frac{\delta_2}{2} \sin 2\phi & e^{-i\delta_1} \cos \frac{\delta_2}{2} - i e^{-i\delta_1} \sin \frac{\delta_2}{2} \cos 2\phi \end{vmatrix} \quad (4)$$

This may be expressed as

$$= \begin{vmatrix} \cos \frac{\Delta}{2} + i \sin \frac{\Delta}{2} \cos 2\Psi & i \sin \frac{\Delta}{2} \sin 2\Psi \\ i \sin \frac{\Delta}{2} \sin 2\Psi & \cos \frac{\Delta}{2} - i \sin \frac{\Delta}{2} \cos 2\Psi \end{vmatrix} \quad (5)$$

Equating the real and imaginary parts of equations (4) and (5), we obtain

$$\cos \frac{\Delta}{2} = \cos \delta_1 \cos \frac{\delta_2}{2} - \sin \delta_1 \sin \frac{\delta_2}{2} \cos 2\phi \quad (6)$$

$$\text{and} \quad \cot 2\Psi = \operatorname{cosec} 2\phi \left( \sin \delta_1 \cot \frac{\delta_2}{2} + \cos \delta_1 \cos 2\phi \right) \quad (7)$$

Equations (6) and (7) are the governing equations.

### 3. COMPUTATION OF THE EQUIVALENT PARAMETERS

From equations (6) and (7) it appears that  $\Delta$  and  $\Psi$  of the combination are in general, dependent on each other. However, it will be shown that for some specific values of  $\delta_1$  and  $\delta_2$ , these two parameters may be varied independently of each other.

Considering that all the plates are fabricated for a design wavelength 1500 nm, the retardation  $\delta$  introduced by a birefringent plate between the two orthogonal components of light is given by

$$\delta = \frac{2\pi}{1500 \times 10^{-9}} (n_e - n_o) d \quad (8)$$

where  $(n_e - n_o)$  is the birefringence of the material of the retarders and  $d$  is the thickness of each plate.

The values of birefringence for quartz for a range of 200 nm of wavelengths in the infrared region are presented in table 1 [10]. For a design wavelength of 1500 nm, the thicknesses required for quarter and half waveplates are calculated to be 44.12  $\mu\text{m}$  and 88.24  $\mu\text{m}$  respectively.

For the simulated results that follow, the individual components of the composite arrangement as shown in Fig.1, consists of either half wave plates or quarter wave plates. In each of the cases the parameters  $\Delta$  and  $\Psi$  are evaluated at the design wavelength 1500nm, 1400nm and 1600nm, so as to accommodate effects introduced by quasi-monochromatic sources.

**Table 1. Values of birefringence**

Wavelength (nm)	Birefringence ( $n_e - n_o$ )
1400	0.0085
1500	0.0085
1600	0.0084

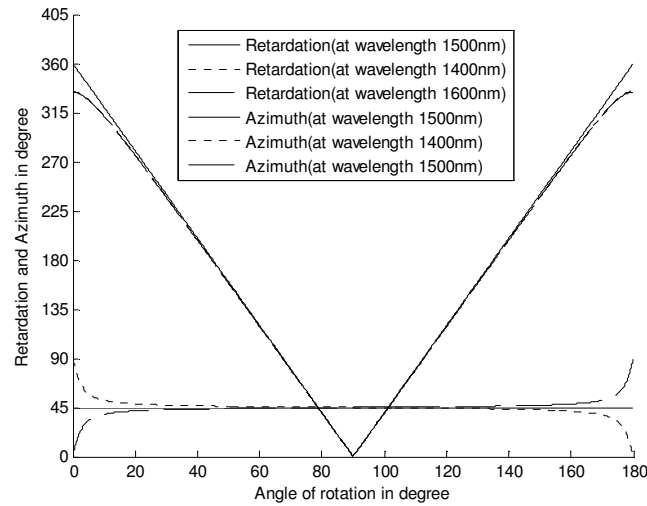


**Fig 2.** (a) The proposed setup. (b) Variation of the overall retardation and azimuth for the combination of two parallel  $\lambda/4$  plates and the central  $\lambda/2$  plate, while the central plate has been rotated from 0 to  $\pi$ .

The effect of rotating the central plate of the cascaded system, where the bounding retarders are quarter-wave plates and the central retarder is a half-wave plate is shown in Fig.2a and Fig.2b. The azimuth of the output remains constant at  $\pi/4$ , although the overall

retardation linearly varies through  $2\pi$  with an  $180^\circ$  rotation of the central half wave plate. We have also calculated the effect when the light is not ideally monochromatic. We have considered the overall effect of the system for a range of  $\pm 6.7\%$  of the design wavelength of light 1500 nm, which is quite a good approximation for laser light.

For a complementary configuration where the two end plates are half-wave plates and the central plate is a quarter wave plate as shown in Fig 3(a), the retardation remains constant at  $3\pi/2$  while the azimuth varies linearly from  $\pi$  to 0 with the rotation of the central half wave plate from  $90^\circ$  to  $270^\circ$ . As in the previous case, the results have been computed for  $\pm 6.7\%$  of 1500 nm.

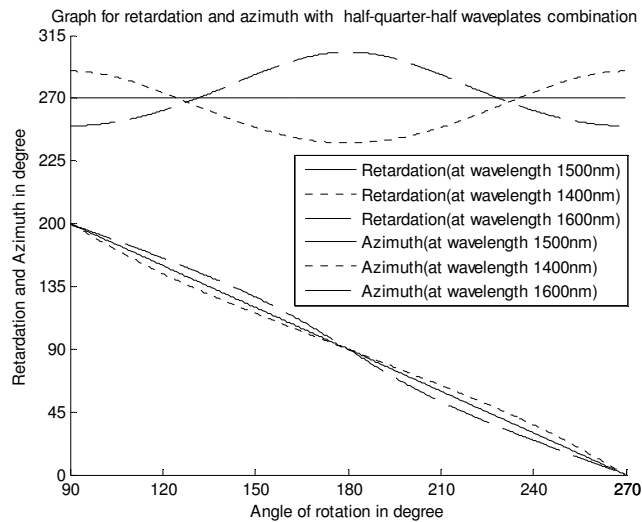


**Fig 3.** (a) The proposed setup. (b) Variation of the overall retardation and azimuth for the combination of two parallel  $\lambda/2$  plates and the central  $\lambda/4$  plate, while the central plate has been rotated from  $\pi/2$  to  $3\pi/2$ .

#### 4. DISCUSSIONS AND CONCLUSION

The numerical calculations of the transmission characteristics of the proposed system show that it acts as an efficient zero-order variable retarder for monochromatic infrared light at 1500 nm. However, combinations that result in linear changes of retardance and/or

direction of birefringence have been presented, in both of which the central retarder is rotated to effect the said variations.

A practical implementation of the proposed scheme would incorporate a mechanical arrangement where the central retarder may be rotated relative to the identically oriented and fixed bounding retarders. A circular scale attached to the former would indicate the relative orientation of its fast axis with respect to the latter.

With the proposed combinations it is possible to vary the polarization states so as to follow any desired latitude or longitude on the Poincaré sphere. It is also expected that the proposed device will be less sensitive to non-normal incidence since the combinations result in zero-order variable wave plates. However, these aspects have not been elaborated in the present report.

It is anticipated that inter-reflections at the interfaces of the elements constituting the variable retarder would negatively affect its performance. These may be reduced in a number of ways, the standard practice being the application of a suitable antireflection coating on the faces of the plates.

## 5. REFERENCES

1. S. Pancharatnam, "Achromatic Combinations of Birefringent Plates, Part II. An Achromatic Quarter-Wave Plate", *The Proceedings of the Indian Academy of Sciences*, Vol. XLI, No.4 Sec. A, pp.137-144 (1955).
2. W. A. P. Fisher, "A Large Field compensator of the Berek type", *Nature*, Vol. 161, No. 4100, pp. 848-848, (May 1948)
3. R. E. Fischer, B.T-Galeb and P. R. Yoder, *Optical System Design 2<sup>nd</sup> ed.*, p.554, *Mc Graw Hill Companies Inc.* (2008).
4. P. Hariharan and P. E. Ciddor, "Achromatic phase-shifters: 2. A quantized ferroelectric liquid-crystal system", *Optics Communications*, Vol. 117 Issue 1-2, pp. 13-15 (May 1995).
5. Alan M. Title and William J. Rosenberg, "Achromatic retardation plates", *Polarizers and Applications, SIPE Proceedings*, Vol. 307, pp. 120-125 (1981).
6. Alan M. Title, "Improvement of Birefringent Filters. 2: Achromatic Waveplates", *Applied Optics*, Vol. 14, No. 1, pp. 229-237 (Jan. 1975).
7. C.M. McIntyre and S.E. Harris, "Achromatic Wave Plates for the Visible Spectrum", *J. Opt. Soc. of America*, Vol. 58, Issue 12, pp. 1575-1580 (Dec. 1968).
8. H. W Lee and Chih-Kung Lee, "Nematic liquid crystal variable retarder and retardation modulator", *Proc. SPIE* Vol. 2873, pp. 305-309 (August 1996).
9. P. Hariharan and P. E. Ciddor, "Improved switchable achromatic phase shifters", *Optical Engineering*, Vol. 38, Issue 6, pp. 1078-1080 (June 1999).
10. J M Bennet, "Polarizers", Chapter 3 in vol. 2 of *Handbook of Optics*, M. Bass, Ed., pp. 3.46-3.49 (McGraw-Hill, New York, 1995).

# A Novel Technique for Computing the Polychromatic Optical Transfer Function of Optical Imaging Systems

Surajit Mandal<sup>1</sup> (Member SPIE), Ajay Ghosh<sup>2</sup>

<sup>1</sup>Department of Electronics & Communication Engineering,  
B. P. Poddar Institute of Management & Technology,  
Kolkata, Pin 700052, India

<sup>2</sup>Department of Applied Optics & Photonics,  
University of Calcutta,  
Kolkata, Pin 700009, India  
surajitmandal@yahoo.co.in

**Abstract.** A new method for accurate and efficient computation of the polychromatic optical transfer function (OTF) of an optical system is presented. The expression is useful in the theoretical analysis of any optical imaging system. The technique is used to evaluate the polychromatic OTF of a clear aperture isotropic lens. Some specific cases are computed and illustrated graphically.

**Keywords:** Optical imaging science; Chromatic aberration characteristics; Polychromatic OTF

## 1 INTRODUCTION

Evaluation of the performance of optical systems by means of polychromatic OTF is now a standard procedure [1-15] because of the fact that experimental evaluation of the OTF is possible and measuring instruments are available for this purpose. Several computation techniques have been reported in the recent past for obtaining the polychromatic OTF. Barnden [2-3] used the autocorrelation method for calculating a series of monochromatic OTFs for equally spaced wavelengths directly from the polynomial fitted to the wave aberration after ray-tracing. These OTFs are then weighted according to the source-detector characteristics and summed over the given wavelength range. Takeda [4] reported that lenses with completely different chromatic aberrations may have the same polychromatic OTF. Bescos *et al.* [5] suggested of using a set of three polychromatic OTFs covering three different wavelength bands, one for each tristimulus value when the final receiver is the human eye. Such an approach has found applications as test functions for apodizing filters in colour imaging [6] and in design of filters for digital restoration of colour images [7]. Navajas *et al.* [8-9] proposed the technique of polychromatic

modulation transfer function (MTF) measurement for photographic systems because it reduces the time for measurement and calculation. Evaluation of the polychromatic OTF considering single phase-space representations (such as the ambiguity function and the Wigner distribution function) to obtain the set of monochromatic OTFs was suggested by Furlan *et al.* [12]. Subbarao [11] and Mahajan [14] reported similar methods for obtaining the polychromatic OTF of a diffraction-limited system just by integrating the OTF obtained for incoherent monochromatic illumination over a given spectral range. An average sampled modulation transfer function describing discrete, sampled display systems was obtained by Helseth [15].

In this communication, a novel technique is proposed for direct, accurate and efficient computation of the polychromatic OTF of an optical system. We apply our technique for computation of the polychromatic OTF of a clear aperture isotropic lens. The OTF of the said system at a particular wavelength is obtained from the autocorrelation of the pupil function. The polychromatic OTF is computed directly by integrating the monochromatic OTF over the entire spectral bandwidth of the white light taking into consideration the nature of variation of the wavelength dependent parameters. The technique will be useful not only for conventional optical systems but also for systems that includes any wavelength dependent component. For simplicity, the spectral profile of the wide-bandwidth source is considered to be uniform and the spectral sensitivity of the detector is neglected.

## 2 MATHEMATICAL FORMULATION

It was shown by Duffieux [16] and Hopkins [17] that for rotationally symmetric optical systems, the normalized monochromatic frequency response function is given by

$$OTF(s) = \frac{\int_{-\infty}^{\infty} \int_{-\infty}^{\infty} \Omega\left(x + \frac{s}{2}, y\right) \Omega^*\left(x - \frac{s}{2}, y\right) dx dy}{\int_{-\infty}^{\infty} \int_{-\infty}^{\infty} \Omega(x, y) \Omega^*(x, y) dx dy} \quad (1)$$

where  $\Omega(x, y)$  is the pupil function of the optical system,  $\Omega^*$  is the complex conjugate of  $\Omega$ , and  $s$  is the normalized spatial frequency ( $0 \leq s \leq 2$ ).

The normalized spatial frequency variable  $s$  may be related to the system parameters by the relation

$$s = \frac{\lambda v}{\text{Numerical aperture in the object space}} = \frac{\lambda v'}{\text{Numerical aperture in the image space}} \quad (2)$$

where,  $v$  and  $v'$  are the number of lines per unit length in the object and the image respectively.

The area of integration [17], though formally extends over an infinite plane, is effectively limited to the area of overlap of the two unit circles shifted equally in opposite directions as shown by the shaded region in Fig. 1. Omission of the off-axis aberrations results in a circularly symmetric pupil function and the integration over each quadrant yields identical results.

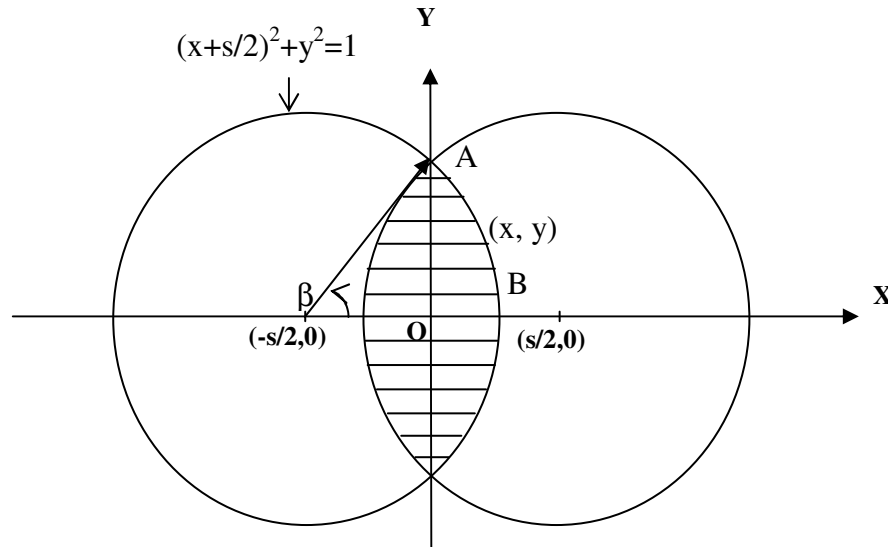


**Fig.1.** Region of integration for the rotationally symmetric systems, *i.e.* the area of overlap of two unit circles shifted symmetrically. Each circle represents the pupil function  $\Omega(x, y)$  of the proposed system. Because of the symmetry of the system, the function needs to be integrated over only one quadrant, say AOB.

In presence of defocus the pupil function of a clear aperture of a conventional lens is given by [17]

$$\Omega(x, y, W_{20}) = \begin{cases} \exp\{i k W_{20}(x^2 + y^2)\} & \text{for } (x^2 + y^2) \leq 1 \\ 0 & \text{otherwise} \end{cases} \quad (3)$$

where,  $k = 2\pi/\lambda$  is the propagation constant and  $W_{20}$  is the defocus coefficient.

Thus the monochromatic OTF for the lens under defocused condition may be written as

$$OTF_{mono}(W_{20}) = \frac{1}{N} \left[ \int_{x=0}^a \int_{y=0}^b 4 \cos [2 k W_{20} s x] dx dy \right] \quad (4)$$

where  $s$  is the normalized spatial frequency ( $0 \leq s \leq 2$ ),  $a = 1 - \frac{s}{2}$  and

$$b = \left[ 1 - \left( x + \frac{s}{2} \right)^2 \right]^{\frac{1}{2}}. \quad N = \pi \text{ is the normalizing factor of the OTF for the lens.}$$

Identifying the  $\lambda$ -dependent term in the above expression, the polychromatic OTF of the said system for polychromatic illumination with flat-top spectral profile comes out as

$$OTF_{poly} = \frac{1}{\int_{\lambda_1}^{\lambda_2} N d\lambda} \left[ \int_{\lambda_1}^{\lambda_2} \int_{x=0}^{a_\lambda} \int_{y=0}^{b_\lambda} 4 \cos [2 k_\lambda W_{20} s_\lambda x] dx dy d\lambda \right] \quad (5)$$

where  $a_\lambda = 1 - \frac{s_\lambda}{2}$  and  $b_\lambda = \left[ 1 - \left( x + \frac{s_\lambda}{2} \right)^2 \right]^{\frac{1}{2}}$ . The above expression is solved

numerically using the elegant and powerful 96-point Legendre-Gauss quadrature technique of integration [18]. The values of spatial frequencies for different wavelengths

can be found as  $s_{\lambda_i} = \frac{\lambda_i s_1}{\lambda_1}$ .

### 3 RESULTS AND DISCUSSIONS

We have already assumed that the polychromatic input beam has a flat-top spectral profile and the spectral sensitivity of the detector is neglected.  $\lambda_1$  is taken as 400 nm as this is approximately the lower cut-off value for the visible light. The polychromatic OTF curves for the conventional lens at the Gaussian image plane have been shown in Figs. 2 with spectral spreads ( $\Delta\lambda = \lambda_2 - \lambda_1$ ) of 0 nm, 100 nm, 200 nm and 300 nm. As shown in the figure, the values of OTF decrease with spectral spreads over the entire frequency range. Thus, it may be concluded that the transmission of different frequencies decreases with the increase of spectral spread.

In Fig. 3, the variation of the polychromatic OTF curves with defocus has been depicted for  $\Delta\lambda = 100$  nm. The transmission of different frequencies again gradually

decreases as defocus value increases. It is interesting to note that for  $W_{20} = 0.75\lambda_1$  and  $W_{20} = \lambda_1$  the OTF assumes negative values for a certain range of spatial frequencies ( $s = 0.70-1.03$  for  $W_{20} = 0.75\lambda_1$  and  $s = 0.41-1.32$  for  $W_{20} = \lambda_1$ ) signifying contrast reversal at those frequency ranges and unfaithful reproduction of the object.

Our proposed method may also be successfully employed to compute the polychromatic OTF of any optical system that may include wavelength dependent components. The study of polychromatic OTF of a birefringent lens (with its optic axis perpendicular to the lens axis) sandwiched between two linear polarizers will be reported in the next communication.

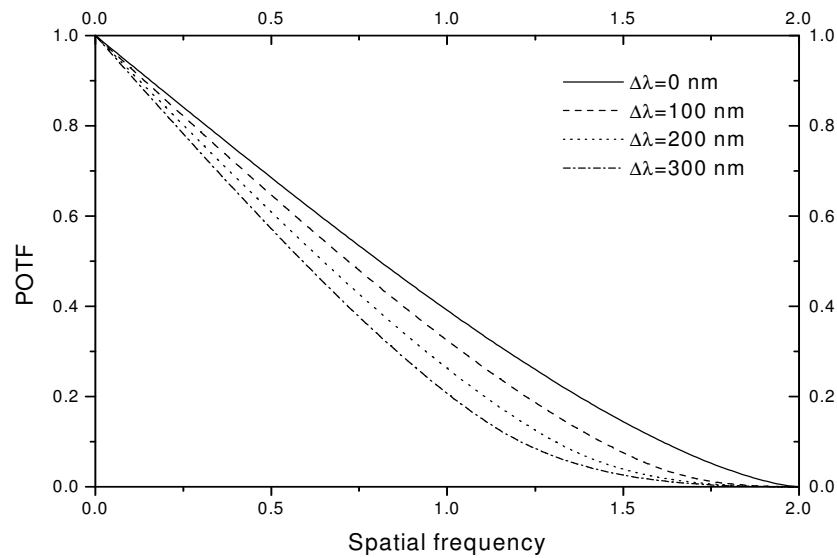


**Fig. 2.** Polychromatic OTF curves for the clear aperture isotropic lens the Gaussian image plane for different spectral spreads.

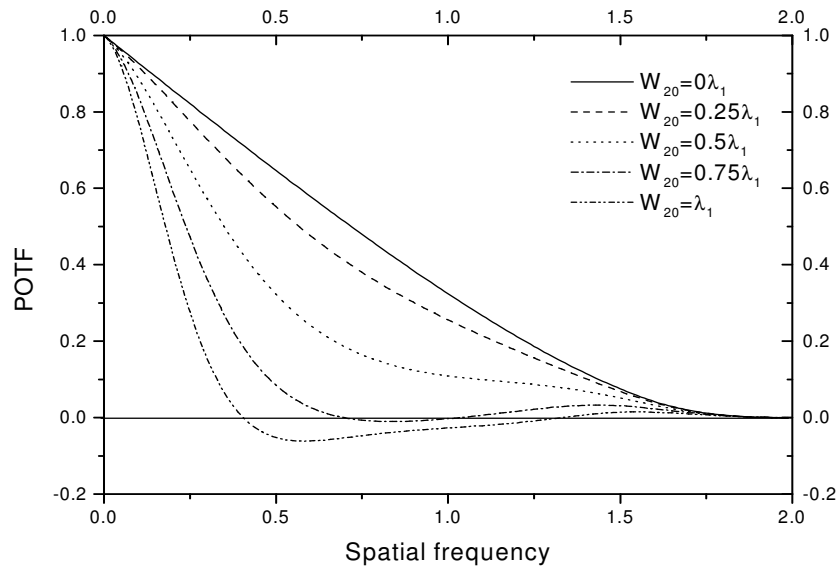


**Fig. 3.** Variation of the polychromatic OTF curves for the clear aperture isotropic lens with defocus.  
 $\Delta\lambda = 100 \text{ nm}$

## REFERENCES

1. H. Tiziani, "The use of optical transfer function for assessing the quality of optical Systems", *Photogrammetria* 34, 45-68 (1978).
2. R. Barnden, "Calculation of axial polychromatic optical transfer function", *Opt. Acta* 21, 981-1003 (1974).
3. R. Barnden, "Extra-axial polychromatic optical transfer function", *Opt. Acta* 23, 1-24 (1976).
4. M. Takeda, "Chromatic aberration matching of the polychromatic optical transfer function", *Appl. Opt.* 20, 684-687 (1981).
5. J. Bescos, J. Santamaria, "Colour based quality parameters for white light imagery", *Opt. Acta* 28, 43-45 (1981).
6. J. Bescos, J. H. Altamirano, J. Santamaria, A. Plaza, "Apodizing filters in colour imaging", *J. Opt. (Paris)* 17, 91 (1986).
7. J. Bescos, J. H. Altamirano, A. Santisteban, J. Santamaria, "Digital restoration models for color imaging", *Appl. Opt.* 27, 419-424 (1988).
8. D. Navajas, S. Vallmitjana, J. J. Barandalla, J. R. DE F. Moneo, "Evaluation of polychromatic image quality by means of transfer function", *J. Opt. (Paris)* 13, 283-287 (1982).

9. S. Vallmitjana, D. Navajas, J. J. Barandalla, J. R. DE F. Moneo, "A simple method of evaluating the polychromatic modulation transfer function for photographic systems", *J. Opt. (Paris)* 14, 25-28 (1983).
10. J. C. Grisolia, J. R. Priu, "A device for the optical transfer function measurement", *J. Opt. (Paris)* 16, 77-81 (1985).
11. M. Subbarao, "Optical transfer function of a diffraction-limited system for polychromatic illumination", *Appl. Opt.* 29, 554-558 (1990).
12. W. D. Furlan, G. Saavedra, J. Lancis, "Phase-space representations as a tool for the evaluation of the polychromatic OTF", *Opt. Commun.* 96, 208-213 (1993).
13. J. C. Escalera, M. J. Yzuel, J. Campos, "Control of the polychromatic response of an optical system through the use of annular color filters", *Appl. Opt.* 34, 1655-1663 (1995).
14. V. N. Mahajan, *Optical Imaging and Aberrations, Part II. Wave Diffraction Optics* (Chap. 2, pp. 208-209, SPIE Press Book, 2001).
15. L. E. Helseth, "Optical transfer function of three-dimensional display systems", *J. Opt. Soc. Am. A* 23, 816-820 (2006).
16. P. M. Duffieux, *L'intégrable de Fourier et Ses Applications a l'optique*, Besangon, privately printed (1946).
17. H. H. Hopkins, "The frequency response of a defocused optical system", *Proc. Roy. Soc. (London) A* 231, 91-103 (1955).
18. M. Abramowitz, I.A. Stegun, *Handbook of Mathematical Functions* (Dover Publications, INC., New York, 1972).

## Development of Colorimeter using Low Cost Optical Bridge

Kushan Chakrabarty<sup>1</sup>, Isha Das<sup>1</sup>, Shila Ghosh<sup>2</sup> (Member SPIE)

<sup>1</sup>Department of Electrical and Electronics Engineering,  
Indian Institute of Technology,  
Kharagpur, India

<sup>2</sup>Department of Electronics & Communication Engineering,  
B.P.Poddar Institute of Management & Technology,  
,Kolkata, Pin-700052, India

**Abstract.** This work aims to construct a low cost optical bridge and find suitable applications for the same. Optical bridge is based on Wheatstone bridge principle where voltage output is zero when the bridge is balanced. This is useful in applications which are based on light balancing or differences in light intensities. Optical bridge generally uses two light beams one of which acts as a reference while the other is modulated/varied by passing through a sample. This paper involves the realization of Colorimeter. Colorimeter measures concentration of coloured but transparent solutions. This can be used as biosensor to measure the concentration of blood constituents. The theoretical and experimental results are found almost same.

### 1. INTRODUCTION

Electronic instrumentation assumes prime importance in many areas including chemical and biochemical industries. One such simple but elegant instrumentation circuit is optical bridge. An optical bridge is a configuration of photosensitive devices that serve as an optical transducer. It follows the Wheatstone bridge principle. The most common configuration of optical bridge consists of two fixed resistors and two photosensitive devices. The circuit has an additional potentiometer by means of which the bridge is balanced. The above circuit may be modified to include only one photosensitive device while testing the operating principle and using the circuit as a simple sensor as shown in Fig. 1.

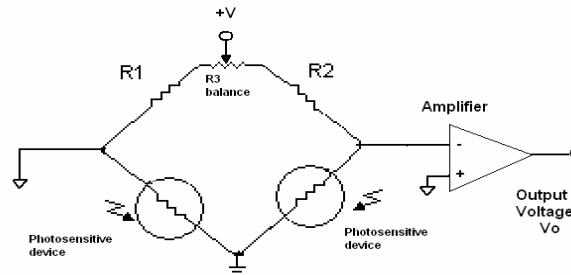


Fig. 1. Optical Bridge

## 2. THEORY

The system works on the principle of Beer-Lambert's law. This law states that the intensity of light goes on decreasing exponentially as it passes through a transparent/translucent sample with a rate of decrease dictated by the molar extinction coefficient of the material for that wavelength of light used. The law states that there is a logarithmic dependence between the transmission or transmissivity,  $T$ , of light through a substance and the product of the absorption coefficient of the substance,  $\alpha$ , and the distance the light travels through the material (i.e. the path length),  $\ell$ . The absorption coefficient can, in turn, be written as a product of either a molar absorptivity of the absorber,  $\epsilon$ , and the concentration  $c$  of absorbing species in the material, or an absorption cross section,  $\sigma$ , and the (number) density  $N$  of absorbers.

For liquids, these relations are usually written as

$$T = \frac{I}{I_0} = 10^{-\alpha\ell} = 10^{-\epsilon\ell c}$$

The transmission (or transmissivity) is expressed in terms of an absorbance which for liquids is defined as

$$A = -\log_{10} \left( \frac{I}{I_0} \right)$$

This implies that the absorbance becomes linear with the concentration (or number density of absorbers) according to

$$A = \epsilon\ell c = \alpha\ell$$

Thus, if the path length and the molar absorptivity (or the absorption cross section) are known and the absorbance is measured, the concentration of the substance (or the

number density of absorbers) can be deduced. Conversely, if the molar absorptivity and concentration are known then the path length may be calculated. The theoretical formula is deduced from the following Fig. 2..

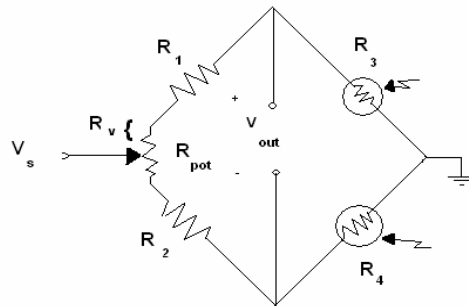


**Fig. 2.** Optical Bridge with resistances

From the diagram and applying voltage divider rule the output voltage may be calculated to be:

$$V_{out} = V_s \left[ \frac{1}{\left\{ \frac{(R_{pot}/2 + R_1)}{R_3} + 1 \right\}} - \frac{1}{\left\{ \frac{(R_{pot}/2 + R_1)}{R_4} + 1 \right\}} \right]$$

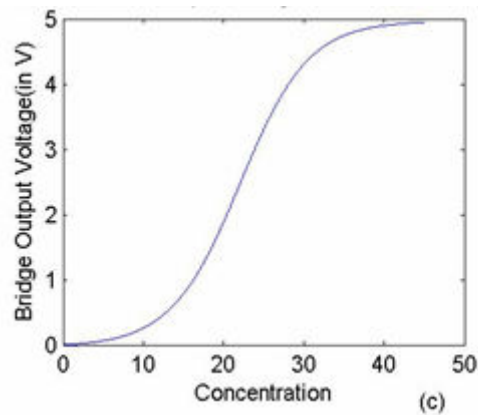


**Fig.3** Simulation Results of Output voltage versus concentration (c)

As  $R_3$  increases,  $V_{out}$  increases and as  $R_4$  increases  $V_{out}$  decreases.  $R_3$  varies with the concentration of liquid. Figure 3 shows the simulation result of voltage output versus concentration.

### 3. PROCEDURE

This part discusses the procedure followed to obtain the observations obtained as stated in the next subsection. The steps followed were as below:

The Optical Bridge was balanced using sunlight to ensure both the photodetectors of each bridge were illuminated equally. Light intensity of the two sources emitting the reference and principal (or sample) optical beams was equalized by treating the already balanced bridge as reference.

A 'blank' was formed by pouring distilled water in one of the vials. This was then placed in one of the light beams. This light beam thus became the reference light beam. Mother solution of 1.0 M copper sulphate ( $\text{CuSO}_4$ ) solution was taken in another vial up to the same level to which distilled water was poured in the 'blank'. The experimental setup for optical bridge colorimeter was completed by placing the above vial in the path of the principal beam.

The enclosure was closed to prevent external light perturbations. Bridge Output voltage was recorded. Similarly various concentrations of the solution were prepared and output voltage was measured. A Calibration curve was plotted and results were analyzed. A known solution of 0.45 M was taken as a sample whose concentration was to be determined using the optical bridge colorimeter from the above calibration curves. The sample (0.45 M) solution was taken in the sample vial and the output voltage for the two bridge circuits recorded. An estimate of the concentration of the sample solution was then made.

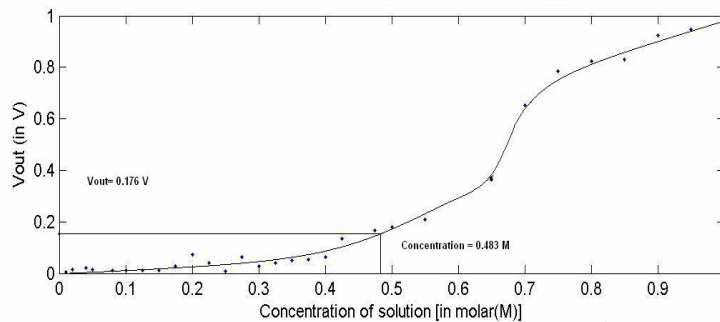


**Fig.4** Plot of experimental output voltage versus concentration

#### 4. RESULTS AND DISCUSSIONS

The theoretical and the experimental curve are almost of same nature. Figure 4 shows the plot of concentration versus output voltage.

There are erroneous readings at the lower concentrations which may be due to increased interference from external light during the recording of these observations. As concentration increases the colorimeter output increases almost monotonically.

From the above graph we have estimated the concentration of the sample to be 0.483 M which is close to the actual value of 0.45 M. [Error in estimation:  $(0.483 - 0.45)/0.45 = 7.33\%$ ]

This low cost colorimeter may be used measurement of concentration of many coloured solutions which absorb optical wavelengths. The colorimeter could be used for measurement of concentration of various gases. This is particularly useful in batch production of chemicals where the manufactured solution concentration may be easily compared with the reference solution's concentration. The colorimeter may be used to determine the oxygen saturation of blood Thus it can be used as Bio sensor. Based on this principle a thickness sensor could be developed.

#### 5. REFERENCES

1. John M Senior, Optical Fiber Communications: Principle and Practice, 2<sup>nd</sup> Edition, Prentice Hall of India.
2. John Webster CRC Press; 1 edition (December 29, 1998) Medical Instrumentation Application and Design
3. Handbook of Modern Sensors (Hardback) By (author) Springer-Verlag New York Inc. 29 September 2010
4. Annual Review of Biophysics and Biomolecular Structure , K.A. Giuliano, P.L.Post , K.M. Hahn, and D.L. Taylor, Vol. 24, 405-434, June 1995
5. Recent Development in Optical Fiber Biosensors, Maria Espinosa Bosch. et al, Sensors 2007, 7,797-859
6. Blood Glucose Sensors: An Overview, Peura, R.A.IEEE/ NSF Symposium on Biosensors, 1984 , pp 63-68

## Secured Data Communication Using PCM and Pseudo-Noise Generation

Mohammad Wasim Sayed, Nasibullah

Department of Electronics & Communication Engineering,  
B.P Poddar Institute of Management and Technology,  
Kolkata, Pin-700052, India

**Abstract.** This paper presents a secure way for point to point data communication. In the transmitter side, a sequence of pseudo random code is added with the PCM output in the binary adder which gives the transmitter output. Transmitter output signal is subtracted from pseudo random signal (by synchronization) in the receiver side, to get back the original signal.

**Keywords.** Secure data communication, Pseudo noise generation, PCM

### 1. INTRODUCTION

Pulse code modulation (PCM)[1] is a method used to digitally represent sampled analog signals. The processes involved in PCM are sampling, quantizing and encoding. In the transmitter side of PCM, the baseband signal is sampled at Nyquist rate[2] or above by the sampler which is then quantized in the quantizer. The encoder then encodes these quantized pulses into bits. In the receiver side of PCM, the pulses are passed through a regenerative repeater and then through a digital-to-analog converter. The output of the digital-to-analog converter is fed to an LPF to get back the analog signal. In this communication, we report a technique in which the PCM output is being added in the binary adder[3] with the pseudo random sequence which is coming from the sequential array. Finally, we get the transmitted output. In the receiver side, the transmitter output is now subtracted from the pseudo random sequence to get back the original baseband signal.

### 2. THEORY

The output of the encoder will give an encoded binary value of analog signal at a particular time instance. This encoded binary data is fed to the n-bit arithmetic binary adder. Another input of the binary adder is coming from the output of sequential array. A

sequential array consists of a ROM chip[3] and a counter[3]. Length of each data word in ROM must be less than or equal to n-bit.

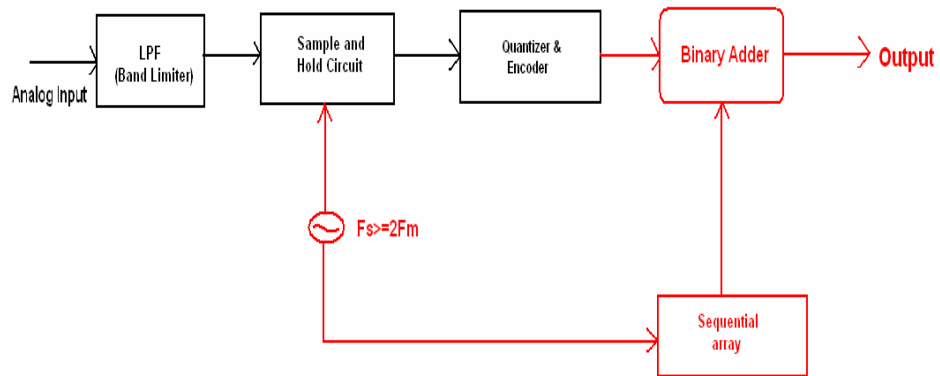


**Fig. 1.** Block diagram of transmitter

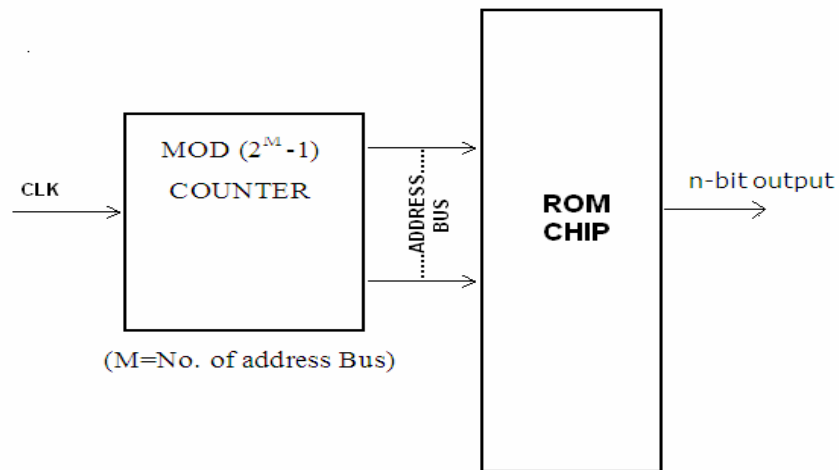


**Fig. 2.** Block diagram of sequential array

Fig. 2 represents the hardware model of sequential array. The ROM chip have  $M$  address line and it has  $(2^M-1)$  data word where bits per each word is  $n$ . So the array size will be  $(2^M-1)$  and the counter counts up to  $(2^M-1)$  and returns back to the  $0^{\text{th}}$  position. The clock frequency of the counter should be equal to the sampling frequency( $f_s$ ) .

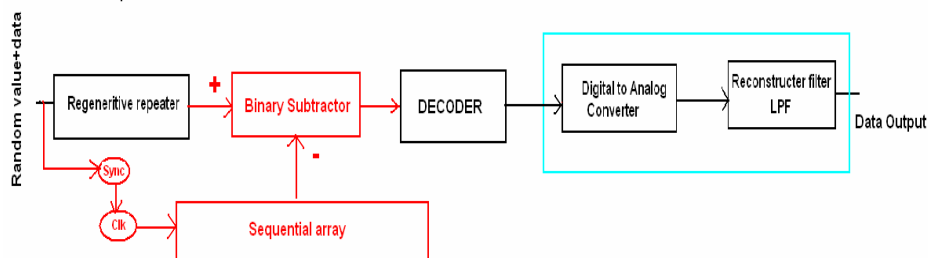


Fig 3. Block diagram of receiver

In arithmetic binary subtractor[3] there are two inputs, where the output from the regenerative repeater is taken as minuend and output from the sequential array is taken as subtrahend. The output of the arithmetic binary subtractor is fed to decoder, which is then fed to digital to analog converter and finally to a LPF to get back the analog baseband signal.

**Generation of random sequence code:-**In this paper random numbers are generated by the following recurrence.

$$x_{n+1} = P_1 x_n + P_2 \pmod{N} \quad n = 0,1,2,\dots \text{ and } x_0 = \text{given} \dots [4]$$

**Example:-**

$$\text{If } x_0 = 79, N = 100, P_1 = 263, \text{ and } P_2 = 71$$

then

$$x_1 = 79*263 + 71 \pmod{100} = 20848 \pmod{100} = 48,$$

$$x_2 = 48*263 + 71 \pmod{100} = 12695 \pmod{100} = 95,$$

$$x_3 = 95*263 + 71 \pmod{100} = 25056 \pmod{100} = 56,$$

$$x_4 = 56 \cdot 263 + 71 \pmod{100} = 14799 \pmod{100} = 99$$

Subsequent numbers are: 8, 75, 96, 68, 36, 39, 28, 35, 76, 59, 88, 15, 16, 79, 48.

The parameters  $P_1$ ,  $P_2$  and  $N$  determine the characteristics of the pseudo random number generator, and the choice of  $x_0$  (the **seed**) determines the particular sequence of random numbers that is generated. If the generator is run with the same values of the parameters and the same seed, it will generate a sequence that is identical to the previous one and it might be predictable.

To overcome this, the value of parameters  $P_1, P_2$  and  $N$  is kept changing pseudo randomly for generation of each numbers.

$$x_{n+1} = P1_n x_n + P2_n \pmod{N_n} \quad n = 0, 1, 2, \dots \quad \text{and } x_0 = \text{given}$$

where  $P1_n = (P1_{n-1} * P1_{init} + P2_{init}) \pmod{N_{init}}$ ,

$$P2_n = (P2_{n-1} * P2_{init} + P2_{init}) \pmod{N_{init}},$$

$$N_n = (N_{n-1} * N_{init} + N_{init}) \pmod{N_{init}}$$

### **Bandwidth requirement:**

Before the binary adder the bandwidth required  $\geq 0.5 * fs * v$ , where quantization level represents in  $v$  digit.

Bandwidth required after binary adder  $\geq 0.5 * fs * n$ , where  $n$  is the length of data bits in ROM chip.

## **3. RESULTS AND DISCUSSIONS**

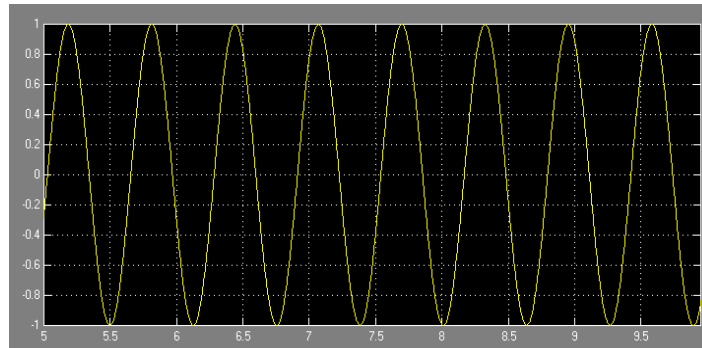


**Fig 4. Analog Baseband Signal**

This is a continuous sinusoidal signal with frequency 100 Hz.



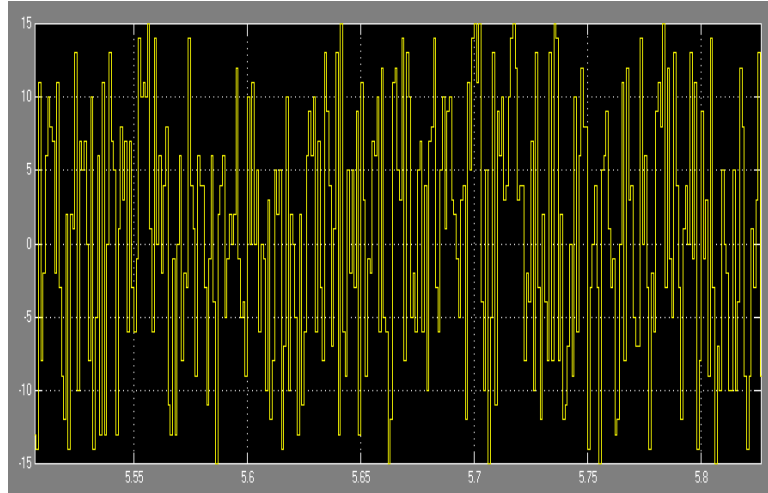


**Fig 7.** Pseudo Random value signal

This pseudo random code (Fig 7) gets added with the output of encoder (Fig 6). The output data is pseudo random in nature which is transmitted to the channel as shown in fig 8. (Table-1) shows the data of message signal, pseudo random signal and pseudo random value added with message signal.

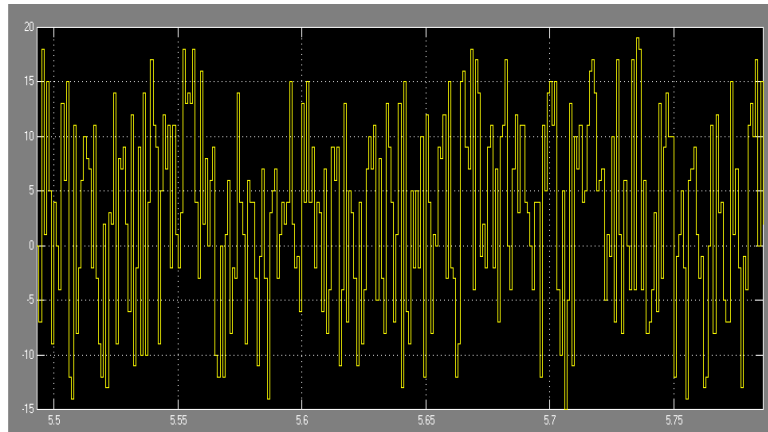


**Fig 8.** Pseudo Random value mixed message signal

Table-1

<b>time<sup>1</sup></b>	<b>value<sup>1</sup></b>	<b>time<sup>2</sup></b>	<b>value<sup>2</sup></b>	<b>time<sup>3</sup></b>	<b>value<sup>3</sup></b>
9.9540	0	9.9540	-12.0000	9.9540	-12.0000
9.9560	0	9.9560	-10.0000	9.9560	-10.0000
9.9580	0	9.9580	0	9.9580	0
9.9600	0	9.9600	11.0000	9.9600	11.0000
9.9620	0	9.9620	15.0000	9.9620	15.0000
9.9640	0	9.9640	3.0000	9.9640	3.0000
9.9660	0	9.9660	-5.0000	9.9660	-5.0000
9.9680	0	9.9680	2.0000	9.9680	2.0000
9.9700	1.0000	9.9700	-11.0000	9.9700	-10.0000
9.9720	1.0000	9.9720	-8.0000	9.9720	-7.0000
9.9740	1.0000	9.9740	4.0000	9.9740	5.0000
9.9760	1.0000	9.9760	8.0000	9.9760	9.0000
9.9780	1.0000	9.9780	12.0000	9.9780	13.0000
9.9800	1.0000	9.9800	-13.0000	9.9800	-12.0000
9.9820	1.0000	9.9820	-15.0000	9.9820	-14.0000
9.9840	1.0000	9.9840	-11.0000	9.9840	-10.0000
9.9860	1.0000	9.9860	-7.0000	9.9860	-6.0000
9.9880	1.0000	9.9880	2.0000	9.9880	3.0000
9.9900	1.0000	9.9900	-5.0000	9.9900	-4.0000
9.9920	1.0000	9.9920	-2.0000	9.9920	-1.0000
9.9940	1.0000	9.9940	0	9.9940	1.0000
9.9960	1.0000	9.9960	13.0000	9.9960	14.0000
9.9980	1.0000	9.9980	-9.0000	9.9980	-8.0000
10.0000	1.0000	10.0000	-5.0000	10.0000	-4.0000

\*Value1 is data value corresponding to time1, value2 is pseudo random value corresponding to time2, value3 is pseudo random value combined with data value corresponding to time3.

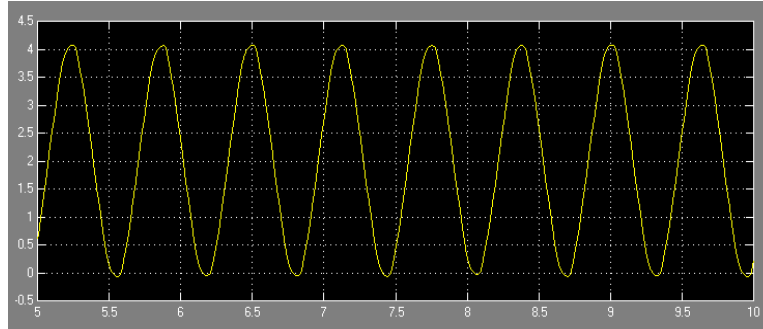


**Fig 9.** Receiver Output Signal

This is a receiver output signal coming from reconstructive LPF filter whose frequency is same as the frequency of the original baseband signal(100 Hz).

This is a simple system, in which only few blocks have been added to the PCM transmitter for secure data communication, but it has a limitation of jamming protection. It can be used for secure voice transmission as well as military applications.

#### **4. REFERENCES**

1. Communication System by R P Sing and S D Sapre, TMH publication
2. Communication Systems by Sanjay Sharma
3. Digital Circuits and Design by S Salivahanan and S Arivazhagan
4. [www.math.utah.edu/~pa/random/random.html](http://www.math.utah.edu/~pa/random/random.html)